Nanoscale Characterisation and Neutron Damage Testing of Organic semiconductors

Giuseppe Maria Paternò

A dissertation submitted for the degree of Doctor of Philosophy

Department of Physics and Astronomy and London Centre for
Nanotechnology

University College London

London, 2016

I, Giuseppe Maria Paternò, confirm that the work presented in this thesis is my own. Where information has been derived from other sources and work which has formed part of jointly-authored publications has been used I confirm that this has been indicated in the thesis.

To my family

To those who supported me during most of this doctoral journey

To those who supported me during the hardest part…

Acknowledgements

This thesis is based on the work carried out at the Organic Semiconductors and Nanostructures group at the Department of Physics and Astronomy and London Centre for Nanotechnology (LCN), University College London (UCL), and at the ISIS - Neutron and Muon Source, Rutherford Appleton Laboratory. My research was founded by an IMPACT PhD studentship co-sponsored by UCL and ISIS - Neutron and Muon Source (grant number 509238).

First and foremost I would like to thank my supervisors, Prof. Franco Cacialli and Dr. Victoria García Sakai, and express my gratitude for their support, helpful guidance and valuable scientific insight throughout my doctoral studies. I would like to thank all collaborators and MsC students who helped me in the lab (Yuan, Jens and Daniele): without each of them this work would not have been possible.

A big thanks to present and past members of the Organic Semiconductors and Nanostructures group, and to the physics basement crew for providing a friendly work environment and for being a good source of humour.

Finally, a very special thanks to my “Italian family”: Alessandro, Andrea, Antonia, Luca, Micky, Moreno and Vale, for their help and for all the fun we had during my adventure in London.

Abstract

In this thesis work, I employ a wide range of morphological, structural and dynamical tools to investigate how the intermolecular interactions in a variety organic semiconductors (OSCs) can influence heavily the nanoscale arrangement and govern the tolerance against external stimuli (i.e. radiation) of these promising materials and related devices. Among the experimental techniques used, this work emphasises on the use of neutron scattering, due to the strong propensity of highly hydrogenated materials to scatter these particles, and thus reveal precious information about their inner structural and dynamical features.

I exploit the power of intermolecular interactions, to grow large and solvent-free single crystals of the electron-acceptor of choice of organic solar cells, the fullerene derivative [6,6]-phenyl-C61-butyric acid methyl ester (PCBM). The structure and quality of these crystals have been characterised by X-rays diffraction and metrological atomic force microscopy experiments. High-quality and solvent-free crystals of organic semiconductors can be a reliable platform for studying the intrinsic optical and electronic properties of these materials.

The nanoscale structure and dynamics of poly (thiophene):fullerene blends has been investigate by means of neutron reflectivity and quasi-elastic neutron scattering. In particular, I show that the intercalation of fullerene particles in between polymer side-chain depends on degree of order of the polymer. Furthermore, I find that polymer:fullerene interaction has a great effect on polymer dynamics, leading to a retardation of side-chain motion. The interaction between polymer and fullerene particles and their nanoscale mutual arrangement is of great interest for improving the charge phogeneration process in organic solar cells.

Finally, I studied for the first time the neutron radiation tolerance of two benchmark poly(thiophenes), observing that polymer crystallinity has a prominent role in determining the neutron radiation tolerance of conjugated polymers. Radiation hardening studies on organic electronics can pave the way to the integration of this class of devices in space and avionic applications.

Contents

List of Figures

List of Tables

List of Publications

Publications included in this thesis

- "Micro-focused X-ray diffraction characterization of high-quality [6, 6]-phenyl-C 61-butyric acid methyl ester single crystals without solvent impurities"

  Giuseppe M. Paternò, Anna J. Warren, Jacob Spencer, Gwyndaf Evans, Victoria García Sakai, Jochen Blumberger, Franco Cacialli. *Journal of Materials Chemistry C*, 1 (2015), 5619-5623.
- "Traceable atomic force microscopy of high-quality solvent-free crystals of [6, 6]-phenyl-C61-butyric acid methyl ester"

  Giovanni M. Lazzerini, Giuseppe M. Paternò, Giulia Tregnago, Neil Treat, Natalie Stingelin, Andrew Yacoot, Franco Cacialli. *Applied Physics Letters*,108 (2016), 053303.
- "Tuning Fullerene Intercalation in a Poly (thiophene) derivative by Controlling the Polymer Degree of Self-Organisation"

  Giuseppe. M. Paternò, Maximilian.W. A. Skoda, Robert Dalgliesh, F. Cacialli and V. García Sakai. *Sci Rep 6 (2013), 34609.*
- "Structural and dynamical characterization of P3HT/PCBM blends"

  Giuseppe M. Paternó, Franco Cacialli, Victoria García-Sakai. *Chemical Physics*, 427 (2013), 142-146.
- "Neutron polarisation analysis of Polymer: Fullerene blends for organic photovoltaics"

  Giuseppe M. Paternò, John R. Stewart, Andrew Wildes, Franco Cacialli and Victoria García Sakai. *Polymer*, 105 (2016), 407-413.
- "Neutron Radiation Tolerance of Two Benchmark Thiophene-Based Conjugated Polymers: the Importance of Crystallinity for Organic Avionics"

  Giuseppe Maria Paternò, Valentina Robbiano, Keith J. Fraser, Christopher Frost, Victoria García Sakai and F. Cacialli. *Scientific Reports, (2017), in press.*

Other publications

- "Inorganic caesium lead iodide perovskite solar cells"

  Giles E Eperon, Giuseppe M. Paternò, Rebecca J. Sutton, Andrea Zampetti, Amir Abbas Haghighirad, Franco Cacialli, Henry J. Snaith. *Journal of Materials Chemistry A*, 3 (2015), 19688-19695.

- “Low-Temperature Photoluminescence Spectroscopy of Solvent-Free PCBM Single-Crystals”

  Giulia Tregnago, Michael Wykes, Giuseppe M. Paternò, David Beljonne, Franco Cacialli. *Journal of Physical Chemistry C 2015, 119 (2015),11846–11851*

- "In operando Neutron Radiation Damage Testing of Organic Solar Cells"

  Giuseppe M. Paternò, Valentina Robbiano, Luca Santarelli, Andrea Zampetti, Christopher Frost, Victoria García Sakai and Franco Cacialli. *Manuscript in preparation.*

- "Nanostructured titania for efficient perovskite solar cells"

  Valentina Robbiano, Giuseppe M. Paternò, Giovanni. F. Cotella, Tiziana Fiore, Martina Dianetti, Francesca Brunetti, Bruno Pignataro, Henry J. Snaith, and Franco Cacialli. *Manuscript in preparation.*

List of conference oral presentations

- Giuseppe Maria Paternò, Franco Cacialli and Victoria García Sakai, *Structural and Dynamical Characterization of Poly(thiophene)/Fullerene-derivative Blends,* **International Conference on Neutron Scattering**, Edinburgh, 09/7/2013
- Giuseppe M. Paternò, Franco Cacialli and Victoria García Sakai, *Structural and Dynamical Characterization of Poly(thiophene)/Fullerene-derivative Blends,* **QENS/WINS Conference**, Autran, Grenoble, 16/05/2014
- Giuseppe M. Paternò, Valentina Robbiano, Franco Cacialli and Victoria García Sakai, *Neutron Radiation Tolerance of Organic Field-Effect Transistors,* **European Materials Research Society Meeting**, Lille, 27/5/2014.
- Giuseppe M. Paternò, Valentina Robbiano, Franco Cacialli and Victoria García Sakai, *Neutron Radiation Tolerance of Organic Field-Effect Transistors,* **European Symposium on Reliability of Electron Devices**, Berlin 01/10/2014.
- Giuseppe M. Paternò, Valentina Robbiano, Luca Santarelli, Andrea Zampetti, Christopher Frost , Victoria García Sakai and Franco Cacialli, *Neutron Radiation Tolerance of Organic Solar Cells,* **International Conference on Materials for Advanced Technology**, Singapore 30/06/2015.

Introduction

Conjugated polymers are a class of macromolecules that exhibit semiconducting and, under certain conditions, metallic behaviour. The research in this field started gaining momentum in the 1970s with the synthesis[1] and doping of polyacetylene films[2, 3], which opened the field of synthetic metals. The second breakthrough came with the discovery of the electroluminescence in conjugated polymers that led to the development of the field of polymer optoelectronics[4]. These important seminal works paved the way for the effective use of these materials in a range of optoelectronic devices including organic photovoltaic diodes (OPVDs)[5, 6], organic light-emitting diodes (OLEDs)[4] and organic field-effect transistors (OFETs)[7, 8].

The excellent mechanical properties of these carbon-based materials, combined with their high and low-cost processability over large areas, and the tunability of their properties via chemical and supramolecular synthesis[9], have made them considerably attractive for the electronics industry. For instance, organic electronics can be used in a wide range of applications where lightness and flexibility are highly desirable, such as wearable electronics, space and avionics. However, conjugated polymers display some intrinsic limitations, which stem mainly from the localised nature of the charge carriers. On the other hand, the confinement of both the excitations and charges within a few nanometres, which lend them a quasi-one dimensional character, can be reduced partially by favouring the intermolecular interaction and crystallinity at the nanoscale and thus extending delocalisation of the charges. To achieve this, a detailed understanding of the morphology at the nanoscale in the time (dynamic) and space (structure) domains is required. This is particularly relevant for those technologies in which multi-component systems with a higher degree of nano-complexity are employed, i.e. polymer-fullerene blends in OPVDs.

The work presented here involves acquiring a more complete insight into the nanoscale arrangements of organic semiconductors in pure crystalline form and in blends, by combining a wide range of experimental techniques, with particular emphasis to neutron scattering. Neutron scattering is a powerful and versatile tool to investigate these systems and in particular highly hydrogenated conjugated polymers, since hydrogen shows the highest neutron scattering cross section among the isotopes[10]. For instance, the large neutron scattering contrast between conjugated polymers and fullerene derivatives (usually around one order of magnitude), allows one to obtain detailed information about the nanomorphology in these blends that is complementary to the information acquired via electron-sensitive techniques, such as electron microscopies and X-ray scattering techniques[11, 12]. Furthermore, intense and broadband neutron pulses can be used to study the effect of neutron irradiation on organic electronics, of importance when used in space and avionic applications. Despite neutron irradiation being a well-established probe to mimic the effects of cosmic rays on silicon-based electronics[13, 14], the experiments I present in this thesis are the first on the neutron radiation hardening of organic electronics, to the best of my knowledge.

Scope and Overview of the Thesis

In this work, I present evidence of how intermolecular interactions play a crucial role in determining the morphology at the nanoscale of organic semiconductors and consequently their optoelectronics properties and their resilience against external stimuli, such as radiation. As already described in the introductory section, these soft and rather disordered systems display lower charge transport features in comparison to their inorganic counterparts. On the other hand, their soft nature can be seen as an advantage, as softness permits access to the realm of intermolecular interactions and non-covalent bonding, which are the tools that nature uses to make life possible (DNA double helix, proteins folding/unfolding and so on). Although controlling the intermolecular level at the nanoscale is more difficult and elusive, it is still paramount for controlling and manipulating the relevant properties of these materials, such as luminescence and charge transport.

The thesis is organised as follows. In **Chapter 1** I give an introduction to conjugated polymers and their fundamental properties in terms of charge transport and photoexcitation events. In this chapter, I also present an overview of the optoelectronic devices that have been investigated in this work.

Chapter 2 follows with the theoretical and experimental background to the neutron scattering techniques employed for the studies, as well as some background about neutron irradiation specific to semiconductors.

The experimental results are described in the next four chapters. **Chapter 3** describes the synthesis and characterisation of solvent-free, high-quality and large (100s of micrometres) single crystals of [6,6]-phenyl-C61-butyric acid methyl ester (PCBM), which is the electron-acceptor of choice in organic solar cells. In this chapter, I also show some nanoscale investigations of crystals morphology by means of metrological atomic force microscopy (AFM) and show how detailed morphological analysis can give an insight into the mechanism of crystal growth. **Chapter 4** presents results from a combined X-ray diffraction and neutron reflectivity study of a pseudo-bilayer system made of poly(2,5-bis(3-hexadecylthiophen-2-yl)thieno[3,2-b]thiophene (PBTTT) and [6,6]-phenyl-C61-butyric acid methyl ester (PCBM), which provided a more complete understanding of the diffusion and intercalation of the fullerene-derivative within the polymer layer.

In **chapter 5,** I present data from X-ray diffraction and neutron spectroscopy on the structure and dynamics of a commonly used blend in organic photovoltaics, poly(3-hexylthiophene-2,5-diyl), P3HT, with PCBM. The study shows that blending leads to a retardation of the polymer dynamics, as it has been seen for other polymer-nanocomposite systems.

In the first part of **chapter 6**, I present the results from the neutron radiation tolerance of the two well-established poly(thiophene) derivatives used in the previous chapters, P3HTand PBTTT. Combining a series of spectroscopic techniques (optical absorption, x-ray photoelectron spectroscopy and Raman scattering) with a characterisation of field-effect transistors and therefore of the intrinsic charge mobility, I show that the two polymers behave very differently upon neutron irradiation.

The thesis finishes with **chapter 7** where I summarise the results obtained, and provide an outlook and suggestions for future work.

1 Organic conjugated systems and related devices

In this chapter, some fundamental properties of organic conjugated systems are discussed. In this class of materials, which comprise conjugated polymers (CPs) and small molecules, the carbon atoms exhibit sp^2 hybridisation and there is the possibility of intramolecular π-bond formation involving the p_z orbitals. The semiconducting properties of these systems lie on the alternation of single (σ) and double bonds (σ + π) in the molecule, which gives rise to an extended and partly delocalised π-electrons cloud all over the molecule. Although to a first approximation the electronic properties of conjugated materials can be explained in terms of classical semiconductor physics, their charge transport properties are in fact quite different from those observed in their corresponding inorganic semiconductors. This can be attributed to the strong anisotropy between intramolecular and intermolecular electronic interactions, with the former sensibly stronger than the latter[15]. Such an effect, coupled with the relatively low dielectric constant in these materials and the strong electron-phonon coupling, leads to a substantial localisation of the electronic wavefunction and excitations. In the first section, I discuss about the concept of conjugation and why these systems are, to a first approximation, regarded as organic semiconductors. The second section focuses on the charge transport features and excitation events in CPs. The chapter finishes with a discussion of two classes of organic devices relevant to this work, OPVDs and OFETs.

1.1 Electronic properties

The electronic structure of conjugated molecules and, in particular, macromolecules is dominated by π- electrons. The concept of conjugation arises from the theory of atomic orbital hybridisation, which was introduced by Linus Pauling to rationalise the geometry of simple organic molecules[16]. The electronic configuration of carbon atom at the ground level is $1s^2\ 2s^2\ 2p^2$. If we consider the methane CH_4, carbon would combine its four orbitals with the 1s orbitals of the hydrogen atoms giving four bonding molecular orbitals (MOs). Three orthogonal MOs would arise from the overlap between the three p-orbitals (p_x, p_y, p_z) and the 1s of the hydrogen, and one weaker MO with no specific directionality obtained by the overlap of the carbon and hydrogen 1s spherical orbitals. However, methane shows four equivalent bonds, with a tetrahedral bond angle of 109.5°. This was explained in terms of *hybridisation* of the four carbon orbitals, to give four equivalent *hybridised* sp^3 orbitals. Such a theory can be also invoked to explain the geometry and electronic properties of organic molecules containing double and triple bonds. In the simple case of ethylene ($H_2C=CH_2$), the triangular planar molecular geometry (bond angles 120°) can be rationalised as carbon hybridises three of its four atomic orbitals to give three sp^2 hybrids orbitals, and one unhybridised p_z orbitals that points perpendicular to them (figure 1.1a). The linear and strong overlap between the sp^2 hybrids with the orbitals of the neighbouring atoms gives rise to three σ-orbitals, all lying on the molecule plane. On the other hand, the lateral overlap between the two non-hybridised p_z orbitals with one electron each, leads to the formation of a π-bond, with an electron density that extends above and below the σ-bond plane. The larger energy splitting for the σ- σ^* (bonding - antibonding) orbitals is due to the stronger linear overlap for the σ-bonds than the lateral overlap in the π-bonds, and define the π and π^* as the frontier molecular orbitals (figure 1.1b), with the π-orbital being the *highest occupied molecular orbital* (HOMO) and the π^*-orbital the *lowest unoccupied molecular orbital* (LUMO). If we extend the alternation of single and double bonds to a larger number of sp^2 hybridised carbon atoms, the lateral overlap between π-orbitals permits the delocalisation of the π-electrons over the whole molecule and, thus, the HOMO-LUMO energy gap decreases accordingly. This particular alternate arrangement of single and double bonds is called *conjugation*, and the systems that exhibit such an electronic architecture are called *conjugated*.

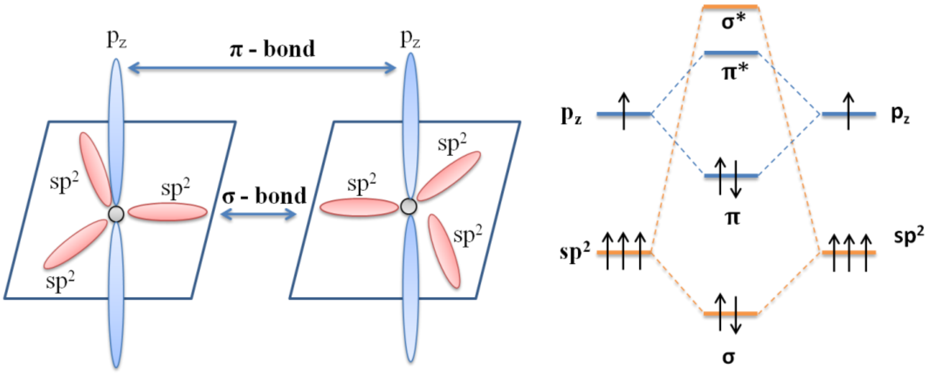

Figure 1.1: a) Representation of the concept sp^2-hybridised carbon atoms and formation of the C=C in ethylene; b) electronic energetic diagram of the ethylene and splitting the energy levels in bonding (σ , π) and antibonding (σ*,π*) states.

In the case of polyconjugated materials, such as *trans*-polyacetylene (PA, fig 1.2a), the extended delocalisation of the π-electrons results in the formation of quasi-continuous π (occupied) and π* (unoccupied) bands, with the HOMO and LUMO levels acting as the frontier energy states of the band system. It is important to note that in this delocalised configuration, polyacetylene would behave as a one-dimensional metal, as the p_z electrons half-fill the π-band (fig 1.2 left). However, it can be demonstrated that the two bonding configurations of PA chain are unstable with respect to so-called Peierls distortion (or dimerisation)[17], as found for 1D and quasi-1D conductors[18, 19]. Given a chain with a real space periodicity of a and half-filled 1D band (Fermi points at $\pm \pi/a$), an elastic distortion in the chain may bring to a lowering of the symmetry so that the new periodicity is twice ($2a$) the original value. This will open a new band-gap at the new Brillouin-zone boundaries ($k = \pm \pi/2a$), and thus the overall electronic energy is lowered as filled electron states with energies below the new Fermi points ($\pm \pi/2a$) are pulled down, whereas empty states are pushed up: as long as the increase in the strain energy caused by the distortion is lower than the decrease of the electronic energy such dimerisation will be energetically favoured (Fig. 1.2). Hence, such a mechanism explains why the electronic properties of trans-polyacetylene and, more in general, of conjugated polymers can be rationalised in terms of semiconductor physics, with the HOMO-LUMO energy gap regarded as the band gap between the valence band and conduction band in the classical semiconductor materials. Neutral (undoped) CPs features typically an optical band gap of 2-3 eV, whereas electronic band-gap lies ~ 0.5 - 1 eV higher in energy due to the strong electron-hole binding energy in such systems (~0.5 - 1.5 eV)[15].

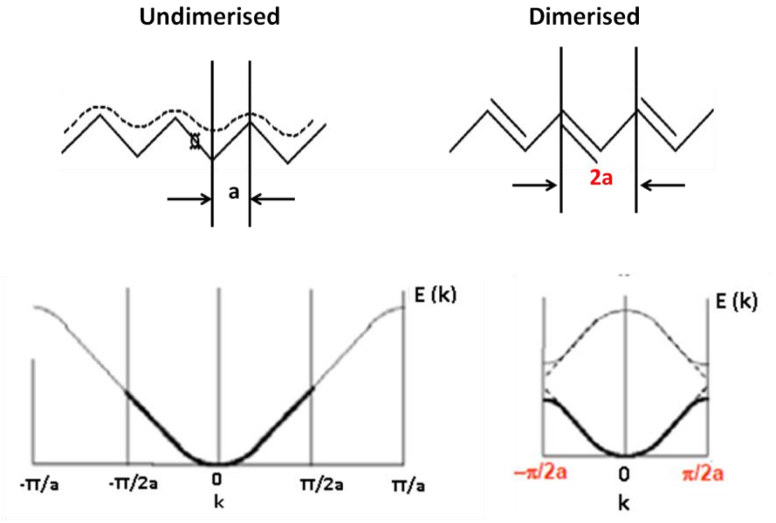

Figure 1.2: Undimerised (metallic) form of pure trans-PA and dimerised (semi-conductive) form arising from the Peierls distortion of the chain.

1.1.1 Excitations and charge transport

The localisation of electrical- and photo-excitations are the main optoelectronic peculiarities of CPs, which in turns dictates the working principles and the design criteria of the related devices. In particular, such a distinct feature arises mainly from three synergistic effects occurring in organic semiconductors and namely: i) the weak electron-electron screening due to the relatively low dielectric constant ($\varepsilon = 2 - 4$)[20]; ii) the strong electron-lattice coupling that leads to the self-trapping of excited states and lends them a strong quasi-particle character; iii) the broad and disordered density of electronic states (i.e intra-band defective states and tail states) that originates from the structural disorder. These characteristics have a great effect on the charge transport mechanism occurring in CPs.

An excess of electric charge can be introduced in the CPs by means of chemical (i.e. oxidation/reduction), electrical (charge injection) and photo doping. When this occurs, the extra charges will not enter the conduction or valence band as in conventional 3D semiconductors, but will introduce kinks in the conjugated sequence. In the case of doubly degenerate electronic ground state such as in *trans*-PA (see fig 1.3a) charges will accommodate in defective states, the so-called *solitons*, which behave as solitary waves localised in a range of 10-15 carbon atoms[21, 22]. Their electronic energy falls in the middle of the π-π*, making possible midgap optical transitions in addition to π-π* interband transitions. An excess electron on *trans*-PA produces doubly occupied negatively charged solitons S^-; in like manner, an excess hole produces an empty positively charged soliton S^+ (Fig. 1.3b).

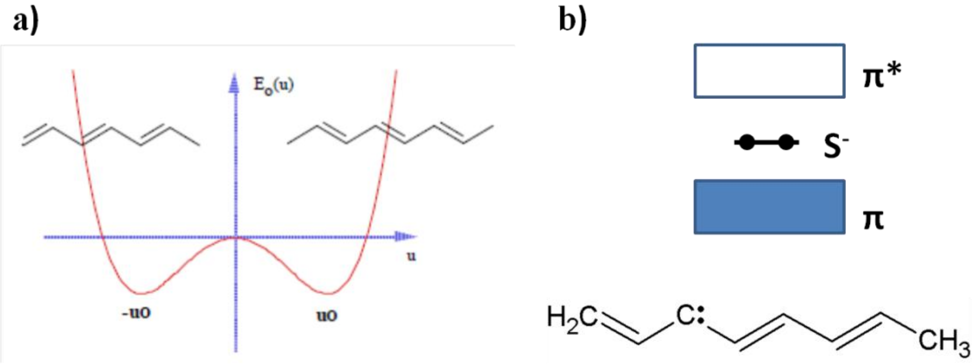

Figure 1.3: a) Degenerate ground electronic structure for trans-PA. This degeneration accounts for the single-defective electronic state called *soliton* upon doping of the conjugated system; b) Negatively charged soliton in PA.

For conjugated systems that do not possess any doubly degenerate electronic ground state (i.e the lower energy benzenoid state and the higher energy quinoid state for poly phenynele-vinylene), excess electronic charge causes a change in the bond-alternation pattern. However, this excitation is now strongly localised to minimise the energy cost of introducing a higher energy excited states and, thus, cause a local distortion of the chain. As these charged quasi-particles deform and polarise the surrounding lattice, and can be seen as charged polarisation waves, they are called *polarons*. Note that a *polaron* can be regarded as being equivalent to a localised pairs of *solitons*, the interaction of which makes possible the formation of a bonding/anti-bonding combination of *solitons*. Only in the case of doubly degenerate electronic state (i.e. *trans*-PA), the *polaron* can decay into a *soliton*, as the two polaronic bonding and anti-bonding levels are simply two degenerated resonance states. *Polarons* can accommodate up to four electrons giving negative *polarons* p^-, negative *bipolarons* bp^{2-}, positive *polarons* p^+ and positive *bipolarons* bp^{2+} (fig. 1.4)[23].

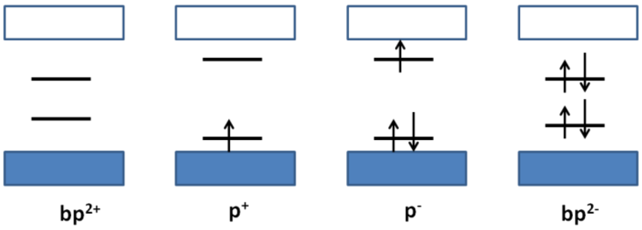

Figure 1.4: Polarons and bipolarons energy levels in non-degenerate ground state conjugated polymer.

Excitons, on the other hand, are neutral quasi-particles that originate from the photoexcitation of the electrons to an excited state (figure 1.5). These, in fact, can be regarded as bound electron-hole pairs, with binding energies (BE) and diffusion lengths strongly dependent on the charge screening features of the material. For instance, in low-dielectric constant CPs ($\varepsilon = 2\text{-}4$) the Coulombic attraction between the excited electron and the hole left in the ground state is weakly screened and, hence, the BE of these quasi-particles, the so-called *Frenkel excitons*, is relatively high (0.5 - 1.5 eV)[24]. In addition, *Frenkel excitons* possess a distinct localised character, with diffusion length in the order of 10 nm[15]. Conversely, if the electron-hole Coulombic attraction is strongly screened, as it happens in high dielectric constant materials, the electron-hole pairs, that in this case are termed *Wannier-Mott excitons*, display BEs of few meV and diffusion lengths that can be delocalised over tens of the lattice constant in inorganic materials (i.e. ≥ 100 µm in single crystalline systems).

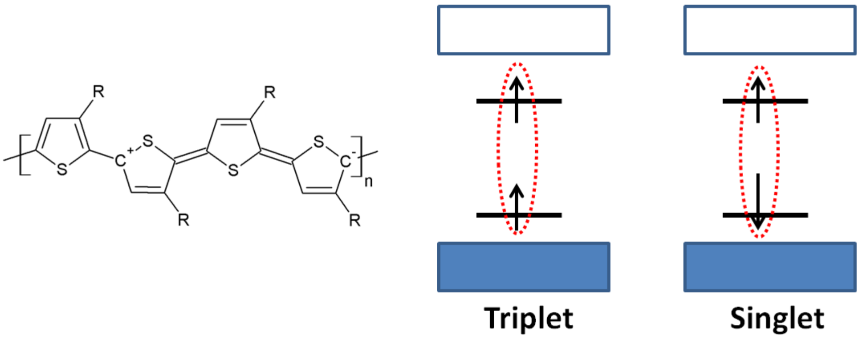

Figure 1.5: Representation of an exciton on a poly (alkylthiophene) alongside with the energetic diagram for a triplet and singlet exciton.

Given the strong localisation of charge carriers and excitations in organic materials, charges are self-trapped by the deformation they induce in the chain and, thus, transport occurs by hopping between localised states that is assisted by phonons scattering[25]. Therefore, charge mobility μ increases with temperature in OSCs, whereas μ decreases vs. T in their inorganic counterparts. It has been observed that, in general, the temperature dependence of the mobility can be described by an exponential law as in equation 1.1:

$$\mu = \mu_0 \, \mathrm{e}^{-(\frac{T_0}{T})^{\alpha}} \, , \tag{1.1}$$

where μ_0 is the pre-exponential factor representing the hypothetical hopping mobility in the absence of energetic disorder, T_0 is an empirical parameter related to the Gaussian width of the site distribution and α being an integer with values between 1 and 4[26]. At room temperature μ ranges typically from 0.1 $cm^2\ V^{-1}$ to 2.5 $cm^2\ V^{-1}$ in disordered CPs[25, 27], whereas it can approach values as high as 20 $cm^2\ V^{-1}$ in molecular crystals and of 23.7 $cm^2\ V^{-1}$ in highly aligned CPs[28], in which conductivity can be also described by delocalised transport[29].

1.2 Optoelectronic devices

1.2.1 Organic Solar Cells

An important area of application of organic semiconductors is as active layer in organic photovoltaic diodes (OPVs). The advantages of using organic materials in photovoltaic cells stems from their relatively high absorption coefficient ($\alpha \sim 10^5\ cm^{-1}$)[30] that balances partly their low charge carriers mobility, and from the opportunity to fabricate OPVs over large area using cheap solution-based processes. The photo-conversion process in OPVs occurs in four main steps:

i. Generation of bound excitons (electron/hole pairs) upon photon absorption;
ii. Dissociation of excitons into free charges at the electron donor/electron acceptor interface;
iii. Charge transport through the active layer;
iv. Charge extraction from the donor or acceptor domains into the electrodes.

As the efficiency of the photo-generation process relies on the splitting of the strongly bound excitons, this class of devices are termed *excitonic solar cells*, to distinguish them from the *non-excitonic* devices, in which free charges are formed already at RT. Despite these drawbacks, which have a large effect in design criteria and efficiency of OPVs, the flexibility for chemical modifications on organic semiconductors as well as the promise of being a flexible and low-cost alternative to inorganic solar cells is the driving-force for the development of this promising class of devices.

1.2.1.1 Characteristics of solar cells

The current-voltage characteristic of a photovoltaic diode in the dark and under illumination allows the extraction and evaluation of both its electric behaviour and photovoltaic performances. Figure 1.6 shows a typical I-V curve for a photovoltaic diode. The short-circuit current (I_{sc}) is the current measured under illumination when the cell is short-circuited: this is the maximum current delivered by the diode. Such a quantity depends mainly on three parameters namely: i) the fraction of absorbed photons, which in turn is a function of the absorption spectrum, absorption coefficient and the thickness of the absorbing layer; ii) the fraction of dissociated excitons, which is optimal when the phase separation between the electron donor and electron acceptor domains matches the characteristic exciton diffusion length of the system; iii) the fraction of charges that reach the electrodes, which is lowered by the presence of charges recombination centres throughout the active material, tipically traps and impurities. The voltage measured when the current flows in the device is zero (maximum voltage according to the Ohm's law), corresponding to almost flat conduction and valence band, is called open circuit voltage (V_{oc}). The open circuit voltage provides the primary driving force for charges separation, and can be linked directly to the energy difference between the HOMO level of the donor and the LUMO level of the acceptor material. In addition, such parameter depends heavily on the quality of the electrode/active layer interfaces, as the presence of defects at the interfaces or short circuit pathways (i.e. pinholes or cracks in the active film) lead to an increase of the resistivity offered by the material and , thus, to a lowering of the *Voc*.

The point on the I-V curve giving the maximum power of this product is the maximum power point (P_{max}), whereas the ratio between the maximum power and the external short and open circuit values is called fill-factor (*FF*) (equation 1.2): as the P_{max} cannot exceeds the $I_{sc} \times V_{oc}$ product, *FF* is always less than one.

$$FF = \frac{\mathrm{I_{Pmax}} \times \mathrm{V_{Pmax}}}{\mathrm{I_{SC}} \times \mathrm{V_{OC}}} \ . \qquad (1.2)$$

The fill-factor is a key value in evaluating the performance of a photovoltaic device and it measures the "squareness" of the I-V curve. For an ideal diode the curve would be rectangular (FF = 1), however for real cells it is less than one because of losses or shunt resistances. The power yield of the solar cell is expressed in terms of power conversion efficiency (η) and it is the ratio between the maximum power delivered by the cell and the incident power P_{light} (equation 1.3).

$$\eta = \frac{\mathrm{P_{max}}}{\mathrm{P_{light}}} . \qquad (1.3)$$

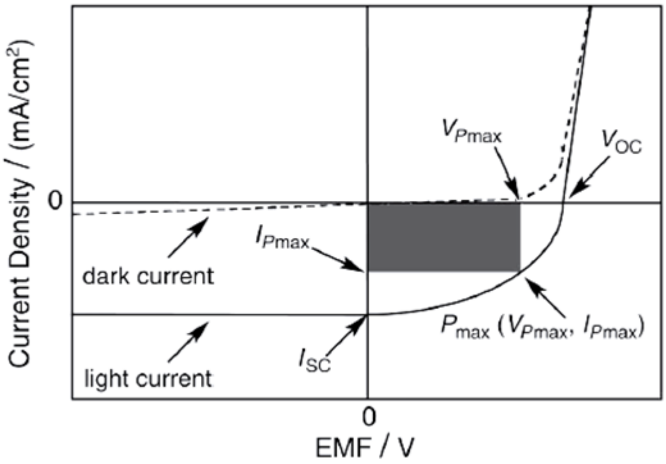

Figure 1.6: Current-Voltage curve for a photovoltaic device (dotted line in dark and solid line under illumination). Adapted from reference [31].

As the efficiency of a photovoltaic device depends on the temperature as well as the spectral distribution of the light intensity, it is hence necessary to define standard measurement conditions in order to compare between measurements made in different laboratories. The standard condition is defined as the measurement taken at 25 °C using a light intensity of 1000 W m^{-2} and a solar spectral distribution AM (air mass) 1.5 global standard solar spectrum, which is the solar distribution of wavelength as an incidental solar ray in a 48.2° angle.

1.2.1.2 Architecture of organic solar cells

The first generation of OPVs was based on a single layer of an organic absorber sandwiched between two electrodes with different work functions[32, 33]. This device configuration corresponds to a metal-insulator-metal diode, in which the rectifying behaviour was attributed to the asymmetry in the electron and hole injection into the molecular π and π^* orbitals, respectively. However, in this configuration the asymmetry in the electrodes work functions (usually Al or Ca) was not large enough to allow an effective photoinduced charge generation, limiting the efficiency of these devices in the range 10^{-3}-10^{-2} %. In order to overcome this drawback and limit losses due to charge recombination, the bilayer heterojunction architecture was proposed[34]. In this configuration, two layers of organic materials, with specific electron and hole transporting properties, were sandwiched between the electrodes. Tang reported an efficiency of ~1% using a phtalocyanine derivative as p-type semiconductor and a perylene derivative as n-type semiconductor sandwiched between a transparent conducting oxide and a semi-transparent metal electrode.

The demonstration of ultrafast charge transfer between conjugated polymers and fullerene derivatives[35, 36], led to the introduction of the type-II bulk heterojunction (BHJ) architecture (figure 1.7)[5, 6]. A bulk heterojunction material is in-fact a solid blend composed of an electron-donor and electron-acceptor material, with a nanostructured morphology formed by spontaneous phase separation between the two components. As the typical exciton diffusion length in CPs is ~ 10 nm, the length scale of such phase separation should be within 10-20 nm. Such a percolated and interpenetrated network has the potential to provide both the large interface area and, upon careful selection of the materials, the driving force necessary for exciton splitting and efficient charge generation. Although BHJ devices are among the best performing at present, a clear structure-performance relationship has yet to emerge due to the complex multicomponent nature of the solid blend.

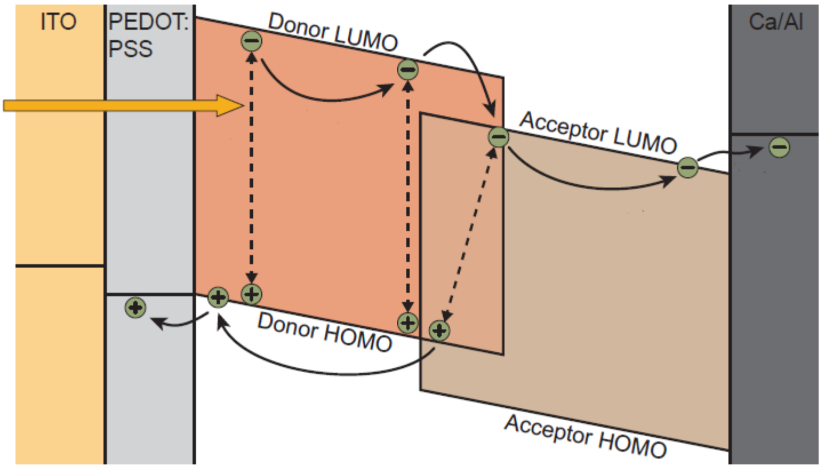

Figure 1.7: Typical type II heterojunction architecture. Light enters the cell through the Indium-Tin oxide electrode (ITO) and the hole-injection layer material (poly(3,4-ethylenedioxthiophene):poly(styrene sulfonate)(PEDOT-PSS) and get absorbed predominantly by the donor material: this creates an hole-electron couple (exciton). In order to be split into free charges, the exciton has to diffuse at the electron-donor/electron acceptor interface within its lifetime. The exciton splitting leads to the formation of free electrons and holes which eventually are collected to their respective electrodes (adapted from ref.[20]).

The current paradigm for BHJ organic solar cells is represented by blends of poly(thiophenes) and fullerene derivatives, for example in its most popular incarnation based on regioregular P3HT as electron donor and PCBM as electron acceptor (figure 1.8).

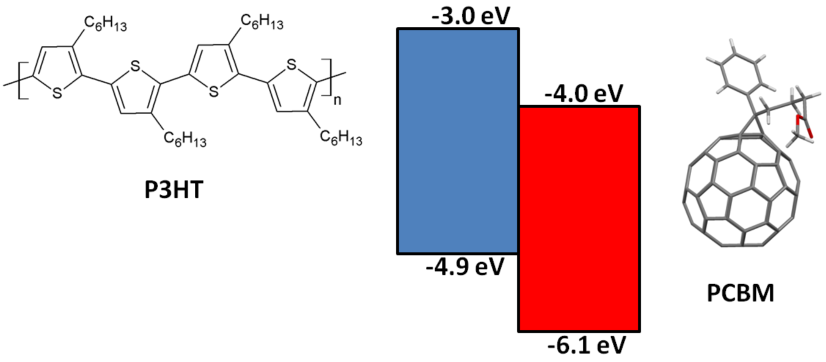

Figure 1.8: P3HT-PCBM type II heterojunction. Note that the position of the LUMO and HOMO of P3HT and PCBM makes these materials suitable for a type II BHJ.

1.2.2 Organic Field-Effect Transistors

The key advantage of using organic semiconductors as active material of thin film transistors stems from the promise of being integrated in plastic-based and low-cost circuits, especially in those employing field-effect transistors (FETs) such as logic and switching elements[37].

The possibility to amplify an electric signal by means of the field-effect phenomenon was firstly demonstrated by Lilienfeld[38]. The modulation of the resistance (current) in the active element by applying a voltage is the key physical principle that leads to the amplification and switching properties offered by FETs. A typical FET structure is shown in figure 1.9a, and contains the following elements: i) a semiconducting layer , ii) a dielectric layer, iii) two electrodes called *Source* (S) and *Drain* (D) that enable charge injection and extraction and iv) a separate *Gate* (G) electrode that permits to modulate the resistance of the semiconductor layer at the interface with the dielectric material (channel). For instance, when a negative voltage is applied to the gate electrode the dielectric capacitive layer is negatively charged and, hence, a positive channel is induced at the interface between the dielectric and the semiconductor. Therefore, a *D-S* positive current (holes) modulated by the gate voltage can be observed when a *D-S* voltage is applied (fig. 1.9b, FET output characteristic): this corresponds to the *ON* state of the transistor.

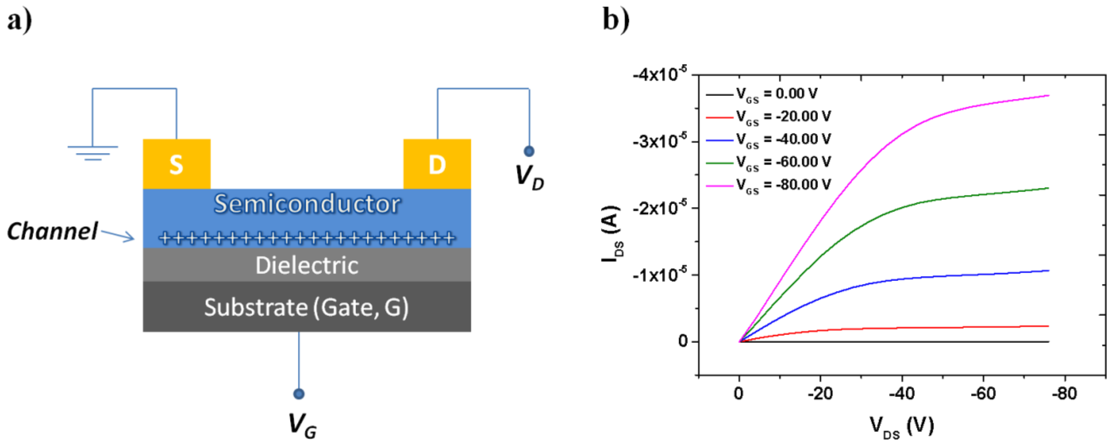

Figure 1.9: a) Sketch of a "top-contact" FET. In the alternative "bottom-contact" configuration, the electrodes are on top of the semiconductor/dielectric interface. b) Output characteristic of P3HT-based OFET (channel length 5 µm).

The important parameters to assess the performances of FETs are the field-effect mobility (μ), the threshold voltage (V_t) and the on/off current ratio (I_{ON} / I_{OFF}). The mobility describes the average charge carriers drift per unit electric field, and quantifies the processing speed of a FET device. As μ depends on the magnitude of the gate voltage, it is in-fact a field-effect dependent mobility. Threshold voltage (V_t) is the minimum gate voltage necessary to induce a conductive channel in the semiconductor layer and to turn-on the device. Therefore, V_t determines the goodness of the switching behaviour of a FET. The I_{ON} / I_{OFF} is the current intensity ratio between the *on* and the *off* states of the FET, and it is the figure of merit for having high performance (high I_{ON}) and low leakage power (low I_{OFF}) for a transistor.

The field-effect mobility can be calculated from equation 1.4, which describes the relation between the drain-source current at a given gate voltage and the mobility. In this expression, W and L represent the channel width and length of the device and C is the capacitance per unit area of the dielectric. In practice, by calculating the square root of the I_{DS} vs. V_G plot (figure 1.10) and taking its slope, we obtain $(WC/2L\mu)^{1/2}$, from which the mobility can be extracted.

$$I_{DS} = \frac{WC}{2L}\,\mu(V_G - V_T)^2 \;, \qquad (1.4)$$

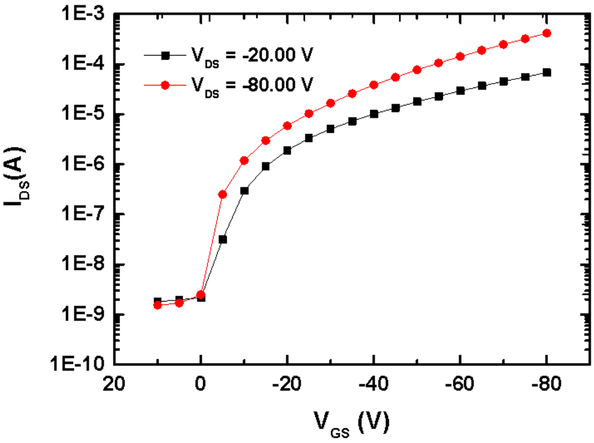

Figure 1.10: Transfer characteristic for a P3HT-based OFET, taken in linear (VGS = -20 V) and saturation (VGS = -80 V) regime (channel length 5 μm).

A large number of organic semiconductors have been employed as active layer in OFETs. The first experiments in this field were carried out using p-type thiophene oligomers[39] and electrodeposited polymers[40], which exhibit FET mobilities ~0.01 cm^2 V^{-1} and $I_{ON} / I_{OFF} < 100$. Since then, a plethora of materials, mostly exhibiting p-type conductivity, have been developed and integrated in OFETs. This, alongside the optimisation of device architecture, has allowed researchers to obtain mobilities approaching and exceeding the one of amorphous silicon (~ 1 cm^2 V^{-1}). Although highly pure, uniform and reproducible devices can be fabricated by using vacuum sublimation and thermal evaporation techniques, solution-processable polymers permit to fabricate large-are and low-cost devices, and hence are more technologically appealing. These materials, which include poly(alkyl thiophenes)[7], liquid-crystalline thieno-thiophene copolymers[41] and indacenodithiophene–benzothiadiazole copolymers[42], exhibit mobilities ranging from 0.1 cm^2 V^{-1} to 5 cm^2 V^{-1}. The tremendous improvement of OFETs performances have facilitated the effective employment of these devices in a number of new applications, including flexible display and 8-bit microcontrollers[43].

2 Neutron scattering theory and neutron-based techniques

Neutron scattering techniques represent a powerful set of methods to investigate a very wide range of features in condensed matter. The advantage of using neutron scattering techniques arises from the basic physical properties of neutrons.

The fact that neutrons are uncharged particles means that they can penetrate deeply into materials, allowing us to obtain valuable information about the bulk of the sample. Such a peculiar property also results in a different neutron-matter interaction mechanism in comparison with other particles or photons, i.e electrons and X-rays: whereas neutrons are scattered by strong and very short (~ 10^{-14} nm) nuclear forces, electrons and X-rays are deflected by the electronic clouds. For instance, neutrons are scattered strongly by the light hydrogen atoms while X-rays and electrons are weakly deflected by highly hydrogenated materials, meaning that neutron scattering techniques are particularly advantageous for investigating organic matter. Furthermore, neutrons possess a magnetic moment and, thus, can be employed effectively in the investigation of the arrangement of electron spins and the energies of magnetic excitations. Finally, yet importantly, the spectrum of neutron energies obtained in neutron sources is extremely wide (typically from 0.025 eV to hundreds of MeV), as neutron velocity (wavelength) can be tuned by means of thermalisation with a medium at a given temperature. This means that the various portions of the neutron spectrum can be employed for different experimental purposes, i.e. neutron diffraction and spectroscopy (thermal neutrons ~25 meV) and neutron damage testing (fast neutrons > 0.1 MeV).

In section 2.1, I will discuss about scattering theory and neutron sources, while in section 2.2, I will give some details about some of the experimental techniques relevant to my work. The content of this chapter is based on a wide range of literature sources, such as textbooks[44-46] and lecture notes[47, 48].

2.1 Scattering theory and neutron sources

2.1.1 Momentum transfer vector

The basic mathematical/physical formalism that is reviewed in this section can be applied to both neutron and X-ray scattering. For simplicity, we start from an idealised scattering experiment, in which we deal with fixed scattering centres and scattering is solely elastic (no energy exchange).

The scattering of photons or particles by a sample is characterised by a change in their momentum $\boldsymbol{P}$, and energy E. The change in momentum can be expressed by the following equation:

$$\boldsymbol{P} = \hbar \boldsymbol{k_i} - \hbar \boldsymbol{k_f} = \hbar \boldsymbol{Q} \ , \tag{2.1}$$

with $\hbar = h/2\pi$, $\boldsymbol{k_i}$ and $\boldsymbol{k_f}$ the wavevectors of the incident and scattered waves respectively, and $\boldsymbol{Q} = \boldsymbol{k_i}$-$\boldsymbol{k_f}$. Similarly, the energy transfer can be expressed as:

$$E = \hbar\omega_i - \hbar\omega_f = \hbar\omega \ , \tag{2.2}$$

where ω represent the angular frequency and $\omega = \omega_i - \omega_f$.

In a scattering experiment, we compare the energy and momentum of the incident and scattered particles. These information are encoded in a four-dimensional function S $(\boldsymbol{P}, E)$, which is called the scattering law, and is traditionally expressed as S $(\boldsymbol{Q}, \omega)$. In the case of purely elastic scattering E = 0, and hence the scattering law is only function of the momentum transfer S $(\boldsymbol{Q})$**.** This also means that the modulus of the incident and scattered wavevectors are identical,

$$|\boldsymbol{k_i}| = |\boldsymbol{k_f}| = \frac{2\pi}{\lambda} \ . \tag{2.3}$$

Let us now focus on the mathematical definition of the momentum transfer wavevector. Figure 2.1a shows the geometry of an ideal elastic scattering event involving only one scattering centre. From eqn. 2.3, the scattering triangle $\boldsymbol{k_i}$ - $\boldsymbol{k_f}$ - $\boldsymbol{Q}$ is isosceles, with $\boldsymbol{k_i} = \boldsymbol{k_f}$ and, thus, elementary trigonometry leads to the expression:

$$\boldsymbol{Q} = \frac{4\pi \ sin\theta}{\lambda} \ , \tag{2.4}$$

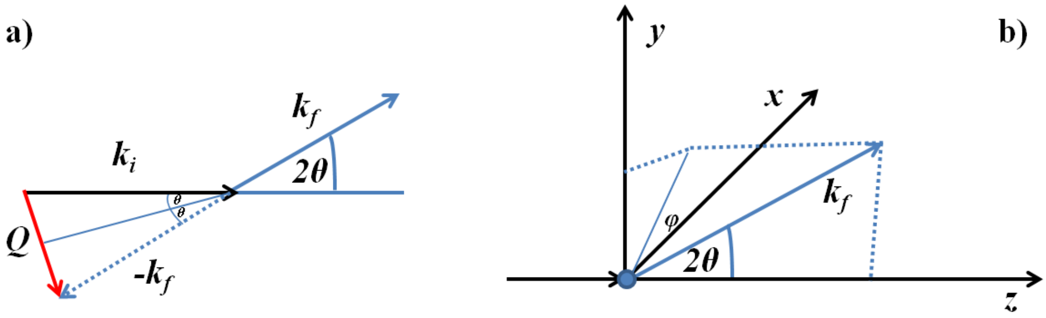

Figure 2.1: a) The scattering geometry for an elastic scattering event through a scattering angle of 2θ; b) scattering geometry in spherical polar coordinates.

To take into account the rotations of the wavevectors and define the momentum transfer vector in terms of spherical polar coordinates, we need to introduce another angle φ (figure 2.1b). This more complete definition can be written as[45]:

$$\boldsymbol{Q} = \frac{4\pi \sin\theta}{\lambda}(-\cos\theta \cos\varphi, -\cos\theta \sin\varphi, \sin\theta)\ . \tag{2.5}$$

2.1.2 The differential cross section

The physical quantity that is measured during a scattering experiment is the ratio between the number of scattered particles at a given 2θ and φ per unit solid angle subtended by the detector ($\Delta\Omega$), and the flux of incident particles per unit area of beam (ϕ). Such a quantity, in the limit of $\Delta\Omega \rightarrow 0$, is known as the *differential cross section* and has the dimension of an area per unit solid angle (equation 2.6):

$$\frac{d\sigma}{d\Omega} = \lim_{\Delta\Omega\rightarrow 0} \frac{R(2\theta,\varphi)}{N\,\phi\,\Delta\Omega}\ , \tag{2.6}$$

where $R(2\theta,\varphi)$ represents the rate of arrival of deflected particles per unit time (s^{-1}) and N is the number of scattering centres. This function can translated into the elastic scattering law $S_{el}(\boldsymbol{Q},\omega)$, by simply transforming the $(2\theta,\varphi)$ directions into the related values of the momentum transfer vector $\boldsymbol{Q}$ with equation 2.5. Note that those quantities are expressed in the limit case of purely elastic scattering, whereas in reality both elastic and inelastic scattering interactions are observed. The difference between the elastic and total scattering differential cross sections is the focus of inelastic scattering experiments.

2.1.3 Scattering by a single atom

After having defined some important quantities to rationalise the scattering process, we now try to understand how the inner structure of the sample at the atomic level, can be related to the scattering data. Let us thus consider the elastic deflection of particles by a single fixed atom. The mathematical form of a steady stream of incident particles travelling along the z-direction can be described by the complex plane wave:

$$\psi_i = \psi_0 e^{ikz} \ . \tag{2.7}$$

Because the incident particles (i.e. neutrons and x-rays) see the nuclei and the electron clouds as points, the scattering will be isotropic and the scattered wave will be spherical with amplitude depending on *1/r* (figure 2.2). If the origin of the system is conveniently placed on the atom so that the wavevector of the scattered wave $\boldsymbol{k_f}$ *is* parallel to the displacement vector ***r***, the form of the sinusoidal part of the scattered wave is $e^{i\boldsymbol{kr}}$ and the scattered wave can be expressed as:

$$\psi_{sc} = \psi_0 \, f(\lambda, \theta) \frac{e^{i\boldsymbol{kr}}}{\boldsymbol{r}} . \tag{2.8}$$

The function $f(\lambda,\theta)$ modulates the amplitude of ψ_i and, as it depends on the interaction mechanism and strength between incident particle and atom, and its nature is extremely different between X-rays and neutron scattering. For neutrons, $f(\lambda,\theta)$ is, to good approximation, invariant with respect of scattering angle and wavelength, and it is called *scattering length, b*:

$$f(\lambda, \theta) = \ -b \, . \tag{2.9}$$

The minus sign is a matter of convention, and denotes that *b* is a positive number for a repulsive interaction between neutron and nucleus. The isotropic scattering upon neutron/nucleus interaction originates from the relatively short interaction length (~10^{-14} m) then the wavelength of thermal neutrons (~ 10^{-10} m). Therefore, neutrons deflection occurs equally in all directions (figure 2.2).

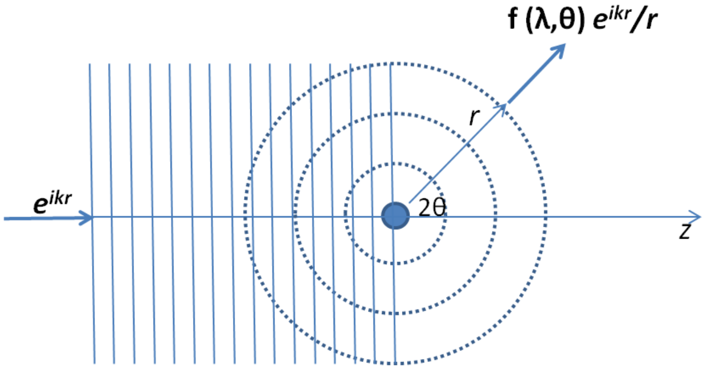

Figure 2.2: Neutrons isotropic and elastic scattering event by a single fixed atom. Note that for neutrons the *f (λ,θ)* function is known as scattering length *b*.

It is worth noting that the invariance of the scattering length vs. λ holds from most nuclei within the range of thermal neutrons. However, some nuclei such as indium and cadmium, in the close vicinity of certain wavelengths exhibit the neutron absorption phenomenon, which implies the existence of the imaginary part of *b* associated with neutron absorption at the resonance wavelengths.

In stark contrast to the *atomic form factor* for x-rays that increases with the atomic number *Z*, neutron scattering lengths display an erratic variation vs. Z and, in addition, is isotope specific. For instance, the hydrogen nucleus has $b = -0.374 \times 10^{-14}\,m$, whereas for deuterium $b = -0.668 \times 10^{-14} m$[10]. This illustrates that, given the large difference in b between hydrogen and deuterium, deuteration is a valid experimental trick to highlight/suppress the signal from a certain region of the sample and obtain detailed atomistic information about the inner structure of the material. By integrating the differential cross section over all angles and combining equations 2.6, 2.8 and 2.9, we obtain the relationship between the total cross section and the scattering length density:

$$\sigma = 4\pi|b|^2 \ . \tag{2.10}$$

2.1.4 Scattering from an assembly of atoms

The scattering geometry for the scattering from an assembly of atoms is reported in figure 2.3. In this case the contribution of the j^{th} atom to the total scattered wave is:

$$\left[\delta\psi_f\right]_j = \psi_0 e^{i\boldsymbol{k}_i\cdot\boldsymbol{R}_j}\, f_j(\lambda,\theta)\frac{e^{i\boldsymbol{k}_f\cdot(\boldsymbol{r}-\boldsymbol{R}_j)}}{|\boldsymbol{r}-\boldsymbol{R}_j|}\ , \tag{2.11}$$

where $\mathbf{R}_j$ is the arbitrary position of the j^{th} atom and $f(\lambda,\theta)$ is the particle-scatterer interaction function, which for neutron represents the scattering length density b and for x-rays is the atomic form factor. Although equation 2.11 looks more complex than eqn. 2.8, it can be linked to the simpler case of monatomic scattering when $\boldsymbol{R}_j = 0$. If the scattering process is weak and linear, as the infinitesimal scattered wavelets have no effect on the incident beam (*kinematical approximation*), by simply applying the superposition principle we obtain that the outgoing scattered wave is:

$$\psi_f = \psi_0 e^{i\boldsymbol{k}_f\cdot\boldsymbol{r}} \sum_{j=1}^{N} f_j(\lambda,\theta)\frac{e^{i\boldsymbol{Q}\cdot\boldsymbol{R}_j}}{|\boldsymbol{r}-\boldsymbol{R}_j|}, \tag{2.12}$$

where $\boldsymbol{Q} = \boldsymbol{k}_i - \boldsymbol{k}_f$ is the wavevector transfer. Multiple scattering is also neglected in eqn. 2.12, even though the occurrence of such events is usually minimised by adjusting the sample transmittance to ~ 90% for most of neutron scattering experiments.

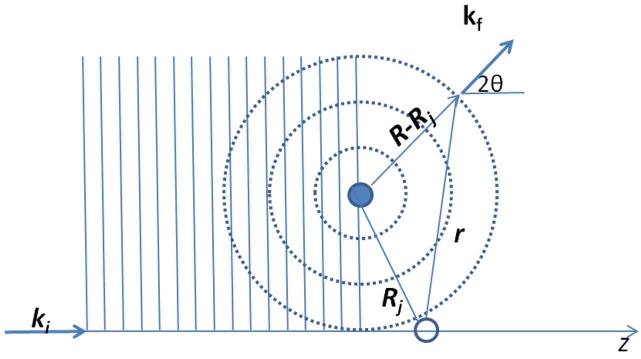

Figure 2.3: Scattering contribution to the total scattered wave from an atom j placed at $\boldsymbol{R}_j$.

In a typical scattering experiment, the sample-detector distance is considerably larger than the sample size and hence $|\boldsymbol{r}-\boldsymbol{R}_j| = |\boldsymbol{r}| = r$. Under this assumption (far-field limit), the intensity of the scattered wave is:

$$|\psi_f|^2 = \frac{\phi}{r^2}\left|\sum_{j=1}^{N} f_j(\lambda,\theta)\, e^{i\boldsymbol{Q}\cdot\boldsymbol{R}_j}\right|^2, \tag{2.13}$$

and, as the scattering rate $R(2\theta,\phi) = |\psi_f|^2\delta A$, the differential cross section of equation 2.6 can be rewritten as:

$$\frac{d\sigma}{d\Omega} = \left|\sum_{j=1}^{N} f_j(\lambda,\theta)\, e^{i\boldsymbol{Q}\cdot\boldsymbol{R}_j}\right|^2. \tag{2.14}$$

The summation over all the scattering centres of *f (λ,θ)* can be also expressed in terms of density of scattering lengths at a given location R and dV, so that $f\ (\lambda,\theta) = \beta(R)dV$. This $\beta(R)$ function is known as *Scattering Length Density (SLD)* and in the SI is expressed in m^{-2}. If we substitute this quantity in eqn. 2.14 and integrate over all the volume, we obtain the following generalisation:

$$\frac{d\sigma}{d\Omega} \propto \left|\iiint \beta(R)\, e^{i\boldsymbol{Q}\cdot\boldsymbol{R}} d^3\,\boldsymbol{R}\right|^2 \propto S(\boldsymbol{Q})\,. \tag{2.15}$$

This expression has a huge practical meaning, as it denotes that the experimental observable (differential cross section) in a scattering experiment can be related to the scattering law S ***(Q)*** and hence to the inner structure of the sample, through the Fourier transform of its *SLD* function.

In the case of the nuclear scattering of neutrons, where the scattering lengths depend on the isotope and the spin state of the nuclei, the $\beta(\boldsymbol{R})$ function can be divided into two parts: an average SLD function $< \beta(\boldsymbol{R}) >$, which accounts for the coherent scattering arising from identical nuclei with the same spin state, and a set of random deviations of SLD, $\Delta\beta(\boldsymbol{R})$. The former function contains all the information about the inner structure of the sample and/or the nuclear coherent motions, whereas the latter originates from the incoherent random fluctuations of the isotopes and spin states and/or from the incoherent self-particle motions.

$$\beta(\boldsymbol{R}) = < \beta(\boldsymbol{R}) > + \Delta\beta(\boldsymbol{R})\,, \tag{2.16}$$

The Fourier transforms of equation 2.16 is proportional to the scattering law and, hence, we obtain:

$$S(\boldsymbol{Q}) \propto < \lfloor < F\ (\boldsymbol{Q}) + \ \Delta F(\boldsymbol{Q}) \rfloor^2 > \ , \tag{2.17}$$

which can be expressed as:

$$S(\boldsymbol{Q}) = S(\boldsymbol{Q})_{\boldsymbol{coh}} + \ S(\boldsymbol{Q})_{\boldsymbol{incoh}}\ \ . \tag{2.18}$$

Defined spatial patterns and collective motions (as in magnetic excitations and phonons) give rise to coherent scattering, Incoherent scattering is valuable because it allows us to map-out atomic self-diffusions as a function of $\boldsymbol{Q}$.

2.1.5 Inelastic scattering and correlation function

After having discussed the basic mathematic formalism underpinning the elastic scattering process, we now turn to the case where there is an exchange of energy and momentum between the incident particles and the sample. Therefore, the scattering law is now function of both Q and ω and the scattering triangle is no longer isosceles, as $|\boldsymbol{k_i}| \neq |\boldsymbol{k_f}|$ (figure 2.4).

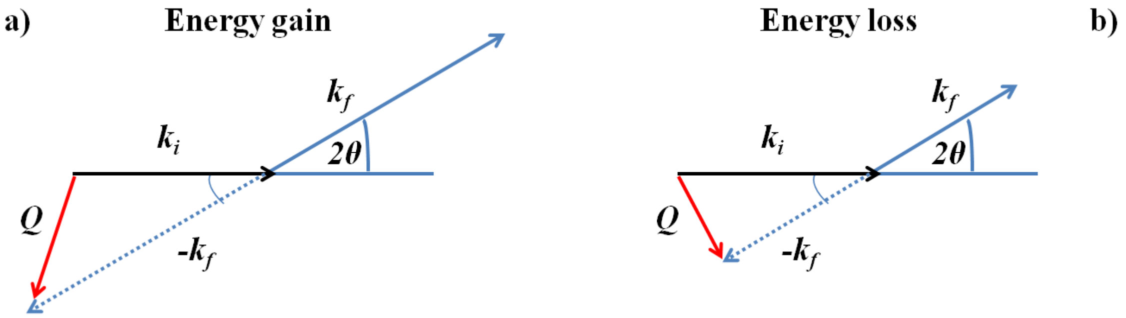

Figure 2.4: The scattering triangle for inelastic scattering in the case of a) energy gain and b) energy loss.

Therefore, in this inelastic case the modulus of the momentum transfer wavevector can be expressed as:

$$\boldsymbol{Q}^2 = \boldsymbol{k}_i^2 + \boldsymbol{k}_f^2 - 2\boldsymbol{k}_i\boldsymbol{k}_f \cos\theta, \tag{2.19}$$

and equation 2.5, which take into account the spherical polar coordinates, can be rewritten as:

$$\boldsymbol{Q} = \frac{2\pi}{\lambda_f}\left(-\sin 2\theta \cos\theta, -\sin 2\theta \sin\varphi, \frac{\lambda_f}{\lambda_i} - \cos 2\theta\right). \tag{2.20}$$

In addition, the expression of the differential cross section has to include a term that accounts for the exchange of energy, and has to express the probability of scattering per unit solid angle and per unit energy transfer:

$$\frac{d^2\sigma}{d\Omega \mathrm{dE}} = \lim_{\substack{\Delta\Omega\to 0 \\ \Delta\mathrm{E}\to 0}} \frac{R(2\theta,\varphi)}{N\,\phi\,\Delta\Omega\Delta\mathrm{E}} \ . \tag{2.21}$$

Such a quantity is termed *double differential cross section* and represent the experimental observable in inelastic scattering experiments, in which actually we take into an account the effect of neutrons-nuclei energy transfer as a function of $\boldsymbol{Q}$, by recording the neutron scattered into dΩ after having transferred a quantity of energy d*E*.

To derive the basic equations of inelastic scattering, we have to take into account the time evolution of our system and, hence, we need to remove the temporal restriction on the SLD, so that β (***R***,*t*) in the dynamic case. Following the same formalism employed in the static elastic case, equation 2.7 that describes the incident wavefunction can be written as:

$$\psi_i = \psi_0 e^{(i\boldsymbol{kz}-\,\omega_i t)} \ , \tag{2.22}$$

and equation 2.11 becomes:

$$d\psi_f = \psi_0 e^{(i\boldsymbol{k_i r}-\omega_i t)}[\beta(\boldsymbol{r},t)d^3\boldsymbol{r}dt]\, f_j(\lambda,\theta)\frac{e^{i[\boldsymbol{k_f}\cdot(\boldsymbol{r'}-\boldsymbol{r})-\omega_f t]}}{|\boldsymbol{r'}-\boldsymbol{r}|} \ , \tag{2.23}$$

which describes the contribution of a scattered wavelet to the outgoing wavefunction at *r'* due to the *SLD* in a *dV* centred at *r* between *t* and *t* + *dt*. In the far-field limit and following the same generalisation reported for equation 2.15, we can write:

$$\frac{d^2\sigma}{d\Omega \mathrm{dE}} \propto \frac{\lambda_f}{\lambda_i}\left|\iiint \beta(\boldsymbol{r},t)\; e^{i(\boldsymbol{Q}\cdot\boldsymbol{r}-\omega t)} d^3\,\boldsymbol{r}\; dt\right|^2 \propto S(\boldsymbol{Q},\omega). \tag{2.24}$$

Note that we also include the ratio between the final and incident wavelength in equation 2.24, because in the inelastic case the incident and scattered flux also depend on how fast the particles are moving. The scattering law S (***Q***, *ω*), also defined as *dynamical structure factor*, encodes both structural (space) and dynamical (time) information, and it is essentially the modulus-squared of the space-time Fourier transform of β (***R***,*t*). The time-dependence of **S** (***Q***, *ω*) is usually expressed in terms of Van Hove space-time correlation function **G (*r*, *t*)**[49], which quantifies the correlation between pairs of scatterers that are separated by a displacement *r* and a time *t*:

$$G(\boldsymbol{r},t) = \iiint \beta(\boldsymbol{r},t)^{*}\beta(\boldsymbol{r}+\boldsymbol{R},t+t')d^{3}\,\boldsymbol{R}\,dt. \tag{2.25}$$

It is, in-fact, the auto-correlation function of β (***R***, *t)*[45], and it is linearly related to the scattering function:

$$\frac{d^{2}\sigma}{d\Omega \mathrm{dE}} \propto \frac{\lambda_f}{\lambda_i}\iiint G(\boldsymbol{r},t)\; e^{i(\boldsymbol{Q}\cdot\boldsymbol{r}-\omega t)}d^{3}\,\boldsymbol{r}\,dt. \tag{2.26}$$

Given the presence of the modulus-squared in equation 2.24, it is usual difficult to infer β (***R***, *t)* from the double differential cross-section. For this, in scattering experiments the dynamical structure factor is conveniently Fourier transformed in time to give the intermediate scattering function I (*q*, *t*), and in time and space to obtain the Van Hove function G (***r***, *t*).

In the case of elastic scattering, the coherent contribution arises from the part of *SLD* that exhibits a discernible spatial pattern and the incoherent signal from the random variability of the scattering lengths (i.e. different isotopes and nonzero nuclear spin). Analogously, the inelastic coherent signal tells us about the collective motions and excitations (i.e. phonons and magnons), whereas the inelastic incoherent scattering originates from the correlations between the positions of the same nucleus at different times (i.e. single atoms diffusion). As the hydrogen atom exhibits the highest values of incoherent cross section among the isotopes[10], incoherent scattering carries spectroscopic information about the dynamic of hydrogen-rich materials, such as biomolecules and macromolecules.

2.1.6 Neutron polarisation analysis

For most of the neutron scattering experiments, the incident neutron beam is not polarised and the population of neutrons with parallel and anti-parallel magnetic dipole is equal. Nonetheless, the use of a polarised neutron beam and the analysis of its polarisation upon scattering can disclose useful information. There are three main methods of beam polarisation, namely: i) polarising filters, which rely on the preferential absorption by polarised ^{3}He nuclei); ii) polarising crystals (i.e. $Co_{92}Fe_8$ crystals); iii) polarising mirrors and super mirrors. The polarisation of the beam is then maintained by applying a magnetic guide field along the beam, and the neutrons with magnetic moment parallel to the guide field are said to be *up*, whereas if the moment is antiparallel are said to be *down*. A polariser is called *up* if does not transmit *down* neutrons and vice versa. In this way, the scattering law for those neutrons for which the scattering process does not alter the magnetic moment can be measured by inserting an *up* polariser before and after the sample. To measure the scattering law for the other processes, for instance *down* neutrons flipped to *up*, an additional polarisation component is required. This can be performed by a *flipper*, which is a device that can change the direction of a neutron magnetic moment from *down* to *up* and vice versa. Therefore, if the instrument is equipped with polarisers before and after the sample and a flipper device is inserted on either side of the sample, the scattering law for all the processes (*up* to *down*, *down* to *up* and so on) can be measured by simply switching *on/off* the flipper. This technique is called neutron polarisation analysis, and can be applied effectively to investigate those scattering processes that flip the magnetic moment of neutrons.

For instance, if we assume that the incoherent signal is mainly *spin-incoherent* and not *isotope-incoherent*, polarisation analysis can be employed to discriminate between *coherent* and *incoherent* signal. Such a separation is vital for those systems in which the collective coherent dynamical motions can intrinsically affect the interpretation of the scattering data, i.e., in cases where the coherent scattering cross-sections are not negligible in comparison to the incoherent scattering cross-sections. The key principle of neutron polarisation analysis is that in the case of *spin-incoherent* scattering the neutron spin is flipped with a 2/3 probability, whereas for coherent (plus *isotope-incoherent*) scattering no such spin-flip occurs. The scattering intensities for neutron spin-flip ($\uparrow\downarrow$) and non-spin-flip ($\uparrow\uparrow$) in the limit of zero isotope-incoherent scattering are given by[50, 51]:

$$I_{\uparrow\uparrow} = I_{coh} + \frac{1}{3} I_{inc} \, , \tag{2.27}$$

and

$$I_{\uparrow\downarrow} = \frac{2}{3} I_{inc} \ , \tag{2.28}$$

and therefore the coherent and incoherent intensities can be separated according to:

$$I_{coh} = I_{\uparrow\uparrow} - \frac{1}{2} I_{\uparrow\downarrow} \ , \tag{2.29}$$

and

$$I_{inc} = \frac{3}{2} I_{\uparrow\downarrow} \ . \tag{2.30}$$

In chapter 5, we will see how neutron polarisation analysis can be applied to separate the coherent/incoherent scattering contributions in pure P3HT and in blends with PCBM.

2.1.7 Neutron sources

Neutron sources can be divided into two main categories: reactors and pulsed sources. In both the cases, the neutrons produced possess energy up to MeV, and thus are far too energetic for the investigation of condensed matter. For this reason, neutrons are conveniently slowed down through collisions with a moderating material with a large scattering cross section (i.e. hydrogen and water). During those collisions, neutrons lose energy to recoiling moderator atoms and, eventually, emerge from the moderator liquid with energies approaching the Maxwell-Boltzmann distribution of the moderator temperature. For instance, moderation with water provides an average energy of neutrons of 25 meV (1.8 Å) at RT, which is suitable for neutron diffraction experiments. On the other hand, liquid-hydrogen permits to obtain neutrons with an average energy of 5 meV (4 Å) at 25 K, which can be employed for studying slow inelastic processes (i.e. quasi-elastic scattering events).

In research reactors, neutrons are provided by fission of a fissile material that is usually uranium enriched with its less abundant isotope, ^{235}U. The fission reaction relies on the instability of ^{235}U nucleus, which breaks up in a number of different mechanisms, such as:

$$n + {}^{235}U \rightarrow {}^{236}U \rightarrow {}^{134}Xe + {}^{100}Sr + 2n.$$

The surplus of neutrons induces the fission of other ^{235}U nuclei, and thus provides the basis of a self-sustaining nuclear chain reaction. An example of reactor neutron source is *Institute Laue Langevin* in Grenoble (France), which delivers a thermal power of 57 MW.

Pulsed sources, which are based on accelerator technology, have become increasingly popular as they do not rely on fissile fuel and, hence, pose less political/social issues. In this case, a stream of high-energy protons (~ 1 GeV) collides with a heavy-metal target, knocking out neutrons and protons of the nuclei in a process called *spallation*. In these sources, neutrons are produced in short pulses that follow the same periodicity of the arrival of proton bunches at the heavy-metal target, whereas nuclear reactor have a steady neutrons output. The repetition rate depends on the neutron facility, and ranges between 10 Hz to 60 Hz. An example of neutron pulsed facility is *ISIS* in Oxfordshire (U.K) that operates at 160 kW with a repetition rate of 50 Hz (Target station 1).

Neutron scattering experiments in reactor sources are performed with a monochromatic beam, which allows to transform directly the angular deflection $(2\theta, \varphi)$ into the relative Q-values (i.e. for elastic scattering). Such monochromation process leads to a decrease of the incident flux, as the beam is damped by the wavelength selection procedure, even though the relatively high flux in such sources counterbalances partially those losses.

In pulsed sources that deliver lower fluxes, monochromation is not only extremely inconvenient but also unnecessary, as the common starting point of the neutrons permits to determine the velocity and, hence, the wavelength of each of them from the neutron *time-of-flight* (equation 2.31):

$$\lambda = \frac{h(t+t_0)}{m_n(L+L_0)} , \tag{2.31}$$

where h is the Planck's constant, t is the time, m_n the mass of neutron and L the total flight path and t_0 L_0 are small calibration offsets. The number of deflected neutrons is usually normalised against the distribution of the "white" beam before the sample, which is measured by placing a neutron monitor after the moderator.

2.2 Neutron-based techniques

2.2.1 Neutron reflectivity

Neutron reflectivity (NR) is a diffraction technique permitting to measure the thickness, roughness and chemical composition of a layered sample. Therefore, NR is an ideal tool to study static and dynamic phenomena occurring at the interfaces of a multilayer. The basic principle is to measure the rate of reflected neutrons (reflectivity) as a function of the momentum transfer wavevector, Q. In specular NR (figure 2.5), the angle at which the wave is incident on the surface equals the angle at which it is reflected and the *Q-vector* lies perpendicular to the substrate plane. For this reason, the measured reflectivity pattern $R(Q)$ encodes important structural and chemical information about the vertical composition of the sample.

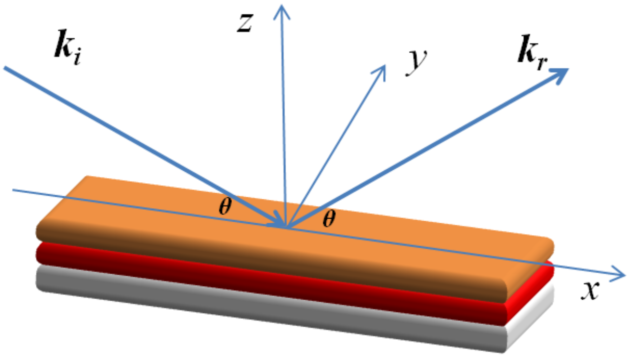

Figure 2.5: Schematic representation of specular reflectivity geometry for a layered material.

For specular reflectivity, we can assume that the scattering length density $\beta(r)$ does not change in the x-y plane, so that we can consider only the *SLD* component normal to the surface profile, $\beta(z)$.

Let us see how $R(Q)$ can be linked to the vertical structure of the sample, which is encapsulated by the linear function $\beta(z)$. The NR curve of a single layer (fig. 2.6) can be divided into two main regions. In the low-Q region, we can observe a *plateau* that is due to the total reflection of neutrons that occurs when the incident beam impinges at an angle below the critical angle (critical momentum transfer vector), θ_c (Q_c). The values of the critical parameters depend on the composition of the layer, as described by equation 2.32:

$$Q_c = 4\sqrt{\pi\beta}. \tag{2.32}$$

For neutrons, the refractive index is also related to the local composition of the sample via equation 2.33:

$$n = 1 - \frac{\beta\lambda^2}{2\pi}\ , \tag{2.33}$$

and, as n is in general very close to unity ($1-\ n \leq 10^{-4}$) the critical angle (°) is usually small for neutrons (i.e.the critical wavelength for nickel is 0.1 Å). This means that the NR experiments have to be performed at very low incidence angle and using a highly collimated beam. At *Q-values* higher than Q_c, the reflectivity curve decays with the forth power of the momentum transfer vector, obeying the Fresnel equation that, for neutrons, can be written as:

$$R \approx \frac{16\pi^2}{\boldsymbol{Q}^4}\ \left|\int_{-\infty}^{+\infty} \frac{d\beta}{dz} e^{-iz\boldsymbol{Q}} dz\right|^2. \tag{2.34}$$

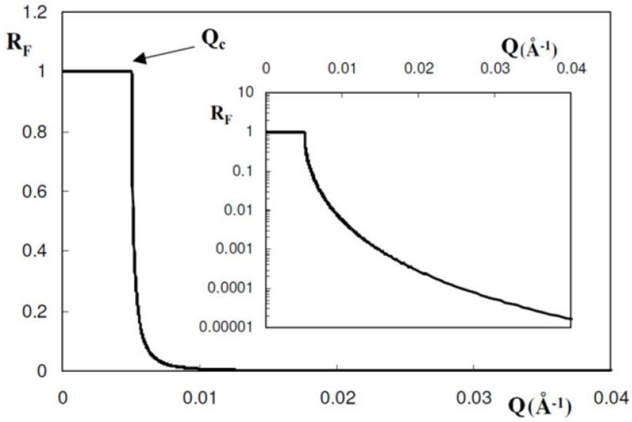

Figure 2.6: NR profile for an air/silicon interface. The inset shows the logarithmic representation of the same curve (adapted from reference [52]).

If *β(z)* is not homogeneous alongside the *z-axis*, as in the case of a layer lying on a substrate (figure 2.7a), the NR curve shows a more complex pattern (fig. 2.7b). In this case, in particular, we need to take into account three media, namely: i) the air ($n=1$); ii) layer 1 with refractive index n_1 and

iii) the substrate with refractive index n_s. In this multilayer system, with air/layer interface set at $z = 0$ and the layer/substrate interface at $z = d$, part of the beam will be reflected at $z = 0$ (k_r), and part will be transmitted for $Q > Q_C$ (k_t). Furthermore, part of this last transmitted beam will be reflected at $z = d$ ($K_{r'}$), and can interfere constructively/destructively with k_r depending on the optical path difference between the two waves. This, in turn, leads to the appearance of interfering fringes incorporated in the NR curve at given Q-values, the so-called Kiessig's fringes, whose amplitude and magnitude depend essentially on the thickness and interfacial roughness of the layers[53].

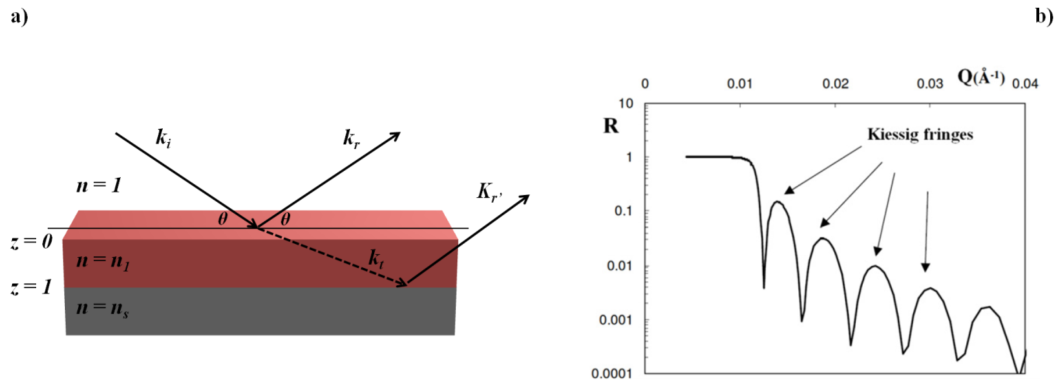

Figure 2.7: a) Specular reflectivity geometry from a multilayer system (i.e. layer onto a substrate). The constructive interference between k_r and $K_{r'}$ gives rise to the so-called Kiessig's fringes; b) NR profile for a multilayer system. The fringes amplitude and magnitude are function of the thickness and interfacial roughness (adapted from ref. [52]).

To obtain the experimental values of thickness, roughness and vertical chemical composition of the sample (*SLD* as a function of z), the NR curves are usually fitted with a model that includes the calculated *SLD* and the estimated roughness and thickness values for each layer. One of the most employed fitting model is based on the optical matrix formalism[54] that, among others, is also used for modelling the properties of other layered materials (i.e. optical features in 1D photonic crystals).

2.2.2 Quasi-elastic neutron scattering

In section 2.1, we saw that scattering is defined elastic when $\Delta\omega = 0$ or the energy exchange is below instrumental resolution, and inelastic when $\Delta\omega \neq 0$. The energy exchange landscape depicted in figure 2.8a, shows that inelastic scattering, in fact, originates from the dynamic interaction between neutrons and relatively fast motions, such as vibration modes and phonons. If the energy exchange is close to the elastic line, scattering stems from the interaction of neutrons with slower motions, such as polymer segmental motions, translation and rotations, and is defined as *quasi-elastic neutron scattering (QENS)*. As QENS signal can be seen as a broadening of the scattering law $S\ (Q,\ \omega)$ around the elastic line, the slowest observable motion is determined by instrumental resolution. *QENS* spectrometers covers timescales from ~10^{-13} to 10^{-9} seconds, and length scales within 1-30 Å[55], allowing to study a very broad range of dynamical events occurring at various length scales.

The measurement of the fraction of elastic signal as a function of temperature is called *elastic scan* (figure 2.8b), and it a useful method to locate at which temperature a given dynamical feature (i.e. rotation of polymer side-chain) enters the spectrometers time window. Having determined this, a typical *QENS* experiment proceeds with the determination of the $S\ (Q,\ \omega)$ at the temperatures and length scale of interest (figure 2.8c). To obtain direct dynamical information in the time domain, the $S\ (Q,\ \omega)$ can be converted into $I\ (Q,\ t)$ by applying a complex Fourier transform. Such a quantity, which is called the intermediate scattering function (figure 2.8d), can be fitted with a suitable model, i.e. the Kolrausch-Williams-Watts (KWW) equation for polymers[56] (see section 5.1.1 and equation 5.3).

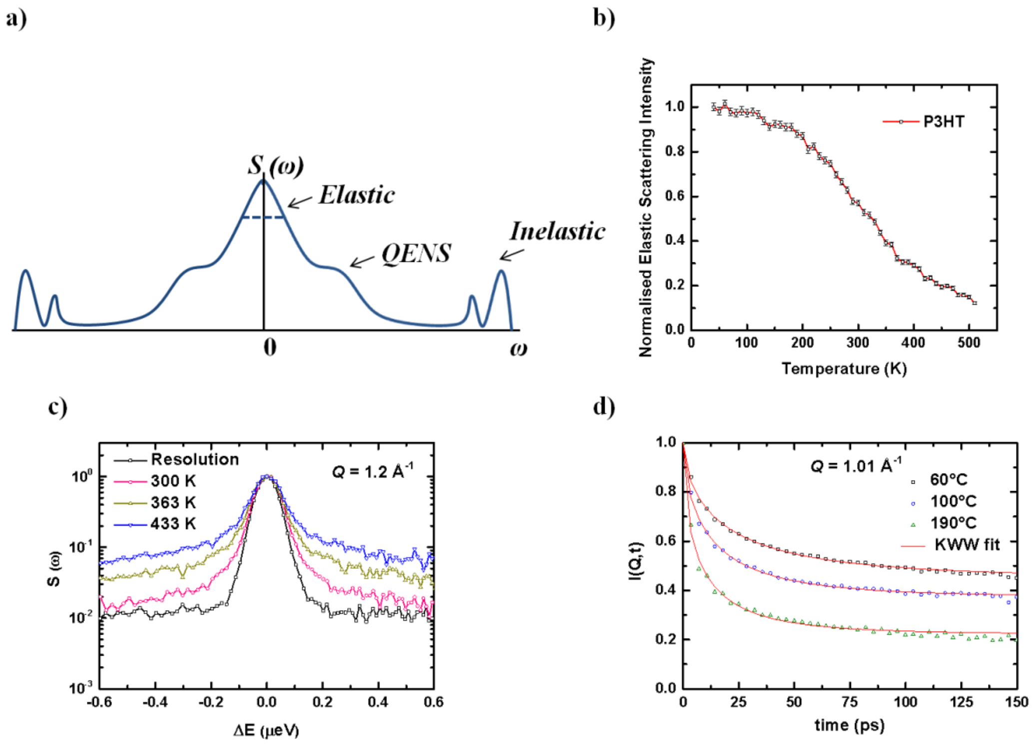

Figure 2.8: a) Representation of the scattering law at a given *Q-value* for various inelastic events. QENS scattering originates mainly from translation, rotations and polymer segmental motions, whereas inelastic scattering stems mainly from vibrations; b) Elastic scan for P3HT (normalised elastic signal vs. temperature) for a *Q*-value of 1.01 Å^{-1}; c) Scattering law as a function of temperature for P3HT (*Q*-value of 1.2 Å^{-1}); d) Intermediate scattering function vs. temperature for P3HT fitted with the KWW function.

2.2.3 Neutron irradiation testing of semiconductors

The exposure of space/aircrafts and crew to the intense cosmic rays radiation is a major concern during space exploration missions and flights. Cosmic rays are a high-intense form of radiation that originates outside the solar system, consisting mainly of protons (~ 90%) and ionised atoms (~ 10 %). The nuclear interaction of those cosmic rays with the structural shielding of spacecrafts produces a stream of highly energetic secondary neutrons. As neutrons can penetrate deeply into matter and can knock out atoms from their positions, they pose a number of hazards to both the equipments and humans hosted in the space crafts. It has been estimated that in Lunar and Mars missions scenarios, 50 % of the equivalent dose received by the crew members may come from secondary neutrons[57, 58]. A stream of secondary neutrons is also produced upon interaction of cosmic rays with the atmosphere. Those neutrons, in turn, may collide with silicon nuclei in the electronic chips, causing either reversible changes of the logic state of the circuit (i.e. single event upset) or irreversible damaging of the device[13, 14]. For these reasons, neutron irradiation is a well-established method to mimic the effect of cosmic rays on silicon-based electronics for space and avionics applications. Neutron irradiation experiments with atmospheric neutrons at different altitudes can be performed[59], however due to the low flux of neutrons they require long acquisition time. On the other hand, neutron sources can provide an intense neutron flux that can be exploited to carry out accelerated neutron irradiation tests.

For our irradiation experiment (**chapter 6**), I took advantage of the VESUVIO beamline at ISIS - Neutron and Muon source. Although VESUVIO is mainly used for neutron spectroscopy experiments[60], such a beam line has been also used for performing irradiation experiments of electronic chips[61, 62] by exploiting the availability of a wide and under-moderated neutron beam, with an energy spectrum spanning from meV to MeV[63]. To the best of my knowledge, my experiment is the first irradiation test performed on organic semiconductors and electronics.

3 Single crystals of [6,6]-phenyl-C61-butyric acid methyl ester: growth and nanoscale structural characterisation

In this chapter, I report about the preparation and nanoscale characterisation of large, high quality and solvent-free PCBM single crystals. In **section 3.1**, we present a structural/computational study of PCBM single crystals in which, by means of microfocused x-ray single-crystal diffraction and molecular dynamics simulation, we were able to resolve the intrinsic crystalline structure of PCBM. The resolution of the structure was performed by Dr. Anna Warren and Dr. Gwyndaf Evans (Diamond Light Source), and the molecular dynamics simulations by Prof. Jochen Blumberger and Dr. Jacob Spencer (University College London - Physics). In **section 3.2**, I present a detailed nanoscale morphological study of the crystals, carried out by means of traceable and metrological atomic force microscopy. The metrological AFM measurements were carried out by Dr. Giovanni Mattia Lazzerini (National Physical Laboratory).

The following chapter is reproduced with the permission of The Royal Society of Chemistry (see ref.[64]) and The American Institute of Physics (see ref.[65]).

3.1 Micro-focused x-ray diffraction characterisation of PCBM single crystals

Achieving large, high-quality, and solvent-free crystals of application-relevant organic semiconductors[66, 67] is crucial to affording ever more detailed insights into the fundamental charge and exciton physics underpinning the technology of photovoltaic diodes (PVDs), field-effect transistors (FETs), and light-emitting diodes (LEDs)[68-70]. However, this is often far from trivial, not only for high molecular weight materials/polymers such as P3HT due to chain entanglement and entropic factors, but also for smaller molecular weight materials such as PCBM, owing to inclusion of solvent molecules and/or other impurities. PCBM is a particularly relevant example because it is one of the most popular choices as the electron acceptor in organic solar cells adopting a type-II heterojunction design. Such an architecture is necessary to favour exciton splitting against a substantial exciton binding energy (0.2-1 eV or so)[24], in either bilayer[71] or bulk heterojunction (BHJ) organic solar cells[5,

[72]. In general, it is thus crucial to understand the physics of charge transport in PCBM in order to optimise this type of solar cells. Despite the large number of papers investigating the morphological and electronic properties of PCBM in solid blends with electron-donor materials[73-81], a clear understanding of its aggregation and intermolecular behaviour in such a complex system is yet to emerge. Preparation and characterisation of solvent-free single crystals have never previously been reported, although the crystalline structure of solvent-free PCBM has been resolved by means of powder diffraction, and published during the final stages of preparation and submission of this work[82]. Previously, Rispens et al. have proved that the solvent choice plays a critical role in the PCBM crystallization behaviour[83]. In particular, when drop-cast from ortho-dichlorobenzene (ODCB) PCBM was found to form red-brown platelet-shaped crystals with a monoclinic unit cell (a = 13.76, b = 16.63, c = 19.08 Å, and β = 105.3°), whereas casting from chlorobenzene (CB) leads to the formation of reddish triangle-shaped crystals with a triclinic unit cell (a = 13.83, b = 15.29, c = 19.25 Å , α = 80.3, β= 78.6, and γ = 80.41°). However, regardless of the solvent choice, these authors have noticed solvent inclusion inside the crystals. Furthermore, the substrate nature seems to affect the crystallization pathways undertaken by PCBM. In this context, Dabirian et al. prepared crystals via dip-coating deposition on three different substrates, observing the formation of crystals with different shapes, namely, hexagonal crystals on silanized SiO_x, amorphous aggregates on graphite and snowflake-like crystals on Au[84]. More recently Zheng and Han have prepared hexagonal crystals incorporating solvent molecules via liquid – liquid interfacial precipitation[85]. In addition to experimental investigations, various groups have carried out modelling studies to gain insight into the charge transport features and the structure–property relationship in PCBM[86, 87], C60[88] and related fullerene derivatives[89]. For this purpose, a reliable and well-defined structure of solvent-free PCBM is required.

3.1.1 Experimental details

Crystal growth and x-ray characterisation: PCBM was purchased from Aldrich (purity >99%) and used without further purification. The PCBM solution with a concentration of 20 mg ml^{-1} was obtained by dissolving an appropriate amount of PCBM in chlorobenzene (CB) at room temperature.

To ensure the complete dissolution of PCBM, the solution was kept stirring overnight at room temperature (295– 298 K) in the dark. I obtained PCBM single crystals by placing a droplet (~100 mL) of the PCBM solution on 15 mm diameter fused silica glass disks at room temperature and allowing the solvent to evaporate. The samples were kept in a capped Petri dish during the deposition and dried under vacuum (~10^{-2} mbar) overnight to remove the residual solvent. The vacuum treatment was carried out at room temperature. All the preparation procedures were carried out in a nitrogen glove-box to prevent degradation of the material. XRD measurements were performed on beamline I24 at the Diamond Light Source. The experiment was carried out using an X-ray beam size of 10 μm × 10 μm with a wavelength of 0.62 Å . The sample was held at a temperature of 100 K to minimise the background. The data were processed using CrysAlis Pro[90], the structure was solved with SHELXS-9729 and refined by means of full-matrix least squares in SHELXL-97[91].

See http://www.rsc.org/suppdata/tc/c3/c3tc31075b/c3tc31075b.txt for the crystallographic information file (CIF).

Computation: Molecular dynamics (MD) simulations were carried out for a 3 × 3 × 3 supercell (108 PCBM molecules) using the experimental crystal structure as initial coordinates. Two simulations were run for 100 and 300 K applying periodic boundary conditions. The systems were equilibrated in the NPT ensemble at 1 bar for about 4–11 ns using a Langevin piston with anisotropic pressure rescaling. Thereafter, simulations were carried out in the NVT ensemble at the respective equilibrium densities. Radial distributions and coordination numbers were averaged over 1000 frames taken from a 10 ns MD trajectory in the NVT ensemble. Parameters for bonded and non-bonded interactions were chosen as in ref.[87] i.e. OPLS parameter from ref.[92] with C60 bond lengths taken from ref.[93]. The only exception is the Lennard-Jones distance parameter for the carbon atoms of the C60 cages, which we increased to $\sigma = 3.832$ Å from 3.550 Å in the OPLS force field. The value was adjusted so as to reproduce the experimental density of fcc-C60 at room temperature[94]. The integration time step for the MD simulation was 1 fs. The MD simulations were carried out with the NAMD package[95].

3.1.2 Results and Discussion

Fig. 3.1 presents the optical microscopy images of the PCBM crystals produced via slow evaporation of the solvent. The best quality crystals were obtained by drop-casting a 20 mg ml^{-1} CB solution on fused silica glass. To obtain a solvent saturated atmosphere and slow down the solvent evaporation dynamics, the samples were placed in a capped Petri dish and kept overnight. Such a deposition technique, with a reduced solvent evaporation rate, enabled the formation of large PCBM crystalline aggregates with a lateral size of up to 500 μm. The preparation procedure involved the optimization of several parameters including solvent, PCBM concentration and substrate.

The images display the presence of high-quality, rhomboidal- shaped crystals, with sizes ranging from ~10 μm to 260 μm. In particular, Fig. 3.1a shows a single PCBM crystal (with a top surface ~260 × 30 μm^2). Some crystals were also found to stack on top of one another (Fig. 3.1b) or to merge with neighbouring crystals to form round-shaped multicrystalline aggregates. The polarised optical microscopy images (3.1 c-d) confirm the high quality of the crystals in terms of lateral homogeneity. This rectangular prism crystal habit for PCBM seems to be unprecedented, as Rispens[83] and Dabirian[84] have found different shapes for PCBM single crystals. This might be related to the different substrate used in our experiment and, hence, confirms the important role played by the substrate nature in affecting the PCBM crystallization behaviour.

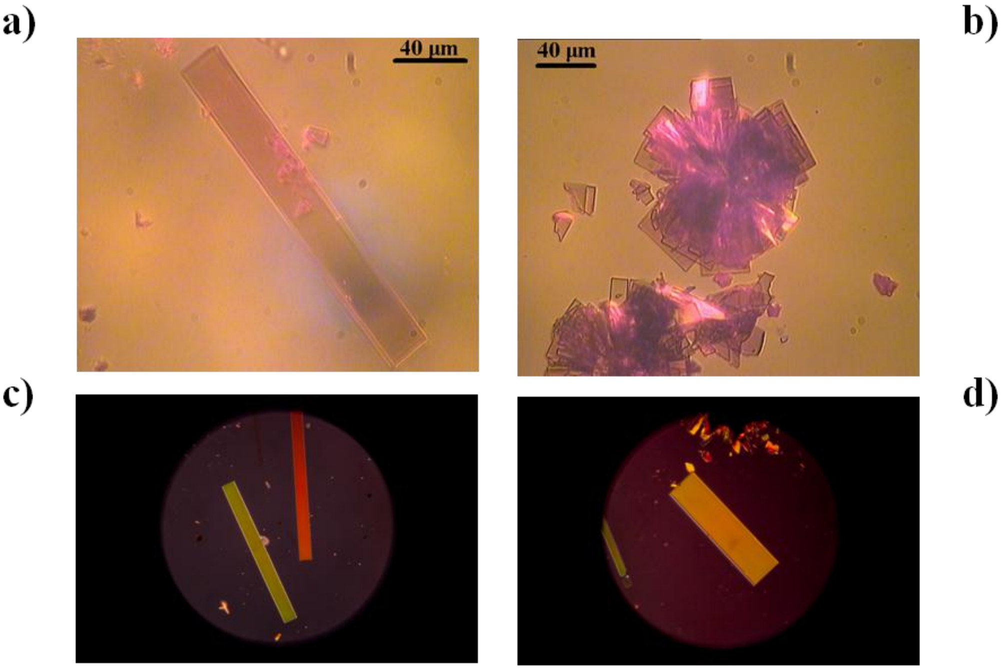

Figure 3.1: a) Optical microscopy images of PCBM single crystal and b) crystalline aggregates; c-d) Polarised optical microscopy images (50x magnification, 360 µm x 360 µm). Reproduced with the permission of the Royal Society of Chemistry.

The XRD micro-focus characterization revealed that PCBM assembles into a monoclinic unit cell containing four PCBM molecules (Table 3.1 and Fig. 3.2a and b). Remarkably, this structure does not show any solvent inclusion, in contrast to what was found by Rispens[83] and Zheng[85]. This is corroborated by the considerably smaller unit cell volume reported here as compared to that reported by Rispens (3708.70 vs. 3984.9 Å^3 for the triclinic and 4210.8 Å^3 for the monoclinic respectively, although this may partly be due to contraction of the crystals at 100 K, the measurement temperature). In addition, a van der Waals sphere representation obtained from the crystallographic information file (Fig. 3.2b) indicates clearly that there is not enough space to accommodate a solvent molecule inside the unit cell. Good agreement between the calculated crystallographic model and the experimental XRD data is demonstrated by the relatively low value of the *R*-factor (5.12%).

Table 3.1: : XRD data collected at the microfocus beamline alongside with the MD simulation data.

Empirical Formula	Crystal System	Space Group	Unit Cell Dimension	Volume	*Z*	Final Indices R
$C_{72}H_{14}O_2$	*Monoclinic*	*P2(1)/n*	Experimental, 100 K	*3708.70* $Å^3$	*4*	*R1= 0.0512*
			a= 13.47 Å α= 90°			*wR2= 0.1503*
			b=15.1 Å			
			β=106.90°			
			c= 19.01 Å γ= 90°			
			MD, 100 K	*3660.35*$Å^3$		
			a=13.25 α= 90°			
			b=14.77 β=106.23			
			c=19.48 γ=90°			
				*3709.28*$Å^3$		
			MD, 300K			
			a=13.29 α= 90°			
			b=14.93 β=106.33			
			c=19.48 γ=90°			

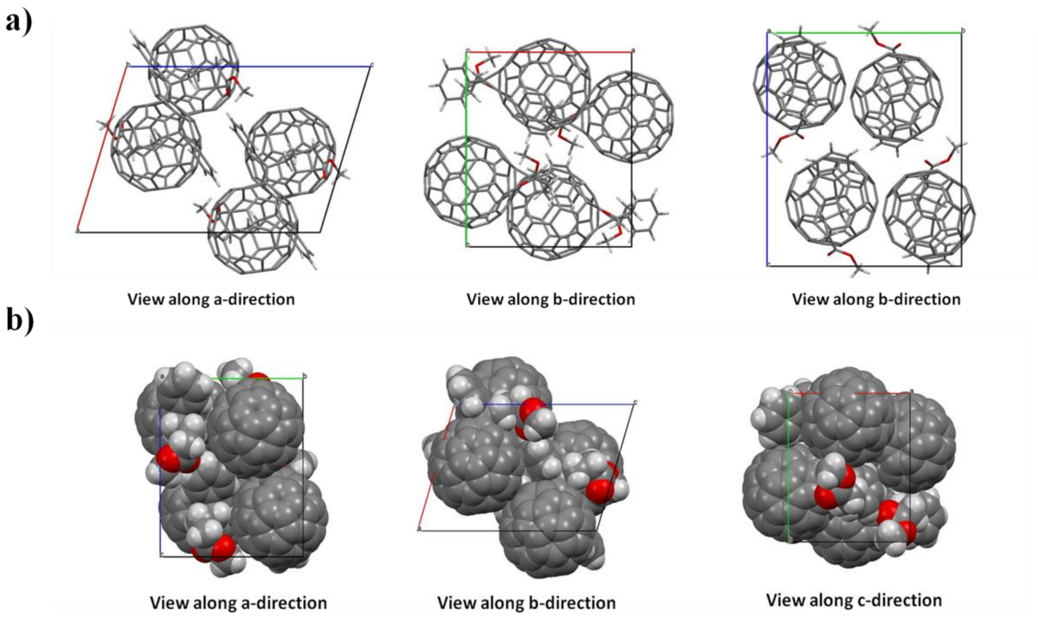

Figure 3.2: a) Monoclinic crystal packing of PCBM along a, b and c direction and b)Van der Waal sphere representation as obtained from the crystallographic information file (CIF). We thank Dr. A. Warren and Dr. G. Evans for performing the XRD characterisation and solving the crystalline structure. Reproduced with the permission of the Royal Society of Chemistry.

Classical molecular dynamics simulations of the solvent-free monoclinic PCBM crystal have been carried out for the temperature at which the X-ray structure was solved (100 K) and for room temperature (300 K), see the experimental details section for simulation details. The unit cell parameters obtained are summarized in Table 3.1. We find that the molecular model predicts the equilibrium density at 1 bar and 100 K reasonably well, overestimating the experimental value by only 1.3%. From the finite difference of the simulated volumes at 100 and 300 K, we estimate a thermal expansion coefficient of 6.7 × 10^{-5} K^{-1}, which is similar to the experimental value for C60, 6.2 × 10^{-5} K^{-1}[94]. The thermal fluctuations of the fullerene molecules are characterised in more detail by computing the centre-to-centre radial distribution functions of the C60 cages, shown in Fig. 3.3. The first peak is centred at 10.05 × 0.10 Å (100 K) and ranges from 9.55 to 10.55 Å, matching closely the shortest distances in the crystal structure (9.56 –10.85 Å, indicated by dashed spikes). The second peak exhibits a shoulder at 12.75 Å and a maximum at 13.25 Å matching again closely the discrete distances in the crystal structure. When the temperature is increased to 300 K the position of the first maximum remains virtually unchanged, and the shoulder at larger distances merges into a single broad peak centred at 12.95 Å. Thus, at room temperature the average nearest neighbour distance in monoclinic PCBM, 10.05 Å, is within statistical errors identical to the distance in fcc-C60 (10.02 Å using a lattice constant of 14.17 Å at 300 K[94]).

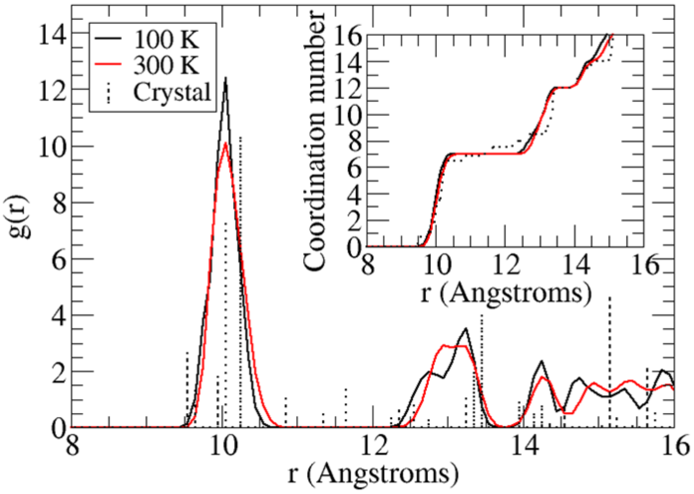

Figure 3.3: Radial distribution function of monoclinic PCBM as obtained from classical molecular dynamics simulation at 100 and 300 K. The spectrum of discrete distances in the X-ray structure are shown as dashed spikes. The distance r is the separation between the centres of mass of the C60 cages of PCBM. Coordination numbers are shown in the inset. We thank Prof. J. Blumberger and Dr. J. Spencer for performing the molecular dynamics simulations. Reproduced with the permission of the Royal Society of Chemistry.

Coordination numbers (CN) were obtained by spherical integration of the radial distributions, shown as insets in Fig. 3.3. Integration up to the first minimum at 11.0 Å gives a CN of 7.0 and further integration up to the second minimum at 13.8 Å gives a CN of 12.0. As can be seen, the CNs are rather insensitive to temperature in the range of 100–300 K. We note that the nearest neighbour CN (7.0) is higher than previously reported values for monoclinic PCBM which contained solvent impurities (PCBM: ODCB = 1: 1, CN= 6), but similar to the one reported for triclinic PCBM, where the PCBM to solvent ratio was higher (PCBM: CB = 2: 1, CN= 7)[83, 96].

3.1.3 Conclusions

I have reported the preparation and micro-focused XRD structural characterisation of large and high-quality crystals of PCBM. These provide a much needed experimental validation for computational models that build on such structural information for analysis and prediction of photophysical and charge transport properties in this class of materials. While in the final stages of preparation of our manuscript about these results[64], I became aware of similar results obtained by Casalegno and collaborators[82], who also obtained solvent-free crystalline structure but from powder diffraction experiments. Such a concomitant and independent finding that it is indeed possible to prepare solvent-free crystals disproves the long-held and discouraging belief that it is impossible to obtain solvent-free crystals of PCBM. In turn, it fully validates the selection of this material as both an experimental and computational model for charge transport and photophysical studies. The good agreement between experimental and computed structures, as evidenced by radial distributions and thermal expansion coefficient, suggests that the present atomistic model is especially well-suited for future investigations of electron transport in this important material.

3.2 Traceable atomic force microscopy of PCBM single crystals

In this section, I report about high-resolution, traceable atomic force microscopy measurements of PCBM solvent crystals. The morphological features of such crystals are extremely important for understanding their fundamental properties and applicative potential. For instance, lateral and vertical homogeneity are strict requirements for investigating the intrinsic charge transport features in organic crystals, in which the charge transport mechanism is likely to be non-activated (band-like)[97] as it happens in inorganic semiconductors. Although we observed that the vast majority of the crystals are flat, an isolated, non-flat crystal provides insights into the growth mechanism and allows identification of “molecular terraces” whose height corresponds to one of the lattice constants of the single PCBM crystal (1.4 nm) as measured with X-ray diffraction.

3.2.1 Experimental details

Metrological AFM measurements: A basic atomic force microscope (AFM) consists of a cantilever, with a sharp tip at its end, raster-scanned on the surface under test. Recalling the well-known working principle of an AFM, the presence of features on the surface induces bending in the cantilever or a variation of its oscillation amplitude if the AFM is working in contact or non-contact mode, respectively, and such changes can be related to the height of surface features. By operating the AFM in closed-loop the bending of the cantilever or the variation of its oscillation amplitude is compensated by moving the entire cantilever vertically using a piezoelectric transducer (PZT). On many commercial systems the vertical displacement, and therefore the surface topography, is obtained by converting the voltage applied to the PZT into displacement. Considering the non-linearity, drift and hysteresis inherent to PZTs, the voltage conversion is one of the major causes of inaccuracy and lack of traceability. To circumvent such a problem we use an AFM that has integrated optical interferometry for the measurement of the vertical motion of the PZT tube to compensate for tip bending[98]. Lateral motion is achieved with a high precision dual axis translation stage. Optical interferometry is the primary route to traceability for dimensional metrology, realised in this case, by the wavelength of frequency-stabilized He-Ne lasers[99, 100].

Importantly, use of an optical interferometer decouples the measurement of the Z displacement from the voltage (VSL) applied to the PZT by the servo loop. This therefore prevents errors introduced by associating the VSL to a z displacement when the servo loop compensates for drift or non-linearity of the PZT. The optical interferometer used, the National Physical Laboratory

(NPL) Plane Mirror Differential Optical Interferometer (PMDOI), is a homodyne differential interferometer, fibre-fed with a He-Ne frequency stabilized laser with wavelength of 632.8 nm. The PMDOI traceably measures the relative displacement between the tip and the sample by using the interference of two optical paths. These are defined by beams reflected twice on two parallel mirrors. One mirror is rigidly connected to the PZT tube that moves the cantilever, and the other forms the sample holder. Since the beams in each path are reflected twice on the relevant mirror, the sensitivity of the interferometer is doubled, and each fringe corresponds to $\lambda/4$ or ~158 nm for the He-Ne laser used here.

Measurements of the surface topography were carried out using the AFM in closed-loop, non-contact mode in a temperature-controlled environment (20 °C ± 0.01 °C). As well as the PMDOI, the AFM (figure 3.4a) uses a fibre interferometer featuring a laser diode (λ = 785 nm) for detecting the deflection of the cantilever. This is in place of the more usual beam deflection system found in most AFMs. The total AFM noise along the z-axis has been measured to be < 0.2 nm. The AFM images were numerically corrected for tilt using the “mean plane subtraction” tool in Gwyddion (a freely available software for AFM data visualization and analysis), and the crystal step height was measured according to the international standard ISO 5436 (2000),taking several line profiles (> 10) perpendicular to the crystal’s long axis and averaging the results. The standard ISO 5436 (2000) defines the currently accepted most accurate way of extracting the step height. The method involves fitting the data taken on the substrate on either sides of the single step and on the step itself, and therefore allows any residual tilt of the sample to be removed from the measurement of the step height.

3.2.2 Results and Discussion

Figure 3.4b shows an example of AFM measurements of two PCBM crystals next to one another, on a fused silica substrate. The measured height averaged along the main axes of the crystal is 48.2 ± 0.9 nm and 109 ± 0.6 nm, respectively (uncertainties here and in the rest of the test are given at one sigma). Figure 3.b shows a roughness (“root mean square”, rms) of 0.9 nm and 1.0 nm on the lower and higher crystal surfaces, respectively, compared to a roughness of 2.7 nm on the glass substrate. A close-up of the substrate (figure 3.4d) also indicates the presence of a non-uniform, discontinuous, 5 nm-thick PCBM layer (reddish grains in Fig. 3.4d) on top of the remaining areas of substrate (black-colored regions in Fig. 3.4d). The roughness of such non-uniform PCBM layer is 2.9 nm, compared to the 1.4 nm roughness of the glass (slightly different in the close-up compared to the 2.7 nm found on a larger sample of the glass).

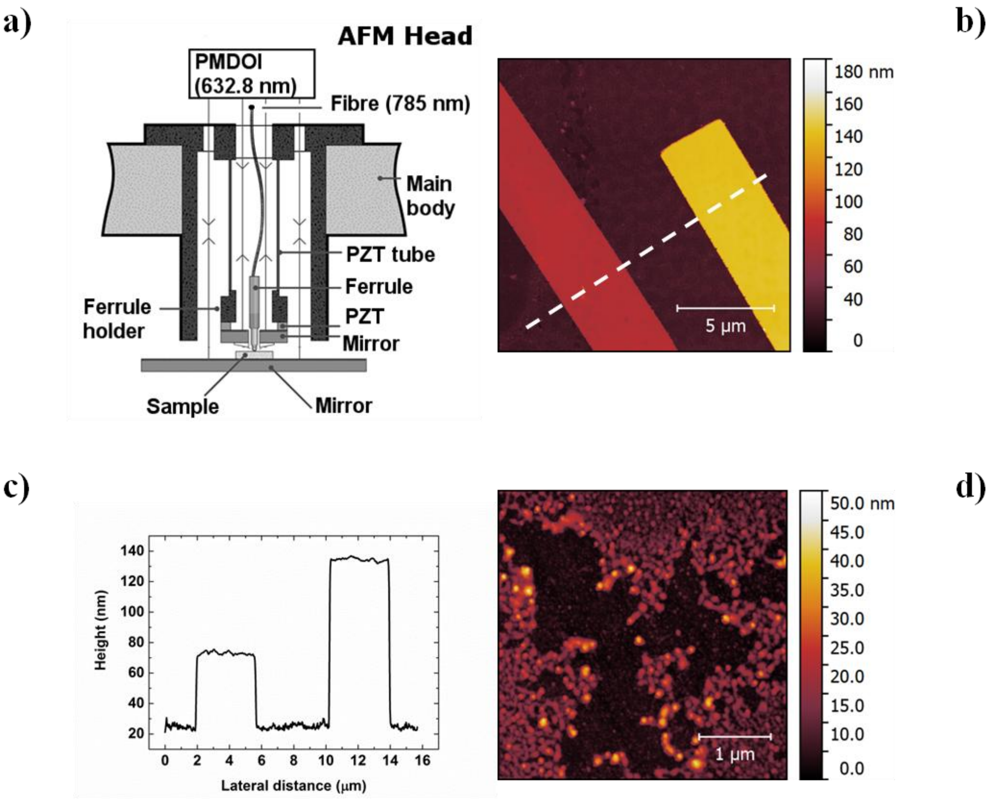

Figure 3.4: a) Schematic of the home-built AFM, including the interferometer beams for the detection of the vertical displacement; b) AFM image (512 x 512 pixels) and c) line profile of two PCMB crystals corresponding to the dashed line in Fig. 1b; d) AFM measurement (512 x 512 pixels) of the substrate, showing the glass substrate not completely covered by PCBM agglomerates.We thank Dr. G.M. Lazzerini for carrying out the metrological AFM measurements. Reproduced with the permission of the American Physical Society.

Interestingly, several PCBM crystals, measured across multiple samples, showed recurrent height values, multiples of either ~ 50 nm or ~ 70 nm (e.g. 49 ± 2 nm and 105 ± 3 nm or 72 ± 2 nm and 139 ± 3 nm). Identification of the factors limiting the growth of the crystals in the vertical direction to specific values are beyond the scope of this work, but, intriguingly, I also note the presence of some overlapping crystals. Figure 3.5a, for example, shows AFM measurements of two such crystals. Similar to the measurements in figure 3.4, the thickness of the crystal is 106 ± 1 nm and 103 ± 1 nm for both the crystal on the left and the crystal on the right of the image, respectively. The roughness on the non-overlapping areas is 0.6 nm (figure 3.5c-d), whereas the top crystal shows a damaged area with defects with depth up to 40 nm.

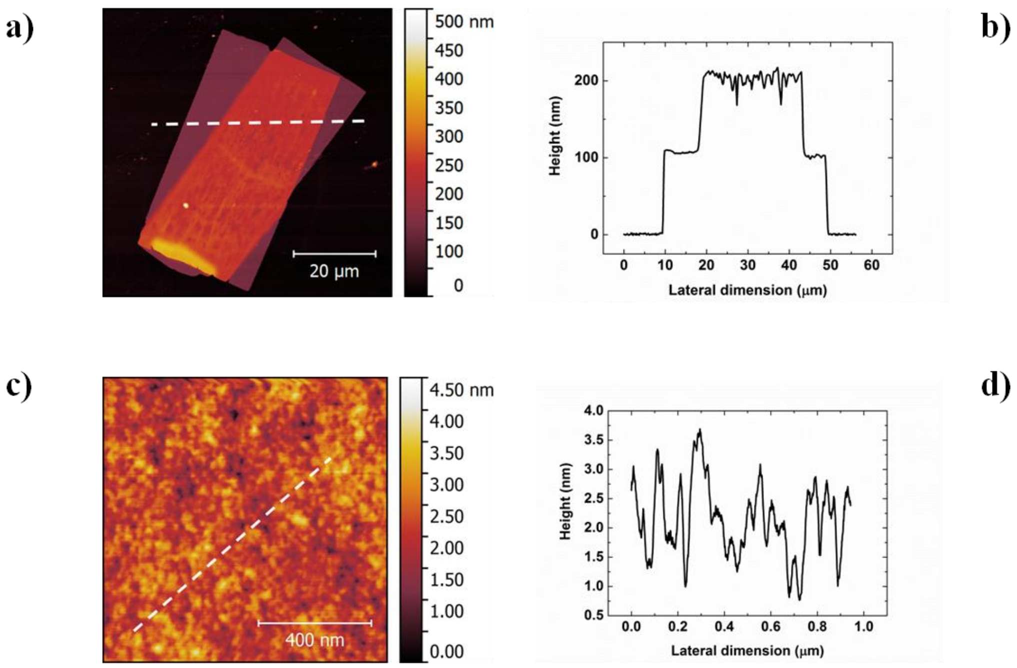

Figure 3.5: a) AFM image (512 x 512 pixels) and b) line profile of two PCBM crystals with the same height, laying on each other (corresponding to the dashed line in Fig. 3.5a; c) detailed AFM image (1024 x 1024 pixels) and d) line profile of the top surface of a PCBM crystal (corresponding to the dashed line in Fig. 3.5c). Reproduced with the permission of the Royal Society of Chemistry.

Figure 3.6a shows AFM measurements of the only crystal observed that was not flat. From the line profile along the main crystal axis (reported in Figure 3.6b), the crystal height increases from the edges (63 nm and 81 nm) up to 210 nm at the centre. In addition to recording a surface roughness of 0.6 nm, a “terrace discontinuity” on the crystal surface can be observed in Figure 3.6c and the value of the step is 1.4 ± 0.2 nm (Figure 3.6d). The inset of Figure 3.6c also shows the progression of a few terraces that eventually yield the monotonic increase of the surface morphology towards the centre of the long-axis of the crystal. Although the edges of such terraces are relatively rough, it is interesting that they have approximately the same extension in the direction of the crystal long-axis.

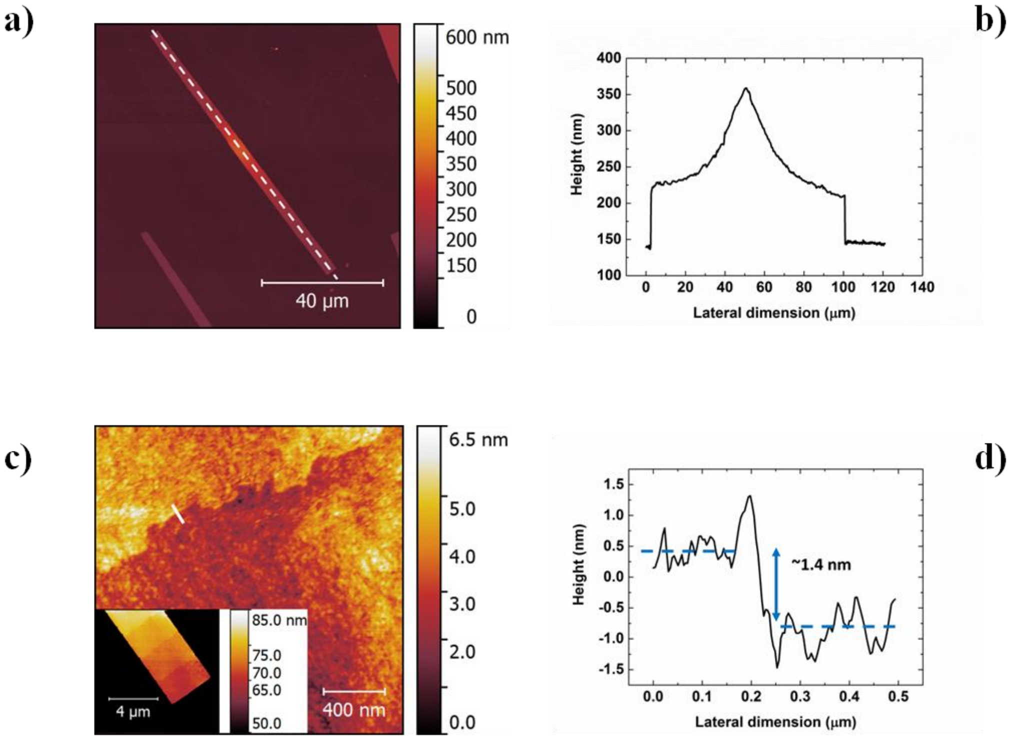

Figure 3.6: a) AFM image (1024 x 1024 pixels) and b) line profile of a PCBM crystal showing an increasing height from the edges of the crystal towards the centre (corresponding to the dashed line in Fig. 3.6a; c) detailed AFM image (512 x 512 pixels for main figure and 256 x 256 pixels for inset) and d) line profile of a 1.4 nm step-like defect on the PCBM crystal. Reproduced with the permission of the American Physical Society.

3.2.3 Discussion

I start my discussion from figure 3.4, and note that the crystals are generally rather uniform in thickness, along their length, with deviations of only 0.9 nm and 0.6 nm respectively for the ones in this figure, thereby confirming the visual impression of the relatively uniform nature of the crystal surfaces. This complements the information on the high quality of the PCBM crystals as obtained from XRD measurements, also demonstrating close packing of PCBM within the crystals bulk[64]. In addition to their uniformity, I observed that the crystals measured can be remarkably thin (thickness as low as 49 nm) compared to their lateral dimensions, which are of the order of few micrometres in width and tens of micrometres in length. As a consequence of the low thickness of the crystals and of their conformability, the measured roughness of the crystal's top surface is given by two components, one is the intrinsic crystal roughness and the other is associated to the conformation of the crystal to the substrate. This means, in turn, that the actual crystal roughness (Rq) can be even lower than the 0.6 nm or 0.9 nm measured. Such low roughness of the crystals, as measured with the metrological AFM, is also entirely consistent with the highly uniform polarisation colours observed in crossed-polarised optical microscopy (figure 3.7), which are correlated with the actual retardation, birefringence and thickness of the crystals. Only samples of highly uniform thickness and structural quality will produce such homogenous polarisation colours. Furthermore, even with a small misalignment with of the crystal with respect to the polariser and/or analyser, no complete extinction of the birefringence is observed, further underlying the excellent quality of the produced crystals, as clearly, perfect alignment is needed.

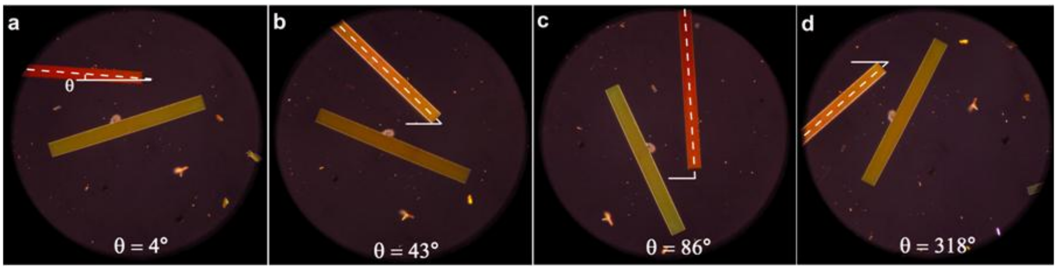

Figure 3.7: Cross-polarized optical light micrographs (360 μm x 360 μm) of PCBM crystals. Θ = angle between the polarizer (solid line) and major crystal axis orientation (dashed line); while the analyzer was positioned at 90° to the polarizer. Reproduced with the permission of the American Physical Society.

As noted above, from the zoomed-in image (Fig. 3.4d) we also observe the presence of a non-uniform, ~5 nm-thick layer of PCBM. We suggest that during the drying process, the PCBM aggregates on the glass substrate, probably clustering around defects in the underlying glass, and these then act as seeds for the formation of the crystals. The formation mechanism of the crystals is still under investigation, however my data suggest at least two possible mechanisms. First, I propose that the crystals can grow along directions pointing out of the surface plane, and essentially as part of complex 3D structures which I have previously reported in section 3.1[64], and that break (mostly at the base) when the solvent dries out or because of handling. Secondly, the crystals can also grow horizontally on the substrate on the PCBM layer, i.e. in a direction within the surface plane.

As an indication of the former growth mode, we note, in figure 3.5, two crystals lying on top of one another, and, more generally, the presence of crystals with recurrent height values (e.g. 49 ± 2 nm and 105 ± 3 nm or 72 ± 2 nm and 139 ± 3 nm). I suggest that for these crystals the thickness is a multiple of a given value (~50 nm or ~70 nm) as a consequence of the crystals growing as part of complex stacks, that subsequently collapsed during the drying process. Interestingly, there is a raised area in the bottom part of both crystals, which lends further support to our interpretation. The crystals appear to have grown simultaneously as they geminate from the area of the raised feature, and then the one lying on the top was later broken, collapsing on the other crystal, and leaving a “stump” (raised area). Figure 3.5a also shows the presence of several defects on the area where the crystals overlap, but not outside of it. I consider that such defects have been generated by the evaporation of the solvent trapped between the two crystals that must have found its way out by breaking the upper crystal and leaving it damaged, owing to the fast evaporation when exposed to vacuum. A different crystal formation mechanism is necessary to explain the unique shape reported in figure 3.6a. Here, I propose that the crystal was formed by the evaporation of a drop of solution that retracted towards the centre as the solvent evaporated, thus leading to a progressively higher PCBM concentration in the droplet which in turn deposited an increasingly larger amount of material when progressing towards the centre of the crystal. A corroborating indication of this is the presence of (already noted) several terraces perpendicular to the main crystal axis illustrated in the inset of figure 3c. Interestingly the step height is 1.4 nm ± 0.2 nm, which corresponds to the *a* lattice constant (1.347 nm), as measured via single-crystal XRD (see table 3.1). I therefore propose that the measured step is generated as the drop retracts, laying a new crystal plane on top of the existing ones.

3.2.4 Conclusions

In conclusion, I presented high resolution, traceable AFM measurement of high quality PCBM crystals. Although the crystals were fabricated through a solution processed procedure, and, as reported previously, they showed no solvent inclusion after vacuum exposure. The effect of the drying process has been considered for understanding the damage in limited areas of crystals and the formation of ~1.4 nm step terrace-like defects corresponding to the crystal lattice constant. Traceable AFM measurements confirmed that the roughness of the crystals' surfaces can be as low as 0.6 nm, which, together with their high quality bulk structure make them good candidates for further investigations of the basic physical properties of this important and intriguing material.

4 Fullerene Intercalation in a Poly (thiophene) derivative: A Neutron Reflectivity study

In this work, I use a pseudo-bilayer system made of poly(2,5-bis(3-hexadecylthiophen-2-yl)thieno[3,2-b]thiophene (PBTTT) and [6,6]-phenyl-C61-butyric acid methyl ester (PCBM), to acquire a more complete understanding of the diffusion and intercalation of the fullerene-derivative within the polymer layer. By combining AFM, x-ray diffraction and neutron reflectivity measurements, I observe that the degree of fullerene intercalation is heavily dependent on the degree of self-organisation of the polymer.

We thank Merck chemicals for providing us with the polymer, Dr. Maximilian W. Skoda and Dr. Robert Dalgliesh (ISIS - Neutron and Muon Source) for the assistance during the neutron reflectivity experiment and data analysis. The content of this chapter has been published as an open access paper in Nature Scientific Reports[101].

4.1 Introduction

As we have already anticipated in the introductory section, one of the most important advantages of organic semiconductors over their inorganic counterparts lies in the possibility of tailoring their physical and chemical properties by exploiting the power of intermolecular interactions. However, to take full advantage of this and hence optimise the performance of related opto-electronics devices, such as organic photovoltaic diodes (PVDs), thin film transistors (TFTs) and light-emitting diodes (LEDs), it is important to gain a detailed understanding on the way these carbon-based materials interact and arrange at the nanoscale[102, 103]. For instance, given the localised nature of charge carriers and excitations in organic semiconductors, exciton diffusion and splitting, charge transport and recombination in polymer-fullerene bulk heterojunction (BHJ) solar cells are strongly dependent on the nano- and meso-scale structure[104] and dynamics[12] of the interpenetrated network formed by the two semiconductors.

More specifically, in recent years it has been proved that polymer: fullerene solid blends are complex systems, in which both pure polymer and fullerene crystalline phases[64, 83] and amorphous intermixed phases coexist[11]. Interestingly, McGehee and collaborators have shown that fullerene derivatives can intercalate between the side-chains of a variety of polymers when there is enough space between the polymer side-chains[105] and the fullerene derivative is sufficiently small to fit between them[106]. In the case of semicrystalline polymers, it has been noted that fullerene can intercalate into the polymer crystalline phase forming stable bimolecular polymer-fullerene crystals[107-109]. The formation of such a mixed and well-ordered phase plays a central role in determining the optimum polymer : fullerene ratio in BHJ solar cells for efficient excitons splitting and charges generation, as also it has been found by molecular simulations[110]. Due to fullerene intercalation prevailing over phase separation in these systems, a pure electron-transporting phase is only formed when the fullerene loading exceeds the quantity needed for full intercalation.

Here, I show that the degree of intercalation of the fullerene derivative PCBM in the semicrystalline polymer poly PBTTT, depends significantly on the degree of self-organisation of the polymer, which in turn is controlled by the film solidification rate during processing. The temperature-dependent solubility of PBTTT[41, 111], insoluble at room temperature but highly soluble in hot chlorinated solvents (above 70 °C), allowed us make bilayers of these components by using a sequential-processing techniques[71, 112, 113]. Thus, I was able to prepare first the polymer layer from a hot solution, and then I overlaid a fullerene layer from the same solvent at room temperature, without dissolving the underlying polymer layer. I cast the polymer via three different deposition techniques to explore different solvent evaporation rates: spin-coating, slow-drying and drop-casting. The resulting films exhibited different morphologies and structural features, with PBTTT drop-cast exhibiting the highest crystalline order. By employing morphological and structural characterization techniques such as AFM, XRD and investigating the out-of-plane segregation of the two components by means of neutron reflectivity (NR), I observe that the rate of fullerene intercalation and formation of bimolecular crystals can be decreased substantially by increasing the crystallinity of the pre-deposited PBTTT films. This eventually leads to large differences in terms of electrical features, as revealed by the characterisation of photovoltaic diodes incorporating these different films as active material.

4.2 Experimental Details

Solar cells fabrication: C16-PBTTT (Merck) and PC61BM (Aldrich) were used without further purification. PBTTT/PCBM solar cells were prepared by depositing the active layer on indium tin oxide (ITO) pre-patterned glass substrates. The ITO substrates were sonicated in acetone and isopropyl alcohol for 10 minutes, dried in a flow of dry nitrogen and then placed in an oxygen-plasma for a 10 min treatment[114, 115]. Oxygen plasma has been shown to increase work function, as well as surface polarity and energy[116], and thereby help adhesion of subsequent layers to be deposited on top. A 30 nm thick hole-injection layer of poly (3, 4-ethylenedioxthiophene): poly (styrene sulfonate)(PEDOT-PSS) was spin-coated from aqueous solution and baked at 150 °C for 10 min, to increase work function and facilitate hole-extraction[117]. The active layer was obtained by first depositing the polymer from hot ODCB 20 mg/ml solution (70 °C) either via spin-coating, slow-drying or drop-casting, followed by a spin-cast deposition of PCBM (20 mg/ml) from the same solvent but at room temperature. For PBTTT spin-cast films, the warm solution was deposited onto the substrate and spun for 60 seconds at 4000 rpm. For slow-dried films, PBTTT was firstly spun for 5 seconds at 4000 rpm and then put it in a Petri dish to complete the film growth. The drop-cast films were obtained by depositing a droplet of solution (0.1 mg/mL in DCB) onto the substrate and letting the solvent dry naturally. To prevent formation of a defect-rich interface due to the quick crystallization of the solution upon contacting the cooler substrate, the substrates were warmed to 70 °C before deposition. A PCBM layer was then spun on top of those films (20 mg/mL DCB, 800 rpm for 60 seconds), yielding thicknesses of ~80 nm for all the samples, as measured by profilometry. Although a perfect bilayer may not be formed due to some diffusion and intercalation of PCBM into PBTTT, we refer to these as (nominally) “bilayer samples” for brevity. Finally, the Al cathode was thermally evaporated on the active layer in a high vacuum chamber (~2.5 x 10^{-6} mbar). All devices were annealed by placing them on a hot plate at 185 °C for 10 minutes in a nitrogen glove box. The photovoltaic efficiency was measured with a Sun 3000 solar simulator (110 × 110 mm^2 area), equipped with a Xenon lamp and an air mass (AM) 1.5 G filter (Abet technologies class AAA).

XRD and AFM: XRD measurements were performed with a Rigaku SmartLab diffractometer (Rigaku, Tokyo, Japan) at the ISIS Neutron and Muon Facility, Rutherford Appleton Laboratory, UK, by using a Kα wavelength emitted by a Cu anode (0.154 nm) and a Cross Beam Optics (CBO). To avoid beam defocusing, the measurements were carried out in parallel beam mode. All XRD diffraction patterns were collected using a symmetrical out-of-plane θ/2θ configuration. AFM images were recorded with a Veeco Dimension in tapping mode, using NSC35/AIBS ultra sharp cantilevers (MikroMasch Europe).

Neutron reflectivity: Neutron reflectivity measurements were carried out at the Offspec neutron reflectometer also at ISIS, using a specular scattering geometry[118]. The Offspec reflectometer used incidents wavelengths of neutrons from 1.5 to 14.5 Å and a time-of-flight detection system. Three incident angles (0.35°, 1° and 2.3°) were used to obtain the reflectivity as a function of the momentum transfer perpendicular to the sample plane, $\mathbf{q}_z=(4\pi \sin(\theta))\lambda$ The scattering length densities (SLD) for PBTTT and PCBM are 5.59×10^{-7} $Å^{-2}$ and 3.76×10^{-6} $Å^{-2}$, respectively. For NR measurements, the polymer/fullerene layers were cast onto Si/SiO_2 wafers with a diameter of 50 mm, following the same deposition procedure used for OPVs fabrication. However, given the larger substrate size in comparison with OPVs samples I had to lower the deposition speed to 2000 rpm for "PBTTT spin-cast" and "PBTTT slow-dried" samples. This led to slightly thicker layers for those two samples (~120 nm for both bilayer "PBTTT spin-cast" and "PBTTT slow-dried"), whereas the measured thickness of the "PBTTT drop-cast" bilayer was comparable with the solar cell one (~80 nm). Eventually, the samples were thermally annealed at 185 °C for 10 minutes in vacuum. The NR data were analysed using the software RasCal (version 1.1.3, A. Hughes, ISIS Spallation Neutron Source) which employs an optical matrix formalism based on the Abeles method[54]. In this approach, the interface is divided into a series of slabs, each of which is characterized by its SLD, thickness, and roughness. The interfacial roughness between adjacent layers was included in the model as an error function of standard deviation (Nevot-Croce approach)[119]. Statistical analysis showed that for the NR fits, a model with four layers was necessary to describe the data (SiO_x and three layers for the "bilayer" region). The interfacial roughness between these layers was significant compared to their thickness, indicating a relatively gradual change in the composition of the layer.

4.3 Results and discussion

Figure 4.1a shows the AFM height images alongside their phase pictures for pure PBTTT cast via spin-casting, slow-drying and drop-casting depositions.

I can observe clear morphological differences among the three films, which suggest that the polymer degree of self-organisation can be varied by controlling the film solidification time. In particular, the solvent evaporation time was evaluated by visual inspection of the change of the film colour (light to dark purple) when it passes from the liquid to the solid phase. For spin-cast films, such change in colour occurred in ~10 seconds, although we spun it for 60 seconds to dry further the film. For slow-drying deposition, I spun-cast the film for 5 seconds and we placed the still wet film in a closed Petri dish to complete the solidification process, which occurred in ~2 minutes. For drop-cast films, I placed a droplet of the PBTTT solution onto the substrate and waited ~12 hrs until the film solidified. We can observe that, whereas the spin-cast film looks relatively unstructured, the slow-dried one show fibril-like aggregates that are more distinctively visible in the phase images. The height and relative amount of such nanofibrillar features increased further when the film was deposited via drop-casting. Such an increased ordering when increasing the film solidification time is provided indirectly by the root mean square (RMS) roughness of the films[120], which increases in the order spin-cast → slow-dried → drop-cast (2.42, 5.20 and 5.59 nm, respectively).

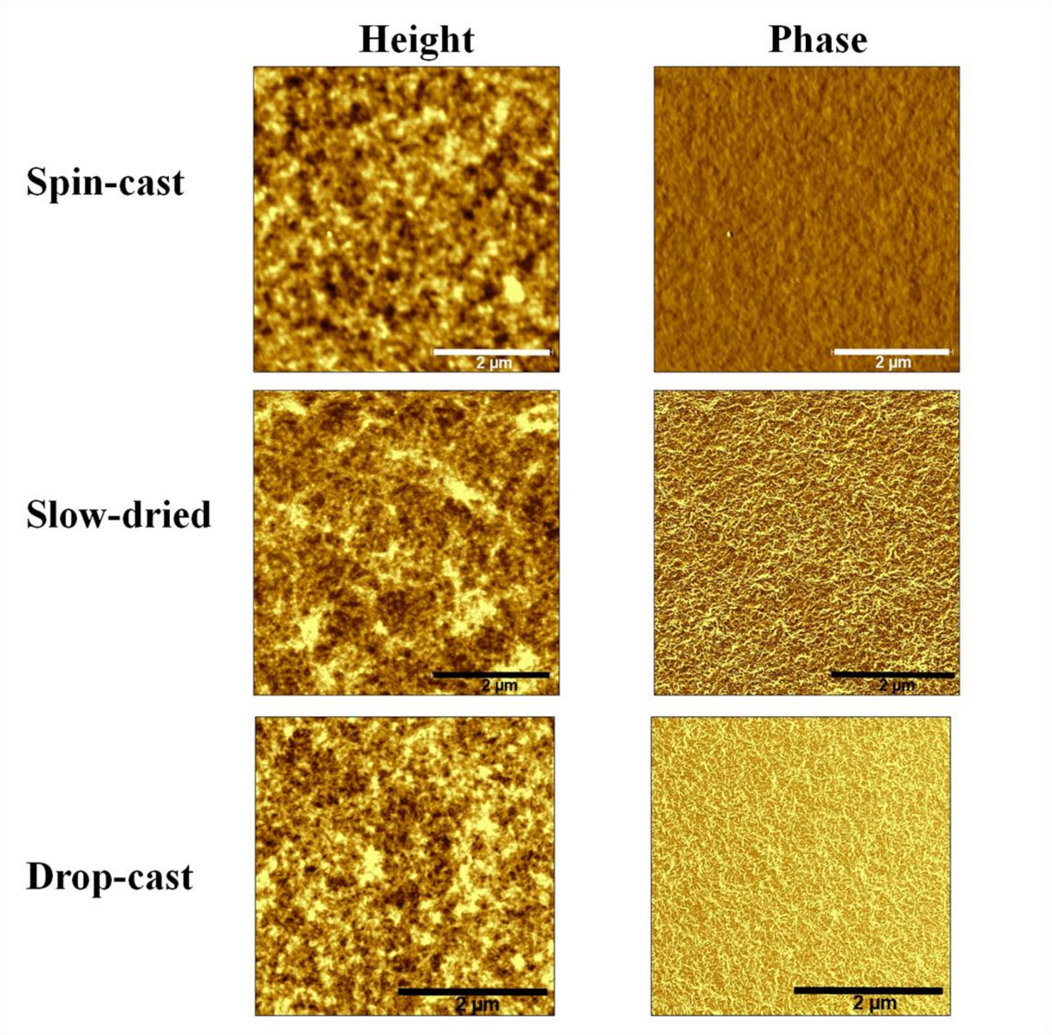

Figure 4.1: AFM height and phase images of PBTTT spin cast, slow-dried and drop-cast height. The height and phase scales are: 0-15 nm and 0-15 deg. for PBTTT spin-cast, 0-30 nm and 0-20 deg. for slow-dried and 0-30 nm and 0-20 deg. for drop-cast. The film thickness is ~60 nm (measured by profilometer). None of the pure PBTTT films was thermally annealed.

The x-ray diffraction pattern of the pure PBTTT films cast via spin-casting, slow-drying and drop-casting (figure 4.2a) indicates clearly that the degree of order increases with the film solidification time, as indicated by the increase of the peak intensity and decrease of the FWHM of the <100> lamellar peak, following the order spin-casting → slow-drying → drop-casting.

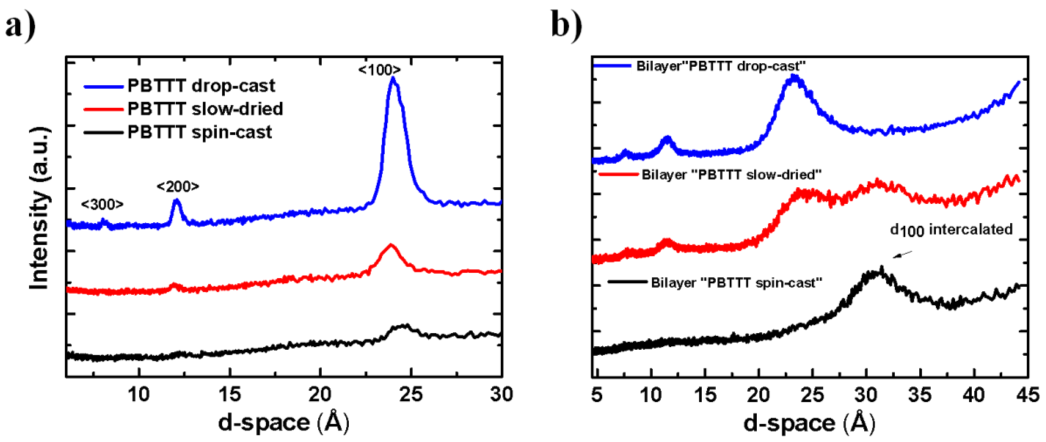

Figure 4.2: a) XRD pattern (out-of-plane) of PBTTT pure deposited via spin-casting, slow-drying and drop-casting. The <100> peak (at ~ 24 ° for all the films) and its higher orders refer to the lamellar stacking (see ref. 12). None of the pure PBTTT films was thermally annealed. b) XRD pattern (out-of-plane) of PBTTT/PCBM films obtained by sequentially depositing the PCBM on top of the three different polymer films (PBTTT spin-cast, slow-dried and drop cast). Although perfect bilayers are not formed due to PCBM diffusion and intercalation in the polymer layer, we refers to these samples as bilayer "PBTTT spin-cast", "PBTTT slow-dried" and "PBTTT drop-cast" for simplicity. Note that all the bilayers were annealed at 185 °C for 10 minutes.

Now I turn to the characterisation of the PBTTT - PCBM bilayers, obtained by depositing the PCBM layer on top of the three different PBTTT films (spin-cast, slow-dried and drop-cast). All the bilayers were thermally annealed at the polymer glass transition (185 °C) for 10 minutes. We refer to these samples as "PBTTT spin-cast", "PBTTT-slow-dried" and "PBTTT drop-cast" bilayers. The addition of PCBM causes a clear expansion of the PBTTT lamellar peak because of fullerene intercalation[107], and thus we can use XRD as a tool to determine the degree of PCBM intercalation and correlate this with the PBTTT morphology. The diffraction pattern in figure 2b shows that, whereas in the pure polymer the spacing for the lamellar peak is 24.0 ± 0.2 Å, in the "PBTTT spin-cast" the d-spacing has increased to 30.9 ± 0.1 Å, indicating that full PCBM intercalation occurs for this sample and bimolecular crystals are formed. On the other hand, for the "PBTTT drop-cast" bilayer, the plot shows the same pattern as for the pure polymer. Interestingly, for "PBTTT slow-dried" bilayer both the pure polymer peak and bimolecular crystalline peak coexist, suggesting that PCBM partially intercalates in between the polymer side-chains and full intercalation is not achieved. It is interesting to note that a similar trend in the XRD pattern can be observed when the degree of intercalation is controlled by varying the fullerene loading in PBTTT : PC71BM blends, with full intercalation occurring already with a 1:1 ratio, partial intercalation with a 4:1 ratio and no intercalation with lower PCBM loadings[107]. Although this corroborates my findings, it should be mentioned that in our case fullerene intercalation is intrinsically controlled by the degree of self-organisation of the polymer, and does not depend on the fullerene loading. In particular, it seems that when I favour the formation of a stable polymer crystalline phase, pre-PCBM loading, by employing a deposition techniques with slower solvent evaporation rates (i.e. slow-drying and drop-casting), the polymer does not allow the fullerene molecules to diffuse within the polymer layer and intercalate in between the side-chains. Therefore, by simply varying the film solidification time and hence the degree of polymer self-organisation, I can easily control the degree of fullerene intercalation.

Having established that fullerene intercalation can be tuned by controlling the polymer's degree of self-organisation, I now turn to specular NR investigation, which allows me to gain insight into the vertical composition of the layer. The scattering length density (SLD) contrast between the PBTTT and PCBM components is large, almost an order of magnitude (5.59×10^{-7} Å^{-2} and 3.76×10^{-6} Å^{-2}, respectively). In figure 4.3 the reflectivity curves and the relative SLD depth-profiles for the three different samples are presented. Note that in all the reflectivity profiles the Kiessig fringes, caused by the interference of waves reflected in multi-layered systems, are not clearly visible. In our samples, those fringes are likely being damped by the high roughness between the various interfaces in the multi-layer system. However, by taking advantage of the large difference between the SLD of PBTTT and PCBM, we were able to obtain information about the vertical composition using the calculated SLD for pure PBTTT and PCBM. In particular, the SLD profiles normal to the film were obtained by fitting the reflectivity curves using a model of slabs and were normalised to thickness.

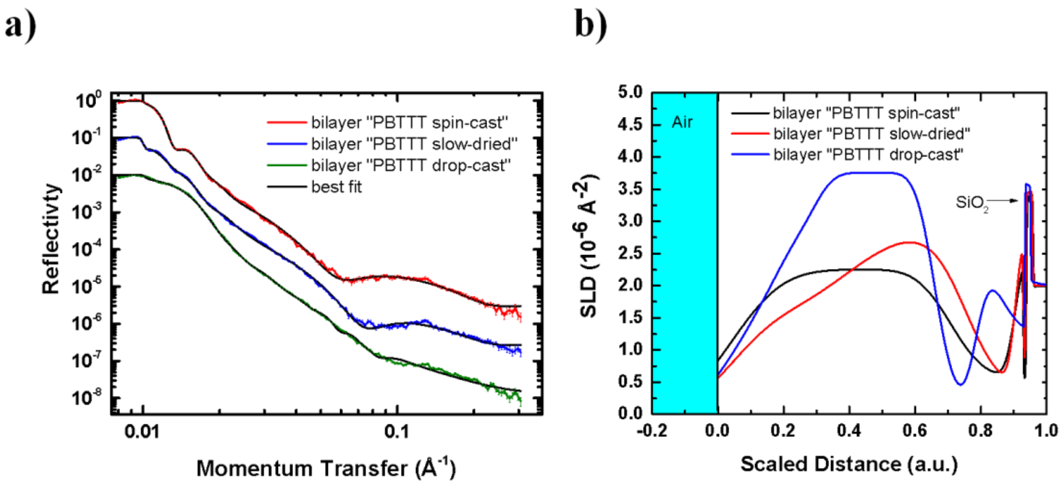

Figure 4.3: a) NR curves and b) SLD profile for "PBTTT spin -cast", "PBTTT slow -dried" and "PBTTT drop -cast" bilayers. Note that the x-axis was normalised to thickness, with a scale from 0 (air interface) to 1 (substrate interface). The total thicknesses of "PBTTT spin-cast" and "PBTTT slow-dried" bilayers are ~120 nm, and ~80 nm for "PBTTT drop-cast" bilayer. All samples were annealed at 185 °C for 10 minutes.

The SLD profiles reveal a complex vertical PBTTT-PCBM stratification that appears to be function of the different PCBM intercalation features in the bilayers. In general, we observe two PBTTT:PCBM mixing regions: a first region close to the air interface that is likely produced upon PCBM-PBTTT contact, and a deeper mixing region that is formed after further PCBM vertical diffusion towards the bulk of the layer. Note that PCBM diffusion and preferential segregation towards the substrate is favoured by its higher surface energy than poly (thiophene) derivatives[121, 122]. In this context, moving from the air interface (0) to the substrate interface (1) for bilayer "PBTTT spin-cast" we can observe: i) a BHJ-like region with a PBTTT : PCBM ratio of 1:1 (~80 nm); ii) a PBTTT enriched layer (~24 nm); two thin and relatively rough wetting layers close to the SiO_2 interface. In particular, the first wetting layer (3 nm) with a ~1:1 PBTTT:PCBM ratio can originate from the further diffusion and mixing of the non-intercalated PCBM with PBTTT segregated at the bottom of the layer, whereas the last wetting component (1 nm) consist of a pure PBTTT layer. It is worth noting that the formation of a PBTTT wetting layer a the substrate interface would be beneficial for the operation of solar cells, since this avoids the segregation of the electron-acceptor component at the anode, where it would hamper hole extraction.

On the other hand, for the "PBTTT drop-cast" bilayer PCBM the intercalation process does not seem to take place effectively, as we can observe a PCBM enriched top surface (~40 nm) and a PBTTT-rich region (15 nm). As the amount of non-intercalated PCBM is higher in this case, the further diffusion of PCBM towards the substrate leads to rougher and more PCBM-enriched wetting layers. Interestingly, the vertical structure of the bilayer "PBTTT slow-dried" is more complex as it can be considered as a "hybrid" between the two aforementioned samples, with i) a first PBTTT-PCBM 4:1 BHJ region (~40 nm), ii) a PCBM-rich region (~35 nm), iii) a PBTTT-rich region (~15 nm) and iv) two thin wetting layers whose PBCM enrichment is slightly higher than in bilayer "PBTTT spin-cast" but lower than in bilayer "PBTTT drop-cast". These features can be seen clearly in the simulated SLD profiles for which the interfacial layer roughness values have been set ten times lower than the experimental ones (figure 4.4). Note that the clear appearance of the Kiessig's fringes in the simulated NR profiles, confirm that the damping of those oscillations are in-fact mainly due to the high interfacial roughness in such pseudo-bilayer systems.

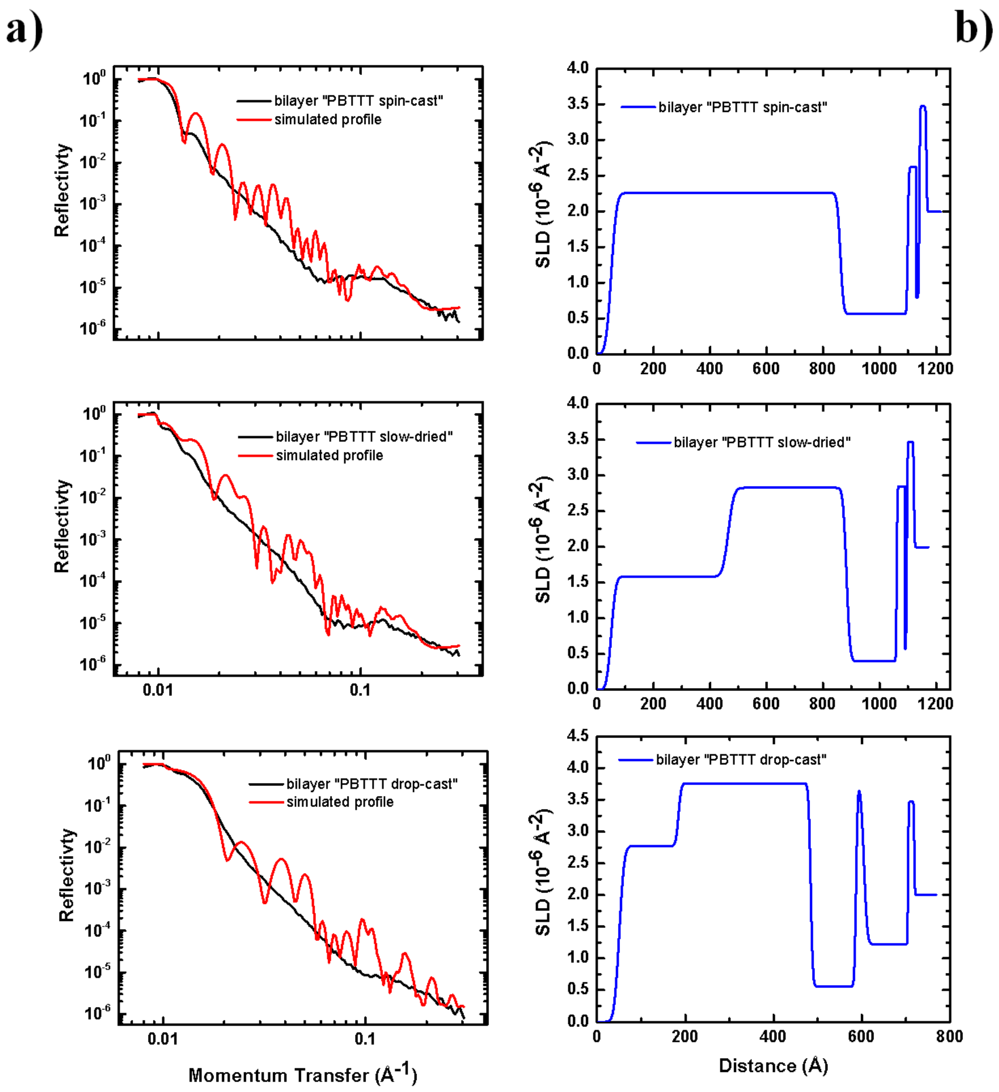

Figure 4.4: a) Simulated NR curves and b) SLD profiles for "PBTTT spin-cast", "PBTTT slow-dried" and "PBTTT drop-cast" bilayers, in which the interfacial layer roughness values are ten times lower that the experimental ones. The curves have been simulated using the software RasCal (freeware).

In any case, it is interesting to point out the NR results also agree with the XRD data, suggesting a strong dependence of the fullerene intercalation rate on the polymer degree of order. In addition, the calculated compositions of the top layers fit the results in the study by Mayer et al.[107] as a function of PCBM loading, which shows that partial intercalation occurs with a 4:1 polymer:fullerene ratio, whereas the fullerene fully intercalates when the ratio is 1:1.

I now discuss how this ordering relates to the electronic performance of the solar cells. Figure 4.5 shows the J-V characteristics for the three PBTTT-PCBM devices. I can observe that the performance of "PBTTT spin-cast" bilayer device approaches that of a PBTTT: PCBM BHJ with a ratio of 1:3 (efficiencies of 1.2% and 1.3%, respectively). This further confirms that if the polymer degree of self-organisation is low, PCBM can diffuse significantly inside the polymer layer and intercalate, leading to a BHJ-like structure. Interestingly, it can be also noted that, even though the polymer-fullerene ratio within the "PBTTT spin-cast" bilayer is 1:1 and hence well below the optimum ratio for PBTTT : PCBM[123, 124], the efficiency is still comparable for these two types of devices. The slight losses in current for the "PBTTT spin-cast" bilayer, which are likely due to the lower polymer-fullerene interfacial area and, thus, to a lower fraction of split excitons, might in fact be counterbalanced by the better vertical segregation of the two components in such pseudo-bilayers devices, in which the electron-donor material preferentially segregates at the anode, as revealed by NR measurements. On the other hand, if the polymer is already well structured, as in the case of "PBTTT slow-dried" and "PBTTT drop-cast", it does not allow fullerene molecules to intercalate and, therefore, charges cannot be efficiently extracted due to the low polymer-fullerene contact area. This results in poor efficiencies, with the drop-cast sample giving the worst performance. The poorer performances of these two samples and, in particular, of the bilayer "PBTTT drop-cast" device can be also related to the unfavorable vertical architecture in these samples, which show a stronger PCBM segregation at the substrate interface. This effect, in turn, would also explain the drop of V_{oc} observed for the "PBTTT drop-cast" device, as the presence of a fullerene-rich defective layer at the cathode interface would hamper the built-in of the driving voltage necessary for excitons splitting. It is important to note that the charge generation process in OPVs not only depends on the vertical phase separation and stratification, but also on the lateral morphology in the active layer. For instance, another synergic reason that causes a lower current in bilayer "PBTTT drop-cast" can also lie on the larger crystallites size in this sample, larger than the typical exciton diffusion length (10 nm)[15]. This in turn would lead to a smaller fraction of split excitons at the PBTTT-PCBM interface and a lower amount of free charges collected at the electrodes.

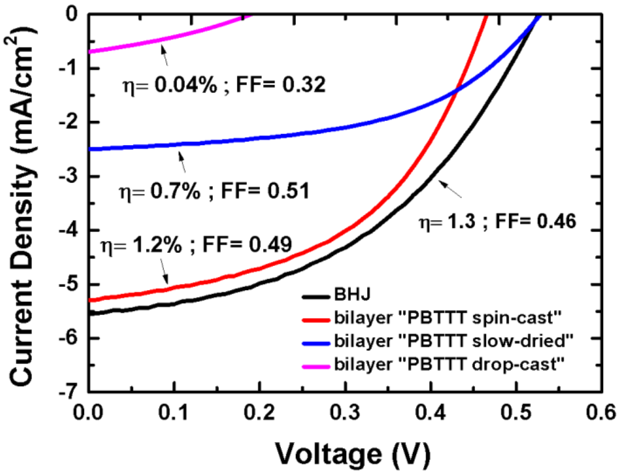

Figure 4.5: J-V characteristics for the PBTTT : PCBM pseudo bilayers. The BHJ (PBTTT/PCBM weight ratio 1:3) J-V characteristic is also presented for comparison.

4.4 Conclusions

In summary, I have shown that the degree of fullerene intercalation is not only a function of the fullerene size and the free volume available between the polymer side-chains, but also of the degree of self-organisation of the polymer prior to mixing with the PCBM. In particular, our findings suggest that if I assist the polymer in the development of a stable thermodynamic state by slowing down the solvent evaporation rate during the film solidification, the polymer does not permit the fullerene to intercalate and mix at the molecular scale. Although the degree of intercalation in PBTTT : PCBM scales with the solar cell performance, in not-intercalated systems the electron-donor/electron-acceptor interfacial area available for excitons splitting and charges generation is reduced significantly, intercalation may have various effects on different polymer-fullerene systems. Therefore, shedding light on the mechanism of intercalation can be paramount for the optimisation of polymer-fullerene solar cells and, more in general, for controlling the opto-electronic properties in a variety of organic-based devices.

5 Neutron Spectroscopy of Poly (thiophene): fullerene blends for Organic Photovoltaic

In this chapter, I present a detailed structural and dynamical characterisation of P3HT: PCBM blends, carried out by means of x-rays/neutron diffraction and quasi-elastic neutron scattering.

In the first section (5.1), I report data from x-rays and neutron scattering on the structure and dynamics of the blends cast from three different solvents characterised by different boiling points, namely chloroform (CF, boiling point Tb = 61.2 °C), chlorobenzene (CB, Tb = 131 °C) and ortho-dichlorobenzene (ODCB, Tb = 180.5 °C). We observe that solvent choice influences the degree of order and phase separation of the blends. From the dynamical point of view, *QENS* data suggest that blending frustrates the polymer side-chain motion. In section 5.2, I present a neutron polarisation analysis carried out on those blends, to separate unambiguously coherent from incoherent scattering contributions.

We thank Dr. John Ross Stewart (ISIS - Neutron and Muon Source) and Dr. Andrew Wildes (Institute Laue Langevin) for the valuable assistance during the neutron polarisation analysis experiment and data analysis. The content of this chapter is reproduced with the permission of Elsevier (see ref.[12] and ref[125].).

5.1 Structural and Dynamical Characterization of P3HT/PCBM Blends

As it has been described previously in section 2.2.2, in *QENS* we look at the scattering signal in the close proximity of the elastic line. For this, *QENS* is well suited to probe various dynamical processes in soft matter and, in particular, those slower dynamic features that are in between phonons/molecular vibrations and the elastic signal (see figure 2.9a), such as polymer side-chain rotations and slower segmental motions. Therefore, with this technique we can monitor the dynamics of multi-component systems such as polymer blends and nanocomposite systems, with the advantage of mapping their nanoscale spatial dependence as a function of the momentum transfer.

For instance, the benchmark blend for BHJ organic solar cells, which is based on regioregular P3HT as the electron donor and PCBM as the electron acceptor, can be seen as a polymer: nanocomposite system, which can encompass not only polymer confinement by the composite particles, but also from the crystalline/amorphous domains. In this context, as *QENS* is particularly sensitive to hydrogen atoms due to their large incoherent scattering cross section[10] and P3HT possesses thirteen hydrogen atoms on the side chain, such a technique can be used to highlight the contribution of the side chain and the effect of blending. For these reasons, in recent years *QENS* has started to be employed in the study of side-chain dynamics of pure poly(alkylthiophenes)[126] and in blends with carbon nanotubes[127] or fullerene derivatives[128].

In this work, I characterise for the first time the dynamical features of P3HT in the presence of the electron acceptor, PCBM. We first study the structure of the blends with x-ray and neutron diffraction, and then look at the dynamics using *QENS*. In particular, I look at the effect of solvent choice and annealing treatment on the structural/dynamics characteristics of the blend system. This provides further insight into the nanoscale rearrangements on the active layer and complements existing structural measurements[129].

5.1.1 Experimental details

Sample preparation: Regioregular P3HT (M_w = 10,000 - 40,000 g/mol) and PCBM were purchased from American Dye Source and used without further purification steps. Blends of 50 wt% P3HT-PCBM were prepared by dissolving the proper amount of material in chloroform (CF), chlorobenzene (CB) and ortho-dichlorobenzene (ODCB). The resulting solutions were drop-cast onto aluminium foil, yielding sample films of around 70 µm (as needed for the *QENS* neutron scattering experiments to achieve transmissions of ~ 90% and minimise multiple scattering effects). The samples were vacuum-dried overnight at room temperature (RT= 20-25 °C) to remove any residual solvent.

Differential Scanning Calorimetry (DSC): DSC measurements were performed on a Mettler Toledo DSC 1 calorimeter at a scan rate of 10 °C/min. Melting and crystallisation temperatures were recorded and percentage cristallinity calculated. In all the DSC traces no peaks related to solvent impurities evaporation were found, indicating that the drying procedure described above was enough to remove the trapped solvent inside the samples.

X-ray diffraction (XRD): XRD measurements were performed with a Rigaku SmartLab diffractometer (Rigaku, Tokyo, Japan) by using a Kα wavelength emitted by a Cu anode (0.154 nm) using a classic θ/2θ configuration. Measurements were done before and after annealing for all blends at 160 ° C.

Quasi-elastic neutron scattering: QENS measurements were carried out on the high-resolution backscattering spectrometer IRIS at ISIS[130]. The scattering signal is the sum of both coherent and incoherent contributions, however for our system the signal is dominated by the incoherent scattering of the hydrogenated side chains of P3HT (σ_{inc} P3HT= 75.5 %, σ_{coh} P3HT= 5.5 %, σ_{inc} PCBM= 14 %, σ_{coh} PCBM= 5 %). Therefore, any motion observed arises from the dynamics of the polymer side chain, to a good approximation. Both P3HT and PCBM have a measurable coherent contribution, which enables us to probe the Bragg peaks from the crystalline domains in the blend (by monitoring the elastic signal as a function of the scattering vector $\boldsymbol{Q}$).

The measurements were performed using the PG002 analyser that affords a resolution of 17.5 μeV, a dynamical range from -0.4 to 0.4 meV and a $\boldsymbol{Q}$-*range* from 0.42 to 1.85 Å^{-1}. For all samples, we performed an initial so-called elastic scan where the temperature is ramped from 40 K to 500 K at a heating rate of 1 K/min, whilst collecting neutron data. The temperature dependence of the elastic-scattering intensity was analysed using equation 5.1:

$$S(\boldsymbol{Q},T,\omega \approx 0) = \exp\left(-\frac{1}{3} < r^2 > (T)\boldsymbol{Q}^2\right), \tag{5.1}$$

where $\boldsymbol{Q}$ is the scattering wave vector and $< r^2 >(T)$ is the mean-square displacement (MSD) of the scattering centres at any given temperature. The decrease of the elastic intensity and the increase of the MSD with increasing temperature can be linked to a variety of atom displacement mechanisms (vibrations, rotations and translations), whose intensity increases with increasing temperature. To calculate the MSD, I plotted the natural log of the elastic-scattering intensity as a function of $\boldsymbol{Q}^2$ ($\boldsymbol{Q}$-range from 0.48 to 1.85 Å^{-1}) at each temperature and fitted with a linear function , obtaining the MSD of the hydrogen atoms. After having acquired the *QENS* signal, I converted the measured $S(Q, \omega)$ from the energy domain to time domain by applying a complex Fourier transform . The measured $\bar{\mathrm{I}}$ (Q, t) is the convolution of the true I (Q, t) and the resolution $R\ (Q,t)$:

$$\bar{\mathrm{I}}\ (\mathbf{Q},\mathrm{t}) = \mathrm{I}\ (\mathbf{Q},\mathrm{t}) \times \mathrm{R}(\mathbf{Q},\mathrm{t}). \tag{5.2}$$

The intermediate scattering function was fitted with the empirical Kolrausch-Williams-Watts (KWW) equation, or stretched exponential[56]:

$$\frac{S(\boldsymbol{Q},t)}{S(\boldsymbol{Q},0)} = A(\boldsymbol{Q},t)\exp\left[-\left(\frac{\tau}{\tau_{KWW}(\boldsymbol{Q},t)}\right)^{\beta(\boldsymbol{Q},t)}\right] + [1 - A(\mathbf{Q},\mathrm{t})], \tag{5.3}$$

where β is a shape parameter ($0 < \beta \leq 1$) measuring the deviation from a simple exponential decay, τ_{KWW} is the relaxation time. The parameter A is a temperature and $\boldsymbol{Q}^2$-dependent amplitude factor related to the elastic fraction and, thus, MSD, via equation 5.4 [131]:

$$A(\boldsymbol{Q}) = exp\left[-\frac{<r^2>\boldsymbol{Q}^2}{3}\right] \tag{5.4}$$

We also make used of the IRIS diffraction detectors bank, to probe some of the structural features in situ. They afford a resolution of which has a $\Delta d/d = 2.5 \times 10^{-3}$ and a d-range from 1 to 12 Å. Annular aluminium can was used to hold the samples for all *QENS* experiments. The data were corrected for detector efficiency using a vanadium standard.

5.1.2 Results and discussion

I carried out differential scanning calorimetry (DSC) to locate precisely the thermodynamic/kinetic transitions (i.e. melting point and glass transition) of pure polymer and blends. For pure P3HT, the DSC trace shows an exothermic peak of crystallization at 201 °C, while the endothermic melting peak is at 224.2 °C (fig. 5.1). The calculated melting enthalpy is 14.6 J g^{-1} that corresponds to a percentage crystallinity of 14.7 %, given that the melting enthalpy of perfect P3HT crystals is 99.0 J g^{-1} [132]. In the blends both melting and crystallization peaks shift to lower temperatures and, in particular, 204.3 °C, 196.8 °C and 195.3 °C for blends cast from CF, CB and DCB, respectively. In addition, I can observe a decrease of the area under the melting peak and a significant broadening of all peaks. The degree of crystallinity extracted from the P3HT melting peak is approximately 5.5 %, 4.0% and 4.5% for CF, CB and ODCB blends, respectively, which is consistent with a hindering of P3HT crystallites growth due to the presence of PCBM amorphous and crystalline domains[133, 134]. DSC data also suggest that casting from CB produces more homogeneous blends and indicates a slight increase in the phase separation following the order CB < ODCB < CF[135]. No clear signatures of a glass transition for either pure P3HT or blends were detectable at the chosen heating rate (10 °C min^{-1}). For semicrystalline systems such as P3HT, the observation of a glass transition is rather difficult as evidenced by the conflicting values available in the literature for both pure components and blend. A detailed calorimetric study on all four samples can in principle provide corroborating data, but falls out of my current scope.

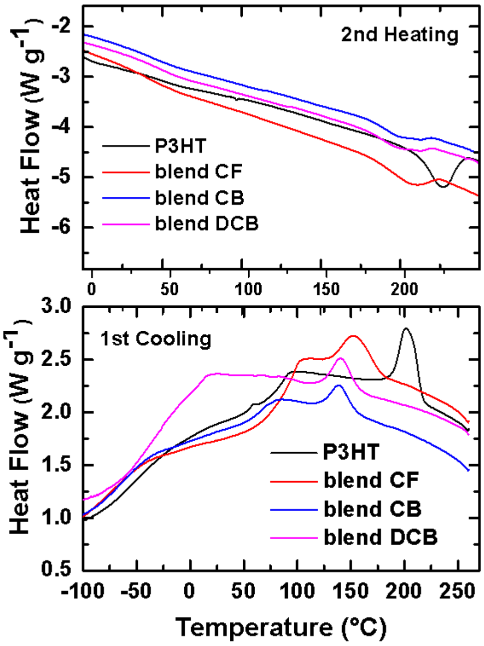

Figure 5.1: Heating and cooling curves from Differential Scanning Calorimetry at a scan rate of 10°C/min. Reproduced with the permission of Elsevier.

Fig. 5.2 (a) shows a typical XRD pattern for pure P3HT and P3HT-PCBM blends. It is well-known that head-to-tail regioregular P3HT crystallises into lamellar structures with two typical orientations: i) the backbone parallel to the substrate plane and the π- π stacking perpendicular (*face-on* orientation) and ii) the backbone perpendicular to the substrate plane and the π- π stacking parallel (*edge-on* orientation)[8]. In the case of preferential edge-on orientation, due to the lamellar stacking of the polymer chains, only the <100> reflections and its higher orders will appear using a symmetrical θ/2θ out-of-plane configuration. In contrast, an in-plane scan is required to reveal the <010> and <001> peaks which are related to the π-π stacking between thiophene rings and their alternate repetition along the backbone chain, respectively. In all my samples, P3HT lamellae are preferentially *edge-on* oriented, as we can infer from the strong <100> reflection at a d-spacing of 17.5 Å, consistent with the P3HT lamellae peak, and the simultaneous absence of <010> and <001> peaks in the XRD out-of-plane diffractogram. These results are in agreement with previous studies, where it has been found that slower evaporation deposition methods (i.e. drop casting) or high-boiling point solvents, facilitate slower growth of films, leading to the development of crystalline order already in as cast samples and, under these conditions, P3HT preferentially adopts edge-on configuration with the respect of the underlying surface[136]. Interestingly, I note different polymer crystallisation behaviours as a function of the solvent. In particular, the diffraction pattern suggests that the blend cast from CB possesses the best degree of order among the ones investigated here, as indicated by the higher intensity and the narrower shape for the polymer <100> peak (FWHM for annealed films are in the figure caption).

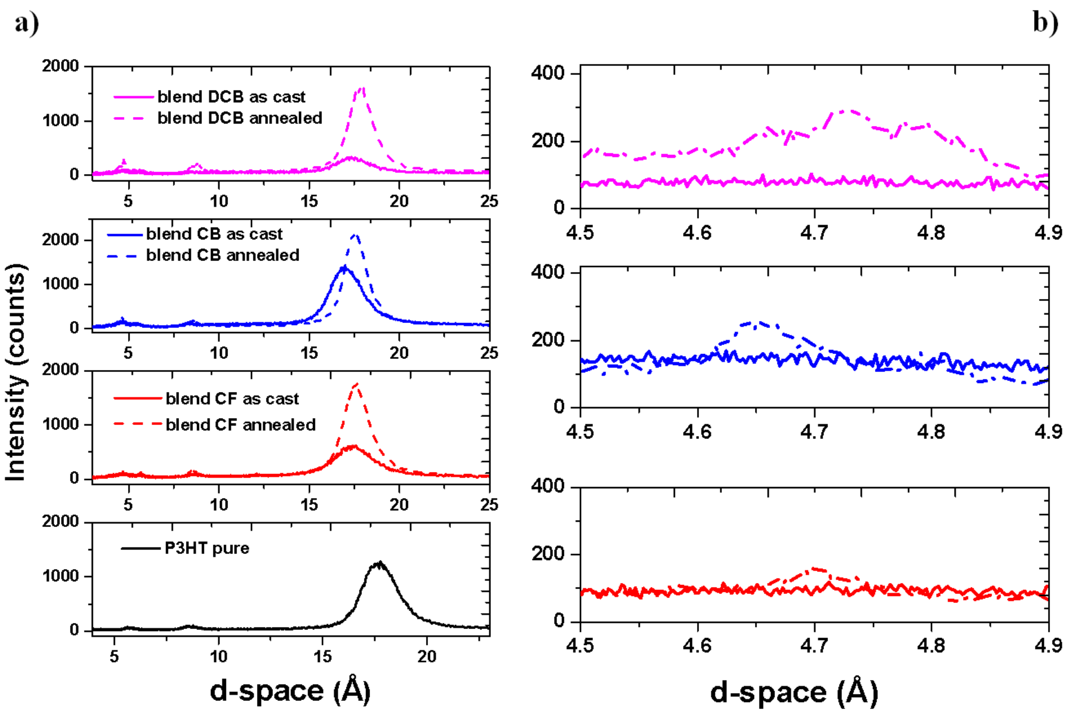

Figure 5.2: a) XRD pattern for pure P3HT and blends in their as cast and annealed states; (b) Zoom on PCBM Bragg peaks region. The full widths at half maximum are: 2.04 ± 0.01°, 1.95 ± 0.01°, 1.66 ± 0.01° and 1.79 ± 0.01° for P3HT, blend CF, blend CB and blend ODCB, respectively. Reproduced with the permission of Elsevier.

Let us now discuss the structural features of PCBM as a function of annealing and solvent. I can observe clearly that that annealing affects strongly PCBM crystallization (Fig. 5.2b), as a Bragg peak at 4.7 Å [64, 83] appears upon annealing, whereas only a broad futureless signal can be observed for as cast films. In addition, both XRD (fig 5.2b) and neutron diffraction (fig. 5.3) show a change in the shape and position of the PCBM Bragg peaks going from blends cast from CF and ODCB, to the blend cast from CB. This indicates that a different structure for the PCBM in the blend cast from CB, which is in agreement with a variety of results in the literature[83] and with my study (chapter 3) that highlight the prominent role played by the solvent during PCBM crystallisation.

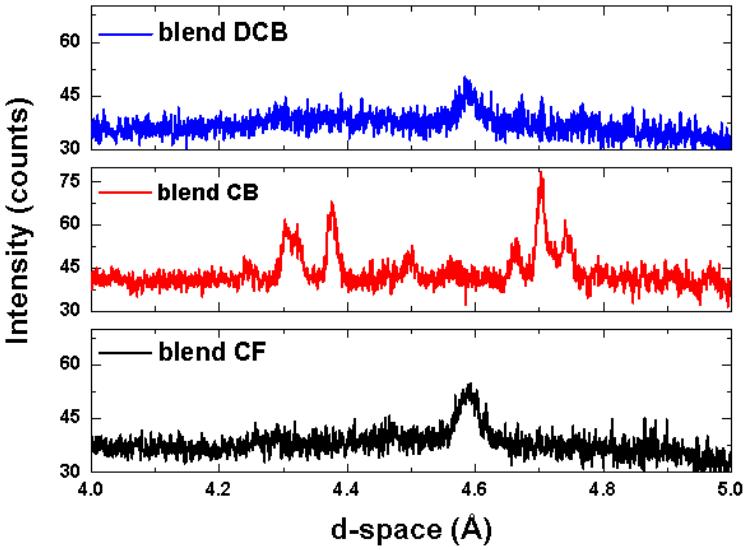

Figure 5.3: Neutron diffraction patter for blend cast from CF, CB and ODCB. Reproduced with the permission of Elsevier.

To summarise this section, DSC measurements suggest that the addition of PCBM leads to polymer:fullerene phase separation, with blend cast from CB featuring a less phase separated morphology. XRD data point towards a higher degree of polymeric order for the CB blend and a different PCBM crystalline structure. The achievement of such favourable interpenetrated nanoscale morphology in blend cast from CB might be ascribed to the higher solubility in this solvent for both P3HT and PCBM than in CF and ODCB[137]. In addition, CB can be seen as a better compromise between the lower boiling point solvent CF and the less volatile ODCB. In this scenario, the faster evaporation rate of CF would facilitate neither polymer crystallisation nor the formation of the P3HT-PCBM percolated and interpenetrated network. On the other hand, ODCB would lead to a strongly phase separated morphology, due to its high-lying boiling point.

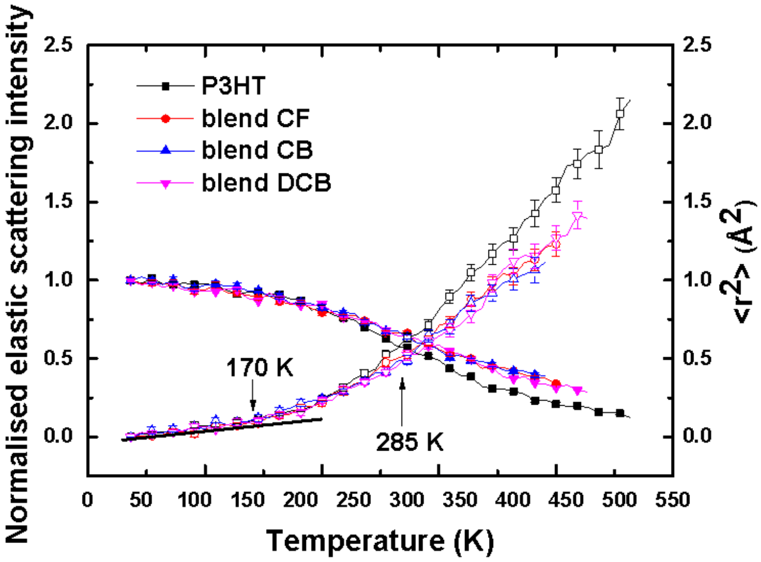

Figure 5.4: Elastic-scattering intensity at Q = 1.01 Å^{-1} (filled symbols) and mean square displacement (open symbols) as a function of temperature for blends and pure polymer. Reproduced with the permission of Elsevier.

In figure 5.4, I show the MSD of the hydrogen atoms alongside the elastic fraction vs. temperature. At temperatures below 170K, the systems show vibrations, whereas at ~ 170 K the first deviation occurs for both pure P3HT and blends, which I ascribe to the activation of hexyl side-group motions occurring at timescales of the order of picoseconds as can be measured by the IRIS spectrometer. These, in particular, could be trans-gauche conformational transitions or rotations. Segmental motions of the whole chain are not expected until the polymer T_g is reached. The plateau below 170 K indicates that the motion becomes negligibly slow below that temperature. This result is consistent with the electrical measurements performed by Obrzut and Page[126], which show an increase of the long-range order in electronic states of P3HT at a temperature below 180 K. At these temperatures the dynamics of P3HT is unaffected by the presence of PCBM. At temperatures around 285 K, (i.e. P3HT T_g according to Zhao et al[138]), we observe a second change in slope, and a retardation of the polymer dynamics upon blending: the elastic intensity of the blends is higher and the mean-square displacement lower. At first sight, the data shows no appreciable change as a function of the solvent. Therefore, although the solvent has an influence on the sample cristallinity the motion of the side chains is essentially unaffected at this lengthscale.

In fig. 5.5 is shown the comparison of the measured dynamic structure factor *S* ($\boldsymbol{Q}$, ω) as a function of energy transfer ΔE for all blends and pure polymer at Q = 1.01 Å^{-1}. The shape of the spectra shown in fig.5.5 consists of a superposition of two contributions: i) a Gaussians peak which corresponds to the elastic contribution to the overall scattering function and ii) a broad Lorentzian peak which is related to the energy exchanges between the sample and the neutrons near the elastic peak (*QENS*). Thus, a broadening of the scattering function corresponds to an increased mobility of the scattering centres. The scattering intensity has been normalised by the maximum scattering intensity for comparison. Consistent with the elastic scan data, at 330 K there is mobility of the side chains (broadening with respect to the resolution), and a slight retardation by the inclusion of PCBM. At 433 K these effects are much clearer, although data suggest that the solvent plays little or no effect in this regard.

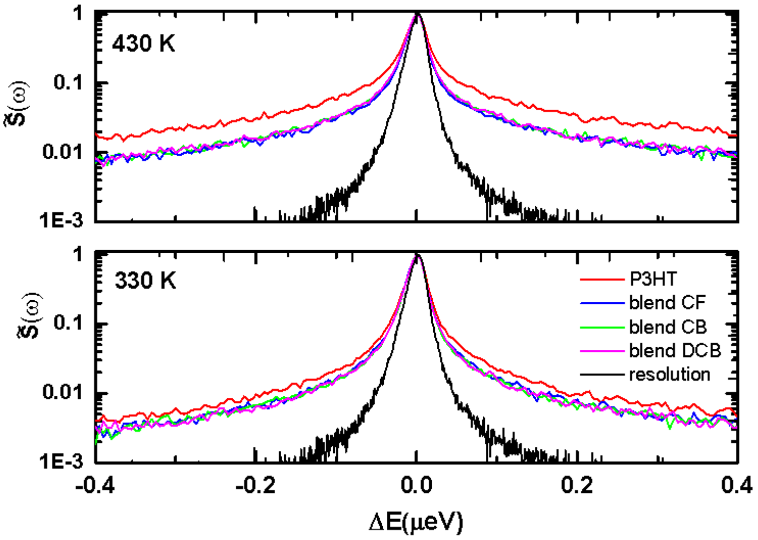

Figure 5.5: Measured structure factor as a function of energy transfer for pure polymer and all the blends at $\boldsymbol{Q}$ = 1.01 Å^{-1} . The black curve represents the instrumental resolution. Reproduced with the permission of Elsevier.

I fitted the intermediate scattering functions of all the samples with the KWW equation (figure 5.6a), and obtained the values of the fitting parameters τ, A and β. Although the $I(\boldsymbol{Q}, t)$ seems to confirm the scenario in which P3HT side-chain dynamics is slowed down by the presence of PCBM particles, the pre-exponential parameter A $(\boldsymbol{Q})$ (figure 5.6b) shows a strong excess of elastic fraction, especially at the ***Q***-values corresponding to PCBM crystal lengthscale. This, in particular, could make *QENS* data less reliable, as the side-chain dynamics retardation upon blending may be only apparent, and actually due to the increase of coherent scattering fraction in the blends.

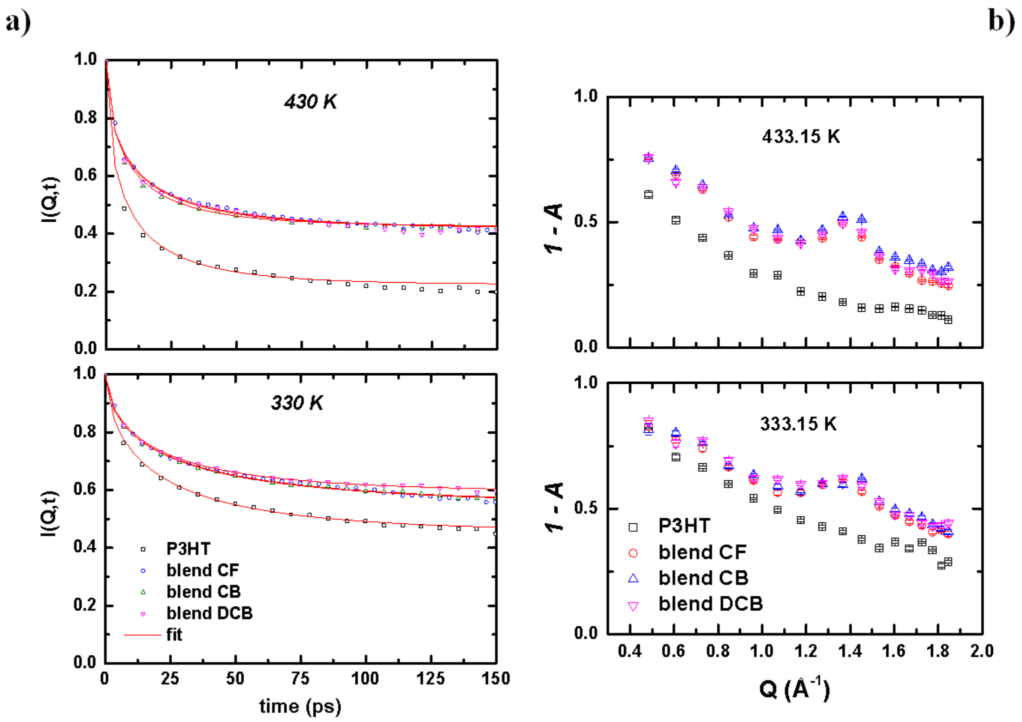

Figure 5.6: a) The intermediate scattering function for pure polymer and blends fitted with the KWW equation (red lines); b) 1-A parameter vs. ***Q***.

5.1.3 Conclusions

In this preliminary study I investigated the structural and dynamical behaviour of P3HT-PCBM blends as a function of solvent and annealing treatment. To the best of my knowledge this is the first investigation on both structural and dynamical features of poly(thiophene)/fullerene-derivatives blends. The combination of calorimetric, structural data from X-rays and neutrons diffraction suggests that CB is the best solvent for promoting long-range order in the blends. This might be explained in terms of favourable effect of CB especially on PCBM crystalline packing and P3HT morphology stabilisation. Particularly, the CB is a good compromise between the fast drying CF, which leads to an out-of-equilibrium morphology and the slow-drying ODCB, which would allow the growing of bigger and phase separated domains. Normalised elastic scattering indicates that the “liberation” of polymer side-chain occurs at 170 K for all the samples and the polymer motion seems to be frustrated with the inclusion of PCBM at temperatures above 285 K. In any case, the dynamics data suggests that the addition of PCBM increases the elastic fraction in the overall scattering intensity, likely due to either an increase of amorphous but not dynamically active domains in the system or to an increase of the coherent signal arising from PCBM crystallites or due to both effects. In this scenario the solvent influences only the degree of order and the homogeneity of the morphology, but does not play any significant role in the dynamics of the systems on a picoseconds timescale, dynamics that is mainly attributed to the hexyl side-groups.

To validate these results, and confirm that the frustration of the dynamics is real and not due to the increase of the coherent contribution upon PCBM addition, I needed to carry out additional experiments. With this in mind, we employed neutron polarisation analysis to separate effectively the coherent from incoherent contribution in such functional polymer:nanocomposite blends (section 5.2)

5.2 Neutron Polarisation Analysis of Polymer:Fullerene Blends

5.2.1 Introduction

As we have seen in the previous section, *QENS* connects useful structural and dynamical information by the measurement of dynamical incoherent (single particle) fluctuations in soft materials as a function of lengthscale. Extraction of these fluctuation rates can, however, be hampered by the presence of coherent contributions, originating from elastic scattering, and/or inelastic scattering modes that overlap in the space/time domain with the incoherent single-particle motions. In section 5.1, I have reported that the addition of PCBM frustrates polymer motion, possibly related to polymer confinement within PCBM domains. However, it seems that there is some excess elastic signal fraction at Q-values that correspond to the characteristic distance of PCBM crystals (see for example figure 5.6b). Calculation of the different contributions to the scattering cross-sections for a 1:1 P3HT:PCBM concentration yields incoherent and coherent contributions of ca. 75.5% and 5.5% for P3HT respectively, and 14% and 5% for PCBM respectively. Thus, three possible scenarios arise: i) the frustration of P3HT polymer dynamics is real (slowing down or increased elastic fraction), and it is due to P3HT-PCBM interaction and/or polymer confinement within PCBM domains; ii) the increase of the elastic fraction is largely due to the increase of coherent signal caused by PCBM addition and crystallisation; iii) a combination of the effects. It is therefore important to assess whether the excess of coherent contribution at this $\boldsymbol{Q}$-range affects data interpretation. To this end, neutron polarisation analysis can be a powerful method to disentangle collective events from single-particle motions in complex systems (see section 2.1.6). Although this technique has been already employed to discriminate between localised and non-localised motions in ionic liquids[139], it has never been used to investigate blends of semi-crystalline conjugated polymers with fullerene derivatives.

In the work presented here, I use neutron polarisation analysis to separate the coherent/incoherent scattering contributions in pure P3HT and in blends with PCBM, by making use of the diffuse scattering spectrometer D7 at ILL. We observe that, although the polymer motion seems to fall outside the instrumental time-window, this technique can be used effectively to discriminate the coherent/incoherent contributions in a multicomponent polymer:fullerene blend and, in general, in those systems in which the coherent contribution can make data analysis/interpretation non-trivial, i.e. in polymer:nanocomposite systems[140].

5.2.2 Experimental details

Materials and samples preparation: Regioregular P3HT (M_w= 10,000-40,000 g/mol) and PCBM were purchased from American Dye Source and used without further purification steps. Film of pure P3HT and blends of 50 wt% P3HT-PCBM were prepared by dissolving the two materials in chloroform separately with a concentration of 20 mg/mL, and mixing them in a 1:1 ratio. The resulting solutions were stirred overnight and drop-cast onto aluminium foil, yielding sample films or around 150 μm (transmission ~ 85%). The samples were vacuum-dried overnight at room temperature (RT= 20-25 °C) to remove any residual solvent.

D7 experiment: The diffuse scattering spectrometer D7 measures neutron scattering with polarisation analysis and, hence, unambiguously separates collective (nuclear coherent) and single-particle (nuclear incoherent) and magnetic scattering processes by means of xyz-polarisation analysis. This is a valid claim in cases where the incoherent scattering is dominantly spin-incoherent (i.e. due to the spin-dependent nuclear scattering length) and not isotope-incoherent (i.e. due to randomly positioned nuclear isotopes). This is a valid assumption for incoherent scattering for most H-containing materials. We used D7 with an incident wavelength of 5.7 Å which covers a similar $\boldsymbol{Q}$-range to that measured on IRIS (0.3 -1.8 Å^{-1}. I measured both in diffraction mode, to determine the structure factor of the pure polymer and P3HT:PCBM blends, and in inelastic mode to measure the QENS signal of the incoherent/coherent scattering using the Fermi chopper option. D7 is equipped with a supermirror analyser detector bank with an angular range of 132°. I measured the spin-flip and non-spin-flip scattering with the polarization axis normal to the scattering plane, with the axis preserved by means of a magnetic guide field (~10 G) that extended along the path of incident and scattered beams. The polarisation efficiency of the instrument was determined as 0.92 by measuring an amorphous quartz standard that gives only coherent non-spin-flip scattering. The detector efficiency was calibrated using a vanadium standard, and the instrumental energy resolution was estimated from the elastic linewidth of the vanadium (FWHM ~ 0.1 meV). The background contribution was evaluated by measuring the signal of empty cans and scaling it to the sample transmissions.

Data analysis: The data were reduced using the LAMP[141] suite of programs at the ILL and analysed using the DAVE[142] software package. The scattering signal in our system is dominated by the incoherent scattering of the hydrogenated side-chains of P3HT plus a small contribution due to PCBM side-group, as a consequence, any motion observed arises mainly from the dynamics of the polymer side chain. However, both P3HT and PCBM have measurable coherent contributions that, especially in the Q-range around the Bragg peaks, can make structural/dynamical data difficult to interpret. For the evaluation of the QENS signal, the instrumental resolution was measured at 2K for each sample. The best fit to the measured dynamical structure functions $S\,(\mathbf{Q},\omega)$ was obtained with a delta function that accounts for elastic events, and two Lorentzian functions to describe the quasi-elastic broadening. One Lorentzian can be related to fast-motions (~1 meV) and the other one to slower motions (~ 0.1 meV). Fitting with a delta plus one Lorentzian did not provide a satisfactory fit. The elastic fraction was calculated from the areas of delta and Lorentzian function and plotted as a function of momentum transfer vector Q.

5.2.3 Results and discussion

5.2.3.1 Diffraction with polarisation analysis

I used D7 in diffraction mode to determine the structure factor of pure P3HT and P3HT-PCBM blends. Figure 5.7 shows the coherent and incoherent signal contribution to the total diffraction pattern for pure P3HT (a) and in a blend with PCBM (b) separated using neutron polarisation analysis. The observed diffraction patterns seem to be consistent with the one obtained by means of x-ray diffraction in the previous experiment (figure 5.2a), with peaks at 0.37 $Å^{-1}$, 0.75 $Å^{-1}$ and 1.14 $Å^{-1}$ corresponding to the <100> lamellar peak and its higher orders in the edge-on orientation, while the peak at 1.66 $Å^{-1}$ is consistent with the <001> + <010> peak in a face-on lamellar orientation, and is indicative of a small fraction of lamellae adopting this geometry[143]. Note that this last peak could not be resolved neither via x-ray diffraction nor via the neutron diffraction experiment carried out using the IRIS instrument, probably because of the strong incoherent signal. If we now turn to the P3HT:PCBM blends (figure 5.7b), we can see that the addition of PCBM leads to two main effects namely: i) the appearance of the PCBM crystalline peak at 1.36 ± 0.1 Å^{-1} and 1.47 ± 0.1 Å^{-1} that can be assigned to the <221> and <22-1> planes of the PCBM monoclinic structure, respectively[64, 83], and ii) the scattering intensity upturn seen at low-***Q*** values (< 0.5 Å-1) that can be attributed to the scattering from the mixed P3HT-PCBM amorphous domains[144]. The parabolic shape of the incoherent signal in the P3HT-PCBM blend does not follow the usual decaying profile as a function of momentum transfer. This peculiar effect is not fully understood yet, and will be further analysed in more details in future works.

In general, the diffraction patterns indicate that the incoherent scattering intensity, which originates essentially from the polymer side-chains, does not change appreciably upon blending. In contrast, the addition of PCBM clearly enhances the coherent signal over the entire diffraction pattern. There is an increase in the coherent signal for the blend as compared with the pure polymer (addition 5%) and in particular, the main structural features of PCBM crystals become visible in the ***Q***-region probed (in the range 0.4 to 1.6Å^{-1})[145].

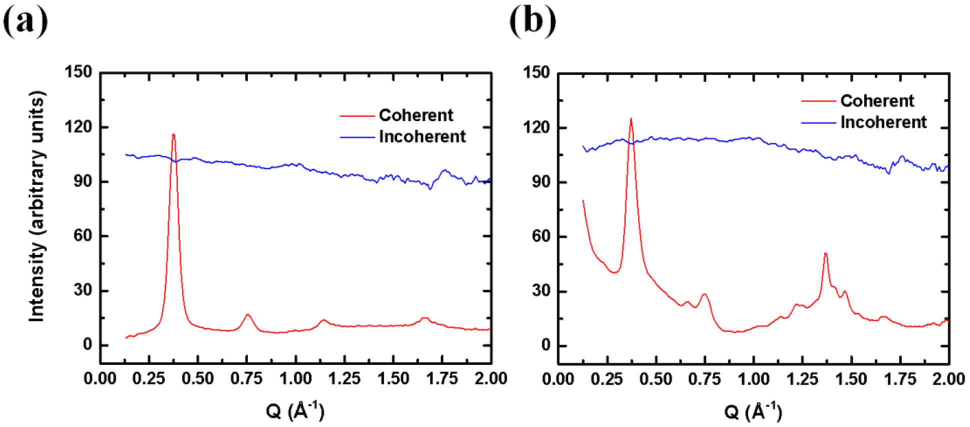

Figure 5.7: Coherent and incoherent contributions for P3HT (a) and P3HT-PCBM 1:1 blends cast from chloroform at 300K. Reproduced with the permission of Elsevier.

5.2.3.2 Quasi-elastic incoherent neutron scattering

We now turn to the study of the quasi-elastic signal. In figure 5.8, I show a comparison between the incoherent and coherent signal intensity taken at ***Q***= 1.2 Å^{-1} and 433 K. We can observe that the incoherent signal intensity is markedly predominant in both P3HT (a) and P3HT-PCBM blend (b), but that the coherent contribution increases upon addition of PCBM (3b). In addition, I do not observe any quasi-elastic coherent broadening for both samples (figures 5.8c,d) within the statistics of the measurement. This suggests the absence of correlated motions at the probed lengthscales and D7 timescale. However, collective motions could exist at longer timescales (nanoseconds). Thus, I will focus on the analysis of the QENS incoherent signal.

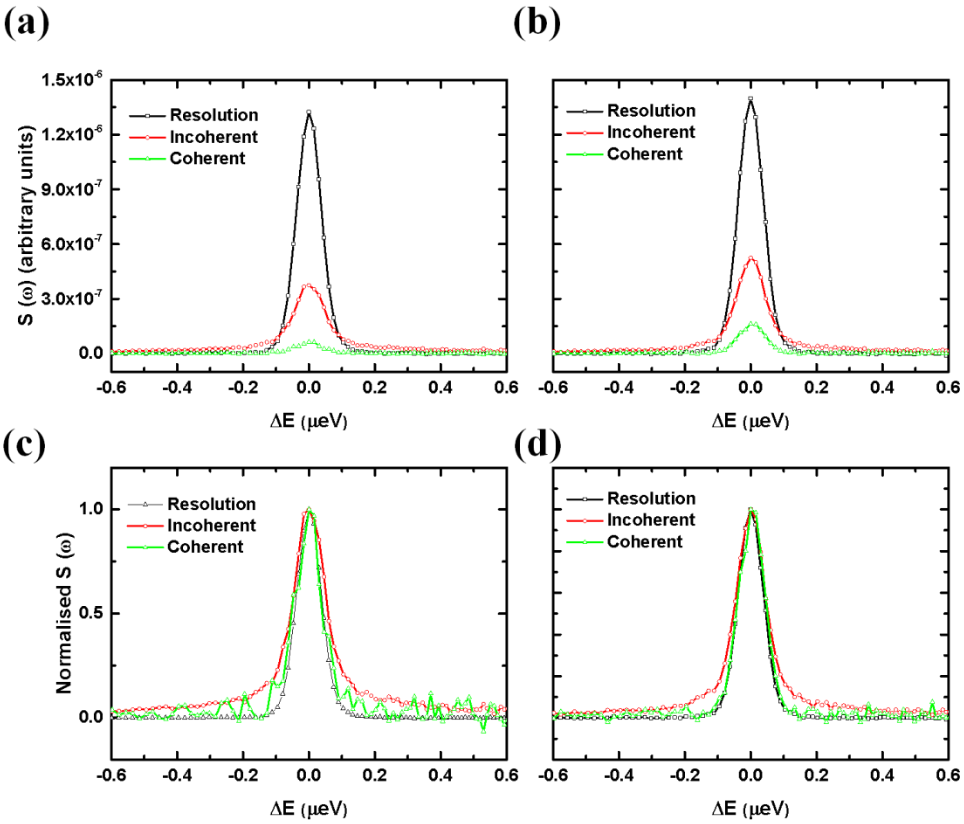

Figure 5.8: a) Incoherent and coherent dynamical structure factor for P3HT and b) P3HT:PCBM , taken at ***Q***= 1.2 Å-1 and 433 K for comparison. Normalised incoherent and coherent structure factor for c) P3HT and d) P3HT:PCBM. The normalised plots indicate clearly that both the samples do not feature any coherent dynamics, as the S (Q,ω)coh almost overlaps the resolution line. Reproduced with the permission of Elsevier.

In figure 5.9, I show the incoherent dynamical structure factor for pure P3HT, measured at three temperatures (300 K, 363 K, 433 K) in the ***Q***-range (0.3 – 1.8 Å^{-1}). The shape of the spectra is a convolution of two main contributions: i) a delta function within the instrumental resolution due to elastic scattering and ii) a broadening due to the single particle motions. Depending on the dynamical properties of the sample and on the probed instrumental timescale, the broadening can be split into two or more Lorentzians, which can be indicative of different type of motions in different time and spatial domains. The incoherent dynamical structure factor spectra for 1:1 P3HT-PCBM blends seem to feature the same characteristics as those of the pure polymer (figure 5.9b), with the exception of a slightly less broad signal for the blend between 1.2 - 1.5 Å^{-1} at 300 K. This effect might be related to the slowing down of the polymer side-chain dynamics, likely due to polymer confinement within the lengthscale of PCBM crystalline domains.

(a) P3HT

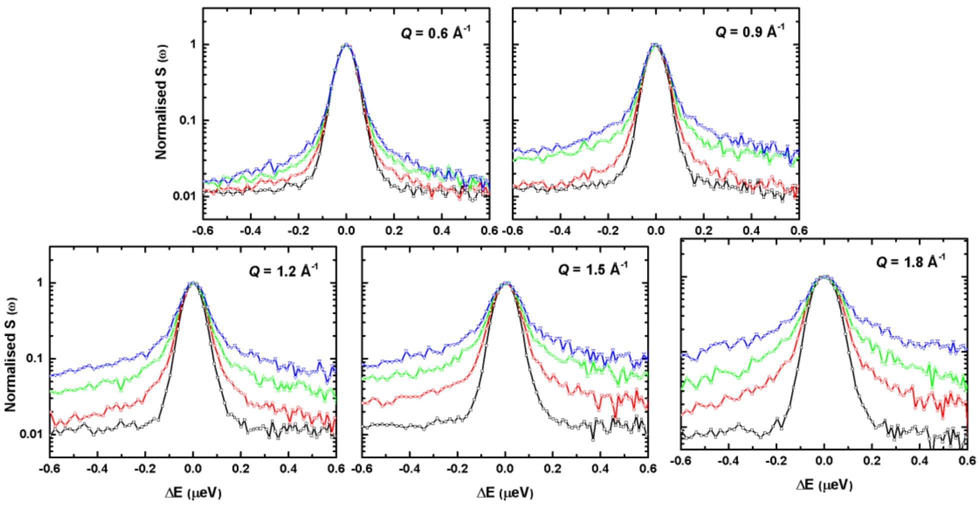

(b) P3HT-PCBM

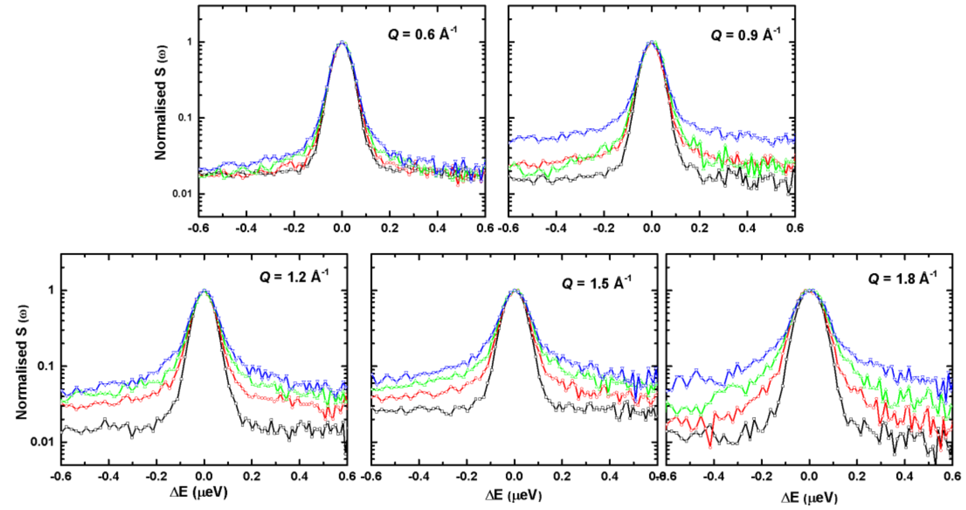

Figure 5.9: Incoherent dynamical structure factor determined from the spin-flip scattering a) for pure P3HT and b) P3HT-PCBM blends 1:1 blends, measured at three temperatures (black 2K, red 300 K, green 363 K, blue 433 K) in the 0.6 – 1.8 Å^{-1} ***Q***-range . All the spectra are reported in logarithmic scale and normalised to peak maximum (y-axis range 10^{-3} to 3) for comparison (y-axis range 5×10^{-3} to 3). Reproduced with the permission of Elsevier.

I fitted the spectra using a delta function, and two broad Lorentzians that account for faster (~ 1 meV) and slower (~ 0.1 meV) motions, all convoluted with the instrumental resolution measured at 2K. Figure 5.10 shows the elastic fraction and the FWHM of the two Lorentzians as a function of the momentum transfer ***Q***. The elastic fraction plots suggest that the polymer side-chain dynamics are likely being constrained by confinement between the PCBM crystallites, as indicated by the slightly higher value of the elastic fraction at around the length scale of PCBM crystals. Unfortunately, the statistical uncertainty of the data, as can be seen from the quasi-flat and erratic trend of both the Lorentzians, does not enable us to gauge if their mobility is retarded and we cannot carry out a more complete dynamical analysis on these samples. Furthermore the instrumental resolution of D7 (~ 0.1 meV) is poorer than that of IRIS (~ 0.02 meV), where polarisation analysis could give us further information for the longer timescale motions.

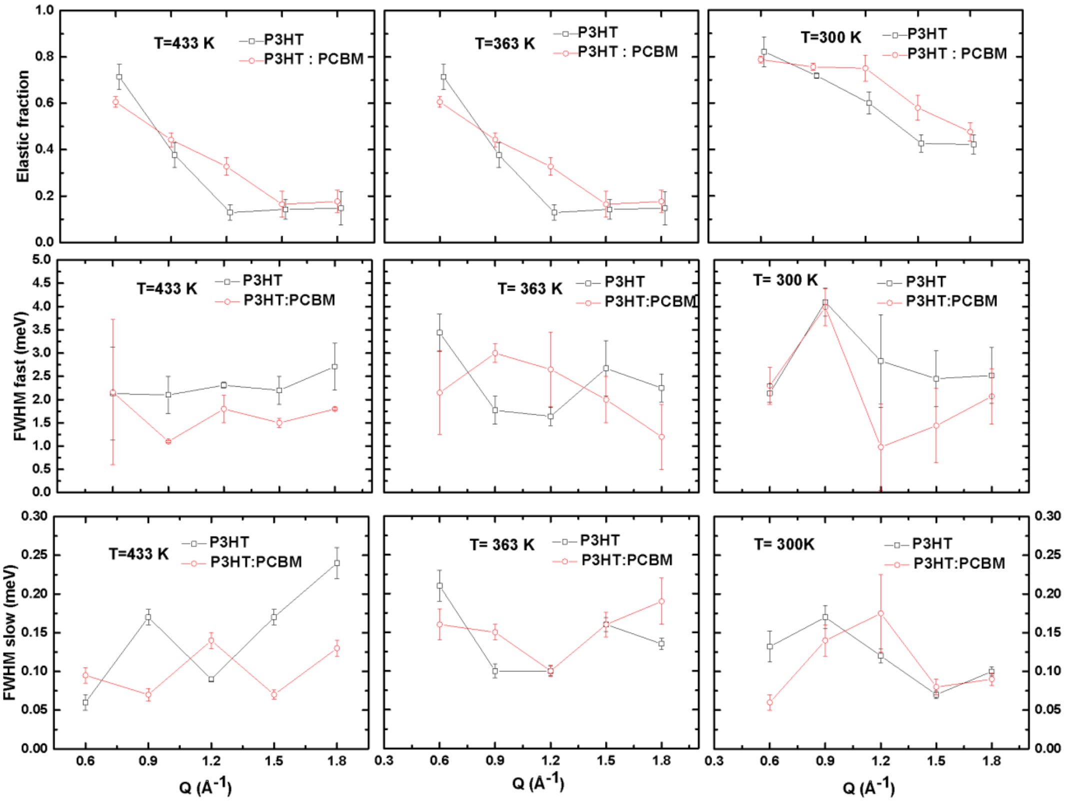

Figure 5.10: Elastic fraction of the pure polymer and P3HT-PCBM blend, as calculated from the ratio between the delta function area (elastic) and the two broads Lorentzians (inelastic), and the full width at half maximum (FWHM) of the Lorentzians as a function of the momentum transfer. Reproduced with the permission of Elsevier.

5.2.4 Conclusions

In this study, I performed an experimental separation of coherent and incoherent neutron scattering contributions on pure P3HT and P3HT: PCBM blends by means of neutron polarisation analysis. To the best of our knowledge, this is the first time that this method has been applied on this class of functional materials. Neutron polarisation analysis is the method of choice to separate effectively the coherent collective scattering contribution from the incoherent single-particle scattering, especially when the time/length scales of the two events overlap. For instance, the excess of elastic signal at around the PCBM d-spacing (1.4 Å^{-1}) can make dynamical data interpretation at this length scale prone to error.

I showed that by removing the strong incoherent contribution of P3HT, we can disclose new structural coherent features, such as the partial *face-on* orientation of the polymer crystalline lamellae. Investigations of the pure incoherent QENS via the analysis of the dynamical structure factor, suggest that that motions of the polymer side-chain in the timescale of a few picoseconds are constrained and possibly being slowed down upon addition and further crystallisation of PCBM buckyballs.

Although I could not carry out a more in-depth dynamical analysis due to the low statistics of the data and the lower instrumental resolution of D7 compared with IRIS, I feel strongly that neutron polarisation analysis combined with QENS is a powerful technique to separate different kind of motions in complex systems which cannot be treated as purely incoherent or coherent and yield confidence in the data analysis and interpretation. In the case of polymer systems, this pertains to most systems, blends, nanocomposites, systems with very specialised polymers which are difficult to deuterate, biopolymers or those used for bio-applications – in all these cases the signal is a mixture of coherent and incoherent scattering and QENS with polarisation analysis would clear the ambiguity in the interpretation of both structural and dynamical neutron data. In the experiments presented in this work, I was able to use QENS with polarisation analysis at a resolution of 0.1meV, but ideally I would like to be able to use the technique on neutron spectrometers of resolutions better suited to capture polymer glassy dynamics, in the hundreds of picoseconds and nanoseconds, such as backscattering spectrometers.

6 Neutron Radiation Tolerance of Two Benchmark Thiophene-Based Conjugated Polymers

In this chapter, I report the first study of the neutron radiation tolerance of two well-established poly(thiophene)s: P3HT and the liquid-crystalline PBTTT. I combine spectroscopic investigations with characterisation of intrinsic charge mobility to show that PBTTT exhibits significantly higher tolerance than P3HT. I explain this in terms of superior chemical, structural and conformational stability of PBTTT, which can be ascribed to its higher crystallinity, in turn induced by a combination of different molecular design features.

I thank Valentina Robbiano for the optical measurements, Dr. Keith J. Fraser for the XPS measurements and Dr. Christopher Frost for the assistance during the neutron irradiation experiment. The content of this chapter has been published as an open access paper in Nature Scientific Reports[146].

6.1 Introduction

Polymer semiconductors combine the excellent mechanical characteristics of polymeric systems with the unique optoelectronic properties arising from the partly-delocalised π-orbitals, thus enabling fabrication of flexible, mechanically-robust, and lightweight devices[147, 148]. Furthermore, since organic semiconductors can be easily processed over large areas using inexpensive solution-based methods, the related devices are relatively cheap to manufacture. The flexibility, low-cost, and strength-to-weight ratio of organic electronic devices present key advantages for those applications in which payload control is vital, such as space and avionic systems, which already heavily rely on the use of polymers as passive structural components[149]. Such benefits may also be exploited for smaller-scale applications, such as weather-balloons and mini-satellites, for which weight and volume requirements might even be more stringent than for spacecrafts. However, the influence of relatively harsh-radiation on such devices needs to be understood better. For instance, it is estimated that equipment on the International Space Station (ISS) receive an annual dose of ~2.8×10^{11} neutrons/cm^2 (secondary neutrons generated by the interaction of cosmic rays with the Station vs. 3.85×10^5 neutrons/cm^2 at ground level), with energies from 10^{-1} to 10^{11} eV[150].

Remarkably, there is no detailed study of the effect of neutron radiation on some of the most established organic semiconductors (OS), even though exposure to other types of radiation has been studied previously. For example investigations of solar cells based on P3HT and PCBM showed degradation of all cell parameters upon exposure to X-rays, also depending on the PCBM loading, but interestingly degradation could not be associated to any significant change in the structure of the active layers[151]. Instead, it was attributed to accumulation of excess charges generated by X-ray absorption at the electrodes. The latter can create a reverse electric field that reduces the built-in potential, in turn then affecting the open circuit voltage, V_{oc}. Street and collaborators[152] noted instead formation of deep-trap states in X-ray irradiated OPVDs that could act as recombination centres for charge carriers. More recently, the γ-rays tolerance of pentacene organic field-effect transistors (FETs) has also been investigated[153]. By means of X-ray and ultraviolet photoelectron spectroscopies (XPS and UPS respectively), the authors observed increased *p*-doping and newly generated states that facilitated hopping transport.

Surprisingly, to date there have been no studies on so-called “neutron radiation hardening” of organic devices, albeit neutrons represent one of the best tools to study the effect of cosmic rays, as an example of the most severe forms of radiation produced after nuclear interactions of the cosmic rays with the structural shielding of spacecrafts[154, 155] (see section 2.2.3). In general, it is thus crucial to shed light on the effects of neutron radiation with a broad energy spectrum, such as those available at a spallation source.

Here, I focus on two notable examples of conjugated polymers benefitting from a long period of development and refinement through a number of design, synthesis, and processing innovations and with significantly different degrees of crystallinity, namely: P3HT[156], and the liquid crystalline PBTTT[41]. In particular, I studied the effect of neutron irradiation on the optical, chemical and vibrational features of the polymers via ultraviolet-visible absorption (UV-Vis), XPS and Raman spectroscopy, and correlated these with the electrical properties as revealed by characterisation of FETs incorporating these materials as active layers.I also thermally annealed the irradiated samples to investigate reversibility. I show below that the two polymers behave rather differently, with PBTTT featuring a greater radiation tolerance than P3HT. This can be correlated to the higher crystalline order and the more rigid and structurally stable backbone of PBTTT, in turn resulting from the presence of the thienothiophene moieties and from a lower density of solubilising chains.

6.2 Experimental details

OFETs fabrication and characterisation: Regioregular P3HT (Aldrich) and C16-PBTTT (Merck Chemicals) were used as received, without further purification. P3HT and PBTTT solutions were prepared by dissolving 10 mg/mL in chlorobenzene at room temperature and in 1, 2 dichlorobenzene at 80 °C respectively. For the fabrication of bottom-gate/ bottom-contact OFETs, I started from n-doped silicon substrates with a 230 nm SiO2 layer, patterned with interdigitated indium tin oxide, ITO, (10 nm)/Au (30 nm) source and drain contacts (channel length, L= 5-20 μm and channel width, Z= 1 cm, purchased from Fraunhofer IPMS, Dresden, Germany). The substrates were sonicated in acetone and isopropyl alcohol for 10 minutes, dried in a flux of dry nitrogen and then placed in an oxygen-plasma asher for another 10 minutes to increase the substrate wettability and the Au electrodes work function. A hexamethyldisilazane (HMDS) layer was spin-coated on the samples, annealed at 100 °C for 1 h and spin-rinsed with isopropyl alcohol. Eventually, the active films were deposited by spin-casting the polymer solutions onto the transistor substrates (1500 rpm for 60 seconds). As PBTTT is soluble in chlorinated solvents only above 70° C, to prevent the formation of a defect-rich interface due to the quick crystallization of the solution upon contacting the cooler substrate, both the PBTTT solution and the substrates were kept at the same temperature (~70 °C) before spin-coating. All devices, except those of Figure 6.5 and table Table 6.3 were thermally annealed at 100 °C for 10 minutes as it is usual to improve the transistor performance. Therefore, with the term “pristine” I refer to devices that have not yet been exposed to neutrons, but that have been thermally annealed before such exposure. To look at the effect of the thermal “pre-annealing” I have also irradiated some devices that were not annealed soon after spin-coating, and report their properties in the discussion section of this chapter.

The OFETs characteristics were measured using a Karl Suss PM5 probe station and a HP4145 parameter analyser, which was connected to low-noise guarded probes for the source and drain-contacts and to the probe chuck for the gate connection. The HMDS/active-layer deposition and electrical characterization of the OFETs was carried out in a dry box under a nitrogen atmosphere with less than 20 ppm residual water vapour and 5 ppm oxygen.

The reported mobilities were measured in the saturation regime by taking the slope of the square root of the drain-source current I_{DS} plotted against the gate-source voltage V_{GS}, and then fitted to the saturation regime equation 1.4.

Neutron irradiation: To test the tolerance of P3HT and PBTTT to neutron radiation, I used the highly energetic flux of the VESUVIO beam line (in the range of MeV) at the ISIS Neutron and Muon Facility, (U.K.). The energy distribution of the neutron in the beam ranges from cold (0.025 eV) to fast (> 10 MeV) and ultrafast (> 20 MeV) neutrons. At the normal primary proton current (180 μA.hrs) the integrated neutron flux above 10 MeV was determined to be $5.82 \times 10^4 \cdot n \cdot cm^{-2} \cdot s^{-1}$ [61, 62]. In our experiment, I irradiated each sample with a total 7.8×10^8 neutrons with energies higher than 0.1 MeV per and 2×10^{15} neutrons cm^{-2} for neutrons with energies from 1 eV to 0.1 MeV (irradiation time = 4.5 hrs). All the neutron irradiation process was performed in air.

X-ray photoelectron spectroscopy: XPS spectra were acquired using a Thermo Scientific K-Alpha photoelectron spectrometer with a monochromatic Al Ka source (1486.6 eV) and spectral intensity > 2.5 Mcps at FWHM 1.0 eV on Ag 3d 5/2. The fitting procedure was carried out by using CasaXPS software.

UV-VIS and Raman measurements: For the optical measurements, P3HT and PBTTT solutions were spin cast onto fused silica substrates (Spectrosil®). UV-Visible absorption measurements were done with a photo-spectrometer (Agilent 8453). Raman spectra were collected using a Renishaw inVia Raman microscope (50× objective) with an excitation wavelength of 785 nm (non-resonant conditions). The laser power was set at 1% of its maximum power to avoid photo-degradation of the sample (1- 5 mW). The spectra were taken at RT in the Stokes' region and were calibrated against the 520.5 cm^{-1} line of an internal silicon wafer. The signal-to-noise ratio was enhanced by repeated acquisitions. All spectra were corrected to subtract the samples fluorescence background.

6.3 Results

6.3.1 XPS and UV-VIS absorption

First, I combined XPS and UV-Vis to quantify the impact of neutron radiation on the chemical and optical features of the macromolecules, and gain insight into the neutron-induced degradation mechanism. XPS spectra (and fits) of the S 2p peaks are shown in figure 6.1(a). The S 2p peak of "pristine" P3HT and PBTTT consists of two main components, namely S $2p_{3/2}$ and S $2p_{1/2}$, arising from the spin-orbit splitting in the p-type orbitals. Here I use pristine to indicate films that have not been yet irradiated, but that were subject to a 10-minutes annealing at 100 °C after spin-coating. The area ratio between these two components was maintained in the fits at 2:1, to account for the degeneracy of each spin state, and I selected an energy separation of 1.2 eV, as described elsewhere[157, 158].

Neutron irradiation leads to significant and irreversible changes of both polymers, as can be inferred from the clear broadening of the S 2p lines, which alongside the chemical shift to higher binding energy (0.1 eV) has been linked to the presence of a positive charge on the sulfur resulting from oxidative doping[157-159] of poly(thiophenes). Notably, thermal annealing after irradiation leads to a further shift of + 0.1 eV for P3HT, but not for PBTTT.

From a quantitative point of view, and starting with the pristine polymers first I note that the S 2p peak is fitted well with a $2p_{3/2}$/ $2p_{1/2}$ doublet, plus a small extra-component at higher binding energies (namely 166.2 eV and 166.6 eV for P3HT and PBTTT, respectively) that might account for a slight oxidation of the surface owing to unavoidable exposure to oxygen and moisture during handling (see table 6.1 for the fitting parameters). Quite significantly, however, I need an additional component to fit the S 2p line of the same films after irradiation (164 eV for P3HT and 164.5 eV for PBTTT). I note two further remarkable features here: first, the total area of the extra components is higher for P3HT than for PBTTT (i.e. the sums of the components at~ 166 and 164 eV are ~36.8 % and 24.8%, respectively of the total area of the features between 160 and 170 eV), and second, it keeps growing upon annealing (to 40.6% and 31.4 % for P3HT and PBTTT, respectively), thus indicating that the population of such species is enhanced, especially for PBTTT.

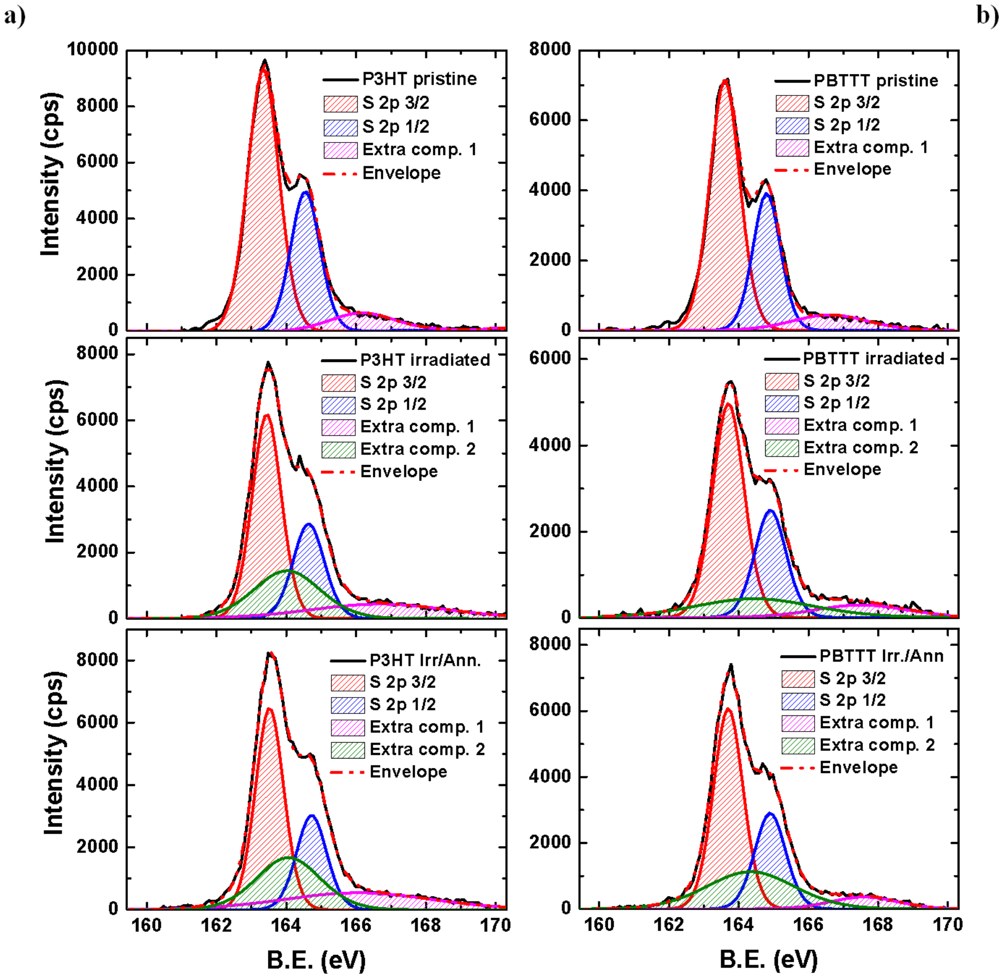

Figure 6.1: a) XPS spectra (counts per second, cps vs. binding energy, B.E.) for pristine, irradiated and irradiated/annealed P3HT and PBTTT films (thickness ~ 80 nm) on silicon/silicon oxide substrates, alongside with their fitting components. The XPS data were taken at a take-off angle of 90° for all the samples. The component centred at ~166 eV (purple line) is attributed to oxidative damage related to sample-handling, whereas the 164/164.5 eV component (green), can be ascribed to neutron-induced degradation, as absent from the spectra of pristine films. The annealing was carried out 150° C for 10 minutes in a nitrogen-filled glovebox. I thank Dr. K. J. Fraser for carrying out the XPS measurements.

Although, such a feature has been linked to the presence of polaronic species in oxidised poly(thiophenes)[157, 158], the oxygen content (table 6.1) estimated from XPS survey spectra do not correlate with the trend of the S 2p line, but indicate a reduction of oxygen upon annealing, thereby strongly suggesting that the feature at 164/164.5 eV, is mainly a neutron-induced effect.

Table 6.1: XPS fitting results for a) pristine, irradiated and irradiated/annealed P3HT.

P3HT	**Pristine** **Peak position** **Mass conc.**	**Irradiated** **Peak position** **Mass conc.**	**Irradiated/Annealed** **Peak position** **Mass conc.**
S (2p 3/2) neutral	163.34 eV 60.88 %	163.44 eV 42.14 %	163.52 eV 39.65 %
S (2p 1/2) neutral	164.54 eV 30.44 %	164.64 eV 21.07 %	164.72 eV 19.82 %
Extra component 1	166.16 eV 8.68 %	166.67 eV 14.34 %	166.06 eV 17.46 %
Extra component 2	- - -	164.02 eV 22.35 %	164.06 eV 23.07 %
O 1s	532.08 eV 2.33%	532.08 eV 6.77%	532.08 eV 5.7%

Table 6.2: fitting results for a) pristine, irradiated and irradiated/annealed PBTTT.

PBTTT	Pristine Peak position Mass conc.	Irradiated Peak position Mass conc.	Irradiated/Annealed Peak position Mass conc.
S (2p 3/2) neutral	163.60 eV 60.42 %	163.70 eV 50.12 %	163.70 eV 45.78 %
S (2p 1/2) neutral	164.80 eV 30.21 %	164.90 eV 25.06 %	164.90 eV 22.89 %
Extra component 1	166.61 eV 9.37 %	167.50 eV 8.42 %	167.59 eV 6.17 %
Extra component 2	- - -	164.45 eV 16.40 %	164.34 eV 25.16 %
O 1s	533.08 eV 3.88%	533.08 eV 6.46%	533.08 eV 4.55%

I also find indications of increased energetic disorder in the UV-Vis spectra of P3HT and PBTTT (figure 6.2). In fact, I observe loss of the vibronic progression on the low-energy side of the first absorption peak (~ 555 nm and 605 nm, respectively), that is commonly associated with a high degree of inter-molecular order in regioregular P3HT[160]. A slight blue-shift (~0.1 eV, ~11 nm) of the main absorption feature can be accounted for by both disruption of conjugation and inter-chain order. An irradiation-induced increase of the "sub-gap" optical absorption, taken together with the XPS data above, suggests a transition from neutral to oxidised (polaronic/bipolaronic) states in poly(thiophene)[161] and the concomitant formation of defects in the gap. Also in good agreement with the XPS data, these changes are more prominent when a thermal treatment is carried out on the irradiated films, as we observe a further blue-shift (~ 0.1 eV) and even stronger sub-gap absorption, so prominent for P3HT to suggest development of an additional peak in the low-energy region (~ 1.6 eV). Remarkably, both blue-shift and growth of sub-gap tail are significantly less pronounced for

PBTTT compared to P3HT (despite very similar neutron scattering cross-sections), and especially before the post-irradiation annealing.

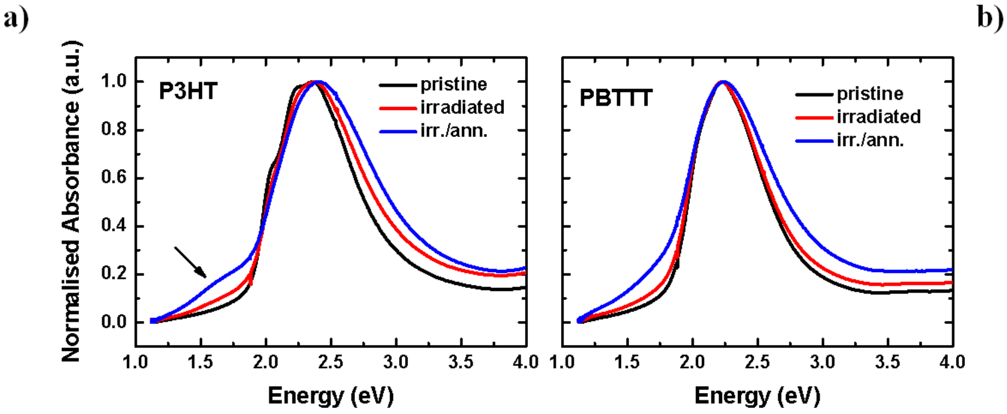

Figure 6.2: Normalised UV-VIS absorption spectra for a) P3HT and b) PBTTT pristine, irradiated and irradiated/annealed films (~ 80 nm, on spectrosil substrates, at room temperature). The annealing was carried out at 150° C for 10 minutes in a nitrogen glove-box. I thank V. Robbiano for the optical measurements.

6.3.2 Raman spectroscopy

I now turn to Raman spectroscopy to obtain a deeper insight into the neutron-induced modifications of the two polymer films since Raman and more generally vibrational spectroscopies have been used effectively to assess fundamental structure-property relationships of polyconjugated systems[162, 163].

I report the full spectra in the 600-1600 cm^{-1} region (figure 6.3a-b), but focus mainly on the 1300-1600 cm^{-1} region (figure 6.3c-d). This is particularly interesting because it includes the two main in-plane ring modes: the C=C symmetric stretching at 1445 cm^{-1}, and the C-C intra-ring stretching at 1380 cm^{-1}, that are known to be sensitive to π-electron delocalisation[164] and degree of structural order[165] in poly(thiophenes).

Starting first with P3HT, I can summarise the effects of neutron irradiation as follows:

(i) A general broadening of the spectral features in the 1300-1600 cm^{-1} region for the irradiated samples. Such a broadening increases further after thermal annealing of the irradiated sample, indicating lack of recovery and actually further degradation induced by the treatment. A similar broadening has previously been ascribed to a decrease of the degree of molecular order and conjugation length in poly(thiophene) films[165, 166].

(ii) A new low-energy wing of the C=C symmetric stretching peak appears at 1430 cm^{-1} after irradiation. This contribution has been previously assigned to the symmetric C=C stretching mode of the quinoid units of oxidised P3HT[167]. Appearance of the 1430 cm^{-1} band has also been observed when P3HT is exposed to the combined action of UV light and oxygen[168], and linked to an order/disorder transition taking place upon oxidation of P3HT chains to their quinoid form[169]. In full agreement with the previously mentioned trend, thermal annealing enhances such a wing, instead of favouring recovery to the pristine form, thus amplifying and possibly consolidating the neutron-induced damage in the polymer.

(iii) The appearance of the anti-symmetric C=C stretching peak at 1515 cm^{-1} and the concomitant enhancement in the C-C inter-ring peak at 1210 cm^{-1} and the C-S-C ring deformation peak at 728 cm^{-1} (figure 6.3 a). We assign these to formation of non-coplanar segments in the chains in agreement with previous literature that used chemical doping to drive formation of polaronic species[167, 169, 170], which are expected to induce torsional disorder along the polymer backbone, consistently with suppression of the thiophenes rigidity and conjugation.

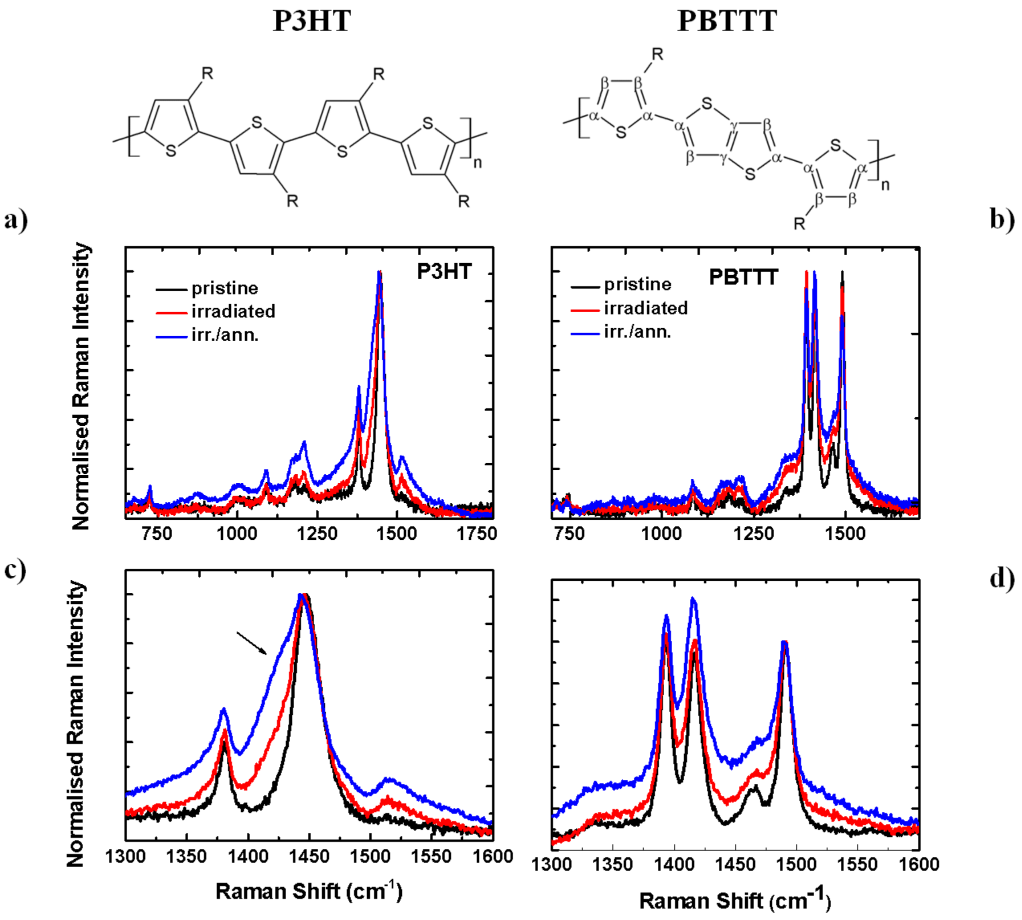

Figure 6.3: a) Full Raman spectra for P3HT and b) PBTTT thin films (~ 85 nm) on spectrosil substrates for excitation with a diode laser at 785 nm, at room temperature. All P3HT and PBTTT spectra are normalised to the peak intensity at 1445 cm^{-1} and 1490 cm^{-1}, respectively. c) Zoom in the 1300-1600 cm^{-1} region for P3HT and d) PBTTT. I thank V. Robbiano for the assistance during the Raman characterisations.

Let us now turn to the Raman spectra of PBTTT (figure 6.3 b and d) and focus first on the C=C-C ring stretch region at 1350-1550 cm^{-1} that is known to be representative of ‘skeleton” vibrational modes strongly sensitive to the extension of the π-π delocalisation[164] . I observe four strong peaks at 1393, 1418, 1463, and 1493 cm^{-1}. These correspond to C_{β}-C_{β} intra-ring stretch, C_{γ}-C_{γ} intra-ring stretch, C_{α}-C_{α} inter-ring stretch and C_{α}-C_{β} intra-ring stretch, respectively[109] (please see figure 6.3 for the labelling convention of the different carbons). I note a general broadening of the spectra in this region, with the Cα-Cα inter-ring stretch peak at 1463 cm^{-1} predominantly affected by the post-radiation thermal annealing. This may indicate an increased conformational disorder of the backbone upon irradiation, even though the polymer largely retains its overall conformational order, as suggested by the minimal changes occurring in the other in-plane backbone modes and in the C-C inter-ring peak at 1210 cm^{-1}, in the C-H bending at 1084 cm^{-1}, and in the C-S-C ring deformation mode at 700 cm^{-1}.

To summarise, the Raman data agree well with the XPS and optical absorption, consistent with a neutron-induced doping process as the main degradation pathway for irradiated P3HT and PBTTT, with PBTTT exhibiting a higher radiation tolerance.

6.3.3 OFET characteristics

The optical and chemical changes observed suggest that PBTTT is intrinsically more resilient than P3HT following neutron irradiation and provide a first indication of the material design criteria to be followed to increase radiation hardness of conjugated polymers. However, a more direct and quantitative evaluation of the mobility and overall transport properties is needed for applications such as FETs and more generally logic circuits. I therefore investigated the influence of neutron irradiation on FETs incorporating P3HT and PBTTT. In addition, irradiated devices were thermally annealed to establish whether radiation-induced effects are reversible.

Figure 6.4 shows the transfer characteristic for P3HT and PBTTT respectively, taken at V_{DS} = - 80 V. In P3HT-based devices both the current and the mobilities decrease after irradiation, but, surprisingly, if thermally annealed after the irradiation step, the mobility is almost recovered to ~ 92 % of the initial value (table 5.2a). On the other hand, the threshold voltage V_T (table 5.2b), as well as the OFF current (table 5.2c) and the sub-threshold slope (table 5.2d) increase when going from the pristine to the irradiated and irradiated/annealed devices. The increase of those parameters suggests that neutrons lead to formation of permanent charged defective species in the channel, consistent with oxidative doping, in P3HT[171] .

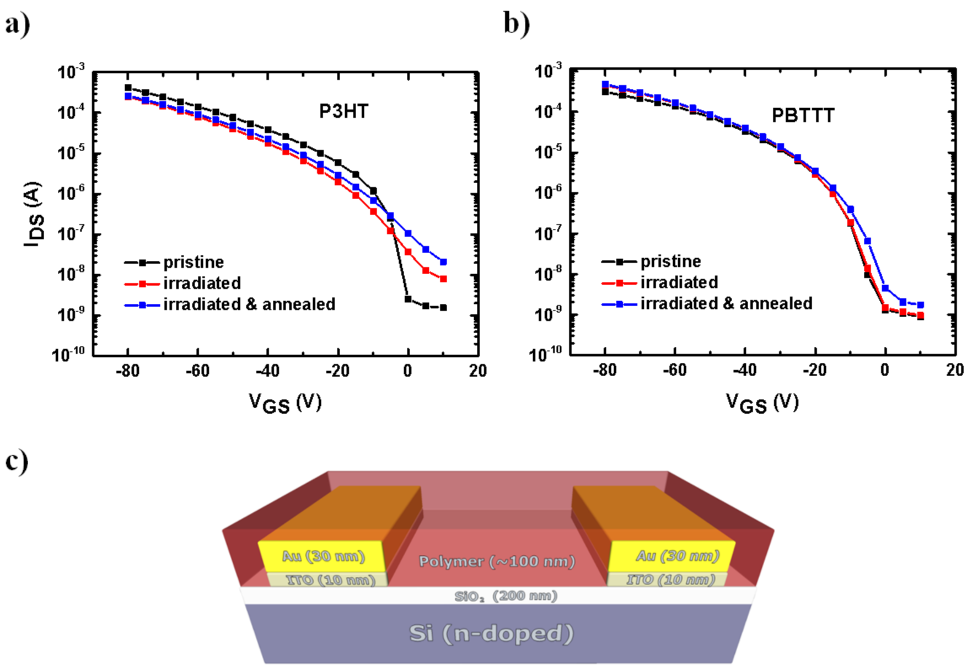

Figure 6.4: a) OFET transfer characteristics for P3HT and b) PBTTT taken at V_{DS} = -80 V; c) sketch of bottom gate/ bottom contact OFET architecture.

In stark contrast to P3HT devices, PBTTT-based ones only display a marginal increase of mobility, V_T and sub-threshold parameters (OFF current and sub-threshold slope) even after post-radiation annealing. Therefore, the electrical characteristics correlate remarkably well with the optical, XPS and Raman results above, providing clear corroborating evidence of a significantly higher tolerance to neutron radiation of PBTTT vs. P3HT.

Table 6.3: FETs mobilities calculated in the saturation regime (VDS = -80 V and VGS between 0 and -80 by using equation 1. The numbers in parentheses represent the uncertainty of the averaged taken over six different devices.

	Mobility pristine (cm^2 V^{-1} s^{-1})	**Mobility irradiated (cm^2 V^{-1} s^{-1})**	**Mobility irr./ann (cm^2 V^{-1} s^{-1})**
P3HT	0.012(4)	0.004(1)	0.011(1)
PBTTT	0.044(1)	0.044(1)	0.046(1)

Table 6.4: Threshold voltage (V_T) for pristine, irradiated and irradiated/annealed P3HT and PBTTT transistors. The numbers in parentheses represent the uncertainty of the averaged taken over six different devices.

	V_T pristine (V)	**V_T irradiated (V)**	**V_T irr./ann (V)**
P3HT	-16.8 (8)	-21 (2)	-18 (2)
PBTTT	-13 (1)	-19 (5)	-20 (3)

Table 6.5: ON/OFF ratio for pristine, irradiated and irradiated/annealed P3HT and PBTTT transistors. The numbers in parentheses represent the uncertainty of the averaged taken over six different devices.

	ON/OFF ratio × 10^6 pristine	**ON/OFF ratio × 10^6 irradiated**	**ON/OFF ratio × 10^6 irr./ann.**
P3HT	0.3 (2)	0.027 (5)	0.0095(9)
PBTTT	3.9 (3)	1.9 (6)	1.1 (4)

Table 6.6: Sub-threshold slope and values for pristine, irradiated and irradiated/annealed P3HT and PBTTT transistors. The numbers in parentheses represent the uncertainty of the averaged taken over six different devices.

	Sub-thr. Slope pristine (V/decade)	**Sub-thr. Slope irradiated (V/decade)**	**Sub-thr. Slope Irradiated/annealed (V/decade)**
P3HT	3 (1)	10 (2)	11.5 (3)
PBTTT	2.3 (6)	2.9 (5)	3.6 (2)

6.4 Discussion

The combination of chemical, optical, vibrational and electrical characterisations suggests that neutron irradiation leads to oxidative-like doping of the materials. In addition, my findings indicate that the population of such doped species, and the subsequent decrease of conformational order in both polymers is amplified by the post-irradiation thermal annealing. However, although the degradation mechanism appears to be in principle similar for P3HT and PBTTT, the two polymers show a different tolerance, with PBTTT being more resilient than P3HT. Disruption of the chemical and electronic order upon irradiation and post-irradiation annealing deteriorates the switching ability of P3HT devices affected by a steep drop of the ON/OFF ratio, consistently with a neutron-induced doping in the material. Hole-mobility decreases after irradiation, although it recovers partially (92 %) its initial value if the device is thermally annealed. This is surprising, as one would expect that a higher amount of doped chains would lead to an increase of the charge mobility. In fact, this regime of hole-mobility has been observed by Neher and co-workers for chemically-doped P3HT[172]. They noticed a mobility decrease at low-to-medium doping levels, for which the beneficial effect of doping is compensated by the deleterious increase of energetic disorder, but an increase at sufficiently-high doping levels. We propose that the same phenomenon also occurs in our system, in which the thermal annealing drives the transition from a low to a moderate doping regime, thus enabling partial recovery of the hole-mobility.

Turning to the actual neutron-induced degradation mechanism, I first consider the experimental radiation environment. Comparison between the experimental neutron energy spectrum at the VESUVIO beamline[63] and the calculated energy spectrum of the neutrons generated on board the ISS[150] as a result of its interaction with cosmic radiation is shown in figure 6.5. In both cases, the energy spectrum is extremely broad, ranging from cold to ultrafast neutrons. This may lead to a plethora of different neutrons-nuclei events, depending on the neutron energy and nuclei properties (i.e. absorption and scattering cross-sections). However, we can clearly observe that the VESUVIO spectrum is significantly more intense in all the regions, with the ISS spectrum being seven orders of magnitude less intense for epithermal-neutrons (10^{-6}-10^{-1} MeV). My experiment is thus an accelerated irradiation test, which enables mimicking several years of space irradiation in only a few hours. E.g. focusing on neutrons with energy > 10 MeV, for which the nominal value for the VESUVIO flux is 5.82 × 10^4 n cm^{-2} s^{-1}, I estimate that in 4.5 hrs our samples received the equivalent of ~ 45 years of irradiation on the ISS.

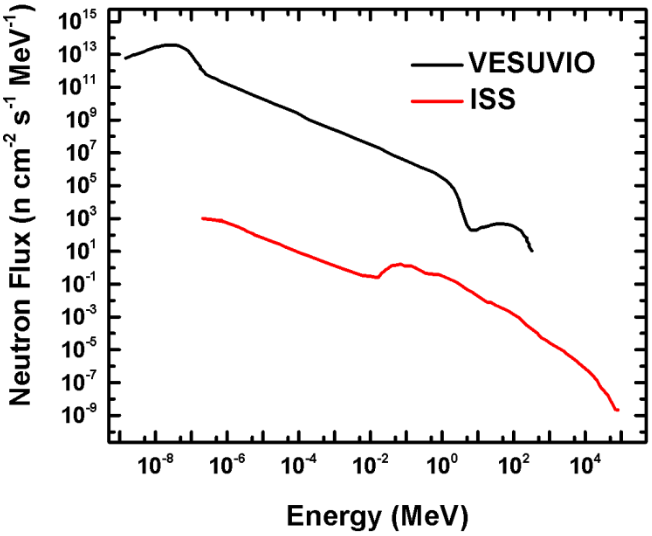

Figure 6.5: Experimental differential neutron energy spectrum at VESUVIO[63] vs. estimated differential energy spectrum received by the ISS[150].

Neutron-induced damage can be classified as due to either ionisations by nuclear reactions/collisions, or to recoil, resonances and cleavage events. The former originate from direct neutron-nuclei collisions and involve mainly fast neutrons (> 0.1 MeV), whereas the latter can be attributed to the interaction of epithermal neutrons with the nuclei. If the deposited energy is large enough to break a C-C or a C-H bond (~ 4 eV), cleavage phenomena will follow. I consider that such events are likely to be responsible for the damage observed in our experiments because of the synergistic effects of the higher dose of epithermal neutrons in our experiment (2 × 10^{15} neutrons cm^{-2}) than fast (> 0.1 MeV) neutrons (7.8 × 10^8 cm^{-2}), and the high probability of interactions with epithermal neutrons (either by scattering or absorption) of such highly hydrogenated systems. The relatively strong tendency of conjugated polymers and of organic matter in general to scatter neutrons stems in fact from their significant content of hydrogen atoms, which exhibit the highest scattering cross section among the isotopes[10]. While I cannot completely rule out the presence of neutron-induced damage in the substrate (i.e. in the gate oxide), we did not observe any increase of the gate leakage current upon irradiation, thus suggesting most damage is within the highly-hydrogenated active layer.

I thus propose that neutron-induced degradation of these polymers is a radical mechanism likely activated by hydrogen or alkyl abstraction, as for x-rays[152] and UV-irradiated P3HT[173] but activated in this case by direct neutron-nucleus collisions (fast neutrons) or by inelastic processes (epithermal neutron/hydrogen interactions in the majority of cases), rather than by photo-generated electrons as for X-rays and UV[174].

Furthermore, it is useful to compare X-ray diffraction (XRD) spectra taken before and after the irradiation to extract further information on the influence of neutron irradiation on the crystalline fractions of the materials. Such XRD spectra do not show significant differences (figure 6.6) thereby indicating that neutron-induced structural damage on the crystalline phase of either polymer is either absent or below the XRD detection threshold. Such an observation powerfully correlates with the differences we noted already between P3HT and PBTTT and leads us to propose that the degradation process mainly occurs in the amorphous phase, in which the defective species (i.e. radicals) would also have a higher mobility and reactivity[175].

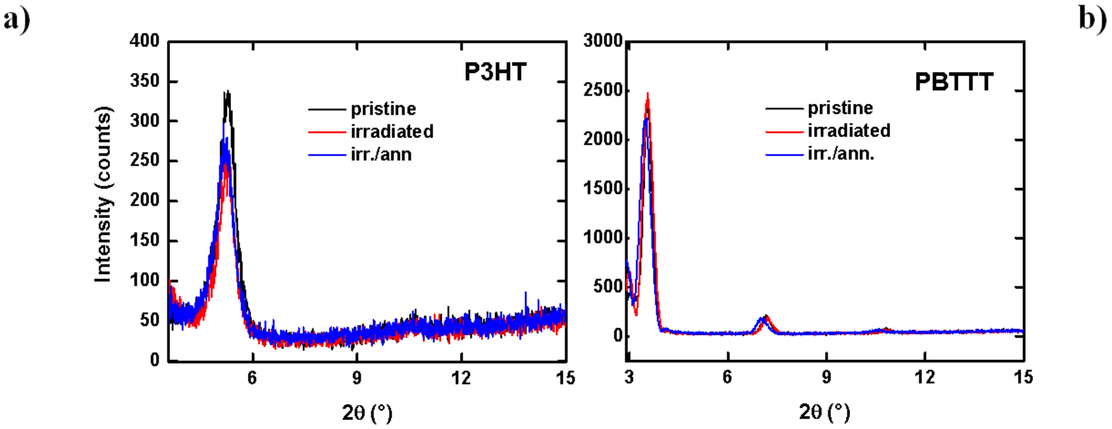

Figure 6.6: XRD pattern for P3HT (left) and PBTTT (right) for pristine, irradiated and irr./ann. films.

As an additional, concurrent factor, I note that crystalline regions might also act as traps for the radicals and hence slow down the degradation process, as previously observed for γ-irradiated cellulose[176] and carbohydrates[177]. In this scenario, thermal annealing of the irradiated films facilitates de-trapping of the radicals and thus exacerbates degradation, as indeed observed as the reduction of the P3HT transistors ON/OFF ratio. So we can explain the different degradation pathways of the two polymers in terms of a higher crystallinity of PBTTT. Effectively, a significant fraction of the neutron-induced defects are frozen at room temperature within the more extended crystalline phase, but with the possibility of being thermally activated. The prominent role played by the crystalline phase in (inhibiting) damage is further confirmed by the OFETs characteristics of non-annealed films (figure 6.7 and table 6.3)), in which the crystalline fraction is significantly lower than in the annealed ones. Remarkably, these demonstrate significantly lower tolerance for both non-annealed P3HT and PBTTT, with the drain current and hole-mobility increasing after irradiation for both polymers and before thermal annealing. This is in full agreement with the expectation of a higher concentration of radicals in the amorphous phase (now more extended that in the pre-annealed case), i.e. not “frozen” within the crystalline fraction, that do not need a post-irradiation annealing to be ‘activated’.

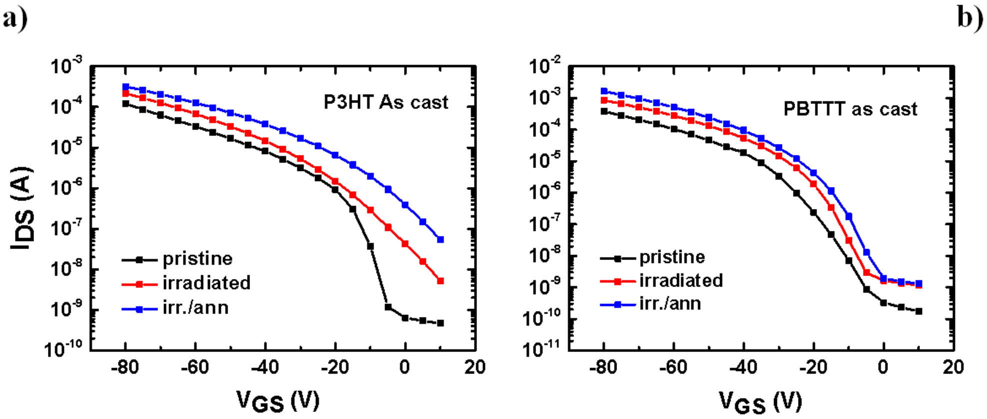

Figure 6.7: OFETs characteristics for a) P3HT and b) PBTTT devices that were not thermally annealed before the irradiation process.

Table 6.7: Hole-mobility values for P3HT and PBTTT films that were not thermally annealed before the irradiation process.

	Mobility pristine ($cm^2 V^{-1} s^{-1}$)	**Mobility irradiated ($cm^2 V^{-1} s^{-1}$)**	**Mobility Irradiated/Annealed ($cm^2 V^{-1} s^{-1}$)**
P3HT as-cast	**0.0046(2)**	**0.0066(3)**	**0.0072(3)**
PBTTT as-cast	**0.015(6)**	**0.020(9)**	**0.025(8)**

I thus attribute PBTTT's enhanced neutron radiation tolerance to a significantly more crystalline structure. Interestingly, this polymer was intentionally designed to assemble into large crystalline domains from a liquid-crystal phase, and exhibits a planar and rigid π-conjugated system, which eventually leads to high charge mobility (~ 1 $cm^2 V^{-1} s^{-1}$)[41]. It has been even suggested that in this material the chain interaction and ordering is favoured already in solution[178] and is preserved during the crystallization. Key guiding principles of such molecular design are: (i) the introduction of the linear conjugated co-monomer, thieno[3,2-b]thiophene, which facilitates the adoption of the low-energy backbone conformation and, hence, provides more conformational backbone stability; (ii) the low side-chain attachment density (in fact half than in P3HT), that permits interdigitation between the chains and the formation of stable and large three-dimensional crystalline domains[107].

6.5 Conclusion

In conclusion, I have investigated, for the first time, the neutron radiation tolerance of two polymeric semiconductors, namely P3HT and PBTTT. Neutrons represent one of the most disruptive components in cosmic-ray particle cascades, and pose a number of hazards to the electronic equipment in aircrafts, spacecrafts and orbiting objects. Evidence we collected through a variety of spectroscopic (XPS, UV-Vis, PL, Raman) and device characterisations (FETs) strongly suggests that neutron irradiation promotes the of polaronic species in both these polymers. Remarkably, degradation is much less pronounced in PBTTT, indicating a superior radiation tolerance of this polymer. I propose that the main degradation process is a radical, non-oxygen assisted mechanism, that can be rationalised as a “radiation-induced doping” taking place preferentially in the amorphous phase of the thin films. Compared to P3HT, PBTTT thus features superior radiation tolerance primarily as a result of its superior crystalline order. The results above provide molecular design guidelines for polymeric semiconductors with improved neutron resilience, and pave the way towards the effective utilisation of such polymer-based electronics for space and avionics applications.

7 Summary and Conclusions

This thesis aims to provide an insight on the nanoscale arrangement of conjugated polymers and fullerene, both in blend and in pure form. In particular, I show that the intermolecular interactions and self-organisation features play a crucial role in influencing the physical/chemical properties of these carbon-based materials.

In this chapter, I summarise the findings illustrated in this thesis work, and give some outlook about possible future experiments.

7.1 PCBM single-crystals

In chapter 3, I report, for the first time, the crystalline structure of solvent-free single-crystal PCBM resolved by means of microfocused x-ray diffraction. I note that both the dimension and the quality of these crystals (high lateral and vertical homogeneity) are unprecedented among the ones reported in previous literature. The high quality of these crystals is also confirmed by the metrological AFM investigations carried out at the National Physical Laboratory (NPL) by Dr. G. M. Lazzerini. The flatness and good lateral homogeneity suggest that these crystals would be ideal for probing the intrinsic optical properties and charge transport features of this functional material.

In regards of the optical characteristics of single-crystalline PCBM, Dr. Giulia Tregnago et al. have recently reported a study in which a vibrationally-resolved low-temperature photoluminescence, afforded by a complex interplay of Herzberg-Teller, Jahn-Teller and Franck-Condon effects, has been observed[179]. However, I could not obtain any reasonable result in determining the charge transport properties of our solvent-free crystals. In particular, I attempted to fabricate single-crystalline OFETs but I could not obtain any reasonable transistor characteristic and, thus, the field-effect mobility. This might be attributed to a poor contact between the oxide capacitor and the crystal surface, which in turn hinders the formation of a conductive channel at the semiconductor/oxide interface. In the next experiments, would be worth exploring different device architectures (i.e. bottom-gate/top-contact OFETs) and different experimental methods, such as time-of-flight conductivity measurements.

7.2 Tuning PCBM intercalation in PBTTT

In chapter 4, I show that we can exploit the strong self-organisation attitudes of the liquid crystalline PBTTT to tune the degree of PCBM intercalation in between the polymer side-chains. The extent of fullerene intercalation is in-fact crucial in determining the optimal polymer:fullerene ratio for effective charge photogeneration in OPVs.

By means of x-rays and neutron reflectivity, I observe that if we increase the solidification time of the pure PBTTT film the polymer self-organises better, and does not allow the fullerene particles to diffuse and intercalate. Different degree of intercalation leads to different optoelectronic properties, as revealed by the characterisation of OPVs incorporating these films as active layers.

In the next set of experiments, it can be interesting to investigate how the "in-plane" electrical characteristics (i.e. FE mobility) of PBTTT can be varied by tuning the degree of fullerene intercalation.

7.3 Neutron spectroscopy of poly(thiophene):fullerene blends

In this chapter, I present a structural and dynamical study of P3HT:PCBM blends. *QENS*, in particular, has allowed us to gain valuable information about the polymer dynamics in such functional polymer:nanocomposite systems.

In the first part, I observe that the solvent from which the solid blend is cast, determines the polymer and fullerene degree of order and polymer:fullerene phase separation. *QENS* data suggest that the polymer side-chain dynamics is likely being retarded by the presence of fullerene buckyballs.

In the second part, to verify whether such findings were real or due to the increase of coherent scattering contribution upon PCBM addition and crystallisation, I employed neutron polarisation analysis to separate experimentally coherent from incoherent signal. Although the instrumental resolution of the D7 spectrometer was not ideal for highlighting polymer side-chain motions, data suggest that polymer dynamics slows down upon blending with PCBM, as a result of polymer confinement within PCBM domains.

In the next experiments, it would be ideal to use polarisation analysis on neutron spectrometers with better resolution (~100 ps and nanoseconds), to investigate polymer glassy dynamics without the ambiguity given by the spatial/temporal overlap between the coherent and incoherent contribution. The precise determination of the glass transition temperature is crucial for selecting the proper annealing temperature necessary to promote long-distance diffusions and, hence, optimal phase separation in polymer:fullerene blends. However, calorimetry measurements do not seem to be precise enough to discriminate unambiguously such transition, given the relatively low amorphous fraction in semicrystalline conjugate polymers. In this context, neutron spectroscopic measurements in the nanosecond time-scale would help to capture such dynamical features also in such peculiar systems.

7.4 Neutron irradiation of organic electronics

In this chapter, I investigated the neutron radiation tolerance of two well-known polymer semiconductors: the benchmark polymer for OPVs P3HT, and the liquid-crystalline PBTTT. Neutron irradiation is a state-of-the art tool to test the resilience of electronic chips and constituent materials against cosmic rays exposure. In particular, a shower of highly energetic (MeV) secondary neutrons is generated upon interaction of the structural shielding of space/aircrafts with cosmic rays, causing both reversible and irreversible failure in electronics. Despite the fact neutron sources are employed extensively in mimicking cosmic rays exposure of inorganic-based electronics, this is the first time that these kinds of experiments are carried out on organic electronics. Interestingly, spectroscopic and electrical measurements point towards a superior neutron irradiation tolerance of PBTTT than P3HT, likely due to its superior self-organisation features (showed, for instance, also in chapter 4).

I have carried out neutron irradiation tolerance experiments of OPVs (not shown in this thesis), made of P3HT:PCBM and PBTTT:PCBM blends, to complement the measurements performed on OFETs, both in static and *in operando* conditions. Although data analysis is at an early stage, it seems that fullerene might somehow mitigate the detrimental effects of irradiation, probably because it may act as neutron-generated radicals scavenger[180].

References

1. Ito T, Shirakawa H, Ikeda S. Simultaneous polymerization and formation of polyacetylene film on the surface of concentrated soluble Ziegler-type catalyst solution. *Journal of polymer science: polymer chemistry edition* **12**, 11-20 (1974).

2. Chiang CK, *et al.* Electrical Conductivity in Doped Polyacetylene. *Phys Rev Lett* **39**, 1098-1101 (1977).

3. Shirakawa H, Louis EJ, Macdiarmid AG, Chiang CK, Heeger AJ. Synthesis of Electrically Conducting Organic Polymers - Halogen Derivatives of Polyacetylene, (Ch)X. *J Chem Soc Chem Comm*, 578-580 (1977).

4. Burroughes JH, *et al.* Light-emitting diodes based on conjugated polymers. *Nature* **347**, 539-541 (1990).

5. Halls JJM, *et al.* Efficient Photodiodes from Interpenetrating Polymer Networks. *Nature* **376**, 498-500 (1995).

6. Yu G, Gao J, Hummelen JC, Wudl F, Heeger AJ. Polymer Photovoltaic Cells - Enhanced Efficiencies Via a Network of Internal Donor-Acceptor Heterojunctions. *Science* **270**, 1789-1791 (1995).

7. Bao Z, Dodabalapur A, Lovinger AJ. Soluble and processable regioregular poly(3-hexylthiophene) for thin film field-effect transistor applications with high mobility. *Applied physics letters* **69**, 4108-4110 (1996).

8. Sirringhaus H, *et al.* Two-dimensional charge transport in self-organized, high-mobility conjugated polymers. *Nature* **401**, 685-688 (1999).

9. Cacialli F, Samori P, Silva C. Supramolecular architectures. *Materials Today* **7**, 24-32 (2004).

10. Sears VF. Neutron scattering lengths and cross sections. *Neutron News*, (1992).

11. Yin W, Dadmun M. A new model for the morphology of P3HT/PCBM organic photovoltaics from small-angle neutron scattering: rivers and streams. *ACS nano* **5**, 4756-4768 (2011).

12. Paternó G, Cacialli F, García-Sakai V. Structural and dynamical characterization of P3HT/PCBM blends. *Chemical Physics* **427**, 142-146 (2013).

13. O'Gorman TJ, *et al.* Field testing for cosmic ray soft errors in semiconductor memories. *Ibm Journal of Research and Development* **40**, 41-50 (1996).

14. Ziegler JF, Lanford WA. The Effect of Sea-Level Cosmic-Rays on Electronic Devices. *J Appl Phys* **52**, 4305-4312 (1981).

15. Barford W. *Electronic and optical properties of conjugated polymers*. Oxford University Press (2005).

16. Pauling L. The Nature of the Chemical Bond. Application of Results Obtained from the Quantum Mechanics and from a Theory of Paramagnetic Susceptibility to the Structure of Molecules. *Journal of the American Chemical Society* **53**, 1367-1400 (1931).

17. Peierls RE. *Quantum theory of solids*. Oxford University Press (1955).

18. Rice MJ, Strassle.S. Theory of a Quasi-One-Dimensional Band-Conductor. *Solid State Communications* **13**, 125-128 (1973).

19. Rice MJ, Strässler S. Effects of fluctuations and interchain coupling on the peierls transition. *Solid State Communications* **13**, 1389-1392 (1973).

20. Li G, Zhu R, Yang Y. Polymer solar cells. *Nature Photonics* **6**, 153-161 (2012).

21. Rice MJ. Charged Π-phase kinks in lightly doped polyacetylene. *Physics Letters A* **71**, 152-154 (1979).

22. Su WP, Schrieffer JR, Heeger AJ. Solitons in Polyacetylene. *Phys Rev Lett* **42**, 1698-1701 (1979).

23. Bredas JL, Street GB. Polarons, bipolarons, and solitons in conducting polymers. *Accounts of Chemical Research* **18**, 309-315 (1985).

24. Brédas J-L, Cornil J, Heeger AJ. The exciton binding energy in luminescent conjugated polymers. *Advanced Materials* **8**, 447-452 (1996).

25. Horowitz G. Organic field-effect transistors. *Advanced Materials* **10**, 365-377 (1998).

26. Lange J, Bässler H. Temperature dependence of the hopping mobility in amorphous tetracene. *physica status solidi (b)* **114**, 561-569 (1982).

27. Venkateshvaran D, *et al.* Approaching disorder-free transport in high-mobility conjugated polymers. *Nature* **515**, 384-388 (2014).

28. Tseng HR, *et al.* High-mobility field-effect transistors fabricated with macroscopic aligned semiconducting polymers. *Adv Mater* **26**, 2993-2998 (2014).

29. Podzorov V, Menard E, Borissov A, Kiryukhin V, Rogers JA, Gershenson ME. Intrinsic charge transport on the surface of organic semiconductors. *Phys Rev Lett* **93**, 086602 (2004).

30. Cacialli F. Organic semiconductors for the new millennium. *Philos T Roy Soc A* **358**, 173-192 (2000).

31. Cacialli F. Plastic and Molecular Electronics. *University Lecture - University College London*, (2011).

32. Ghosh AK, Morel DL, Feng T, Shaw RF, Rowe CA. Photovoltaic and rectification properties of Al⁄Mg phthalocyanine⁄Ag Schottky-barrier cells. *J Appl Phys* **45**, 230 (1974).

33. Tang C, Albrecht A. Photovoltaic effects of metal–chlorophyll a–metal sandwich cells. *The Journal of chemical physics* **62**, 2139 (1975).

34. Tang CW. Two-layer organic photovoltaic cell. *Applied physics letters* **48**, 183-185 (1986).

35. Kraabel B, Lee CH, Mcbranch D, Moses D, Sariciftci NS, Heeger AJ. Ultrafast Photoinduced Electron-Transfer in Conducting Polymer Buckminsterfullerene Composites. *Chem Phys Lett* **213**, 389-394 (1993).

36. Brabec CJ, *et al.* Tracing photoinduced electron transfer process in conjugated polymer/fullerene bulk heterojunctions in real time. *Chem Phys Lett* **340**, 232-236 (2001).

37. Garnier F, Hajlaoui R, Yassar A, Srivastava P. All-polymer field-effect transistor realized by printing techniques. *Science* **265**, 1684-1686 (1994).

38. Lilienfeld JE. Method and apparatus for controlling electric currents. US Patent 1745175 A (1930).

39. Garnier F, Horowitz G, Peng XZ, Fichou D. Structural Basis for High Carrier Mobility in Conjugated Oligomers. *Synthetic metals* **45**, 163-171 (1991).

40. Koezuka H, Tsumura A, Ando T. Field-Effect Transistor with Polythiophene Thin-Film. *Synthetic metals* **18**, 699-704 (1987).

41. McCulloch I, *et al.* Liquid-crystalline semiconducting polymers with high charge-carrier mobility. *Nature materials* **5**, 328-333 (2006).

42. Zhang X, *et al.* Molecular origin of high field-effect mobility in an indacenodithiophene-benzothiadiazole copolymer. *Nat Commun* **4**, 2238 (2013).

43. Sirringhaus H. 25th anniversary article: organic field-effect transistors: the path beyond amorphous silicon. *Adv Mater* **26**, 1319-1335 (2014).

44. Squires GL. *Introduction to the theory of thermal neutron scattering*. Cambridge university press (2012).

45. Sivia DS. *Elementary scattering theory: For X-ray and neutron users*. Oxford University Press (2011).

46. Roe R-J. Methods of X-ray and neutron scattering in polymer science. (1999).

47. Oxford School on Neutron Scattering. *Lecture Notes*, (2013).

48. ISIS, Neutron Scattering Training Course. *Lecture Notes*, (2012).

49. Van Hove L. Correlations in Space and Time and Born Approximation Scattering in Systems of Interacting Particles. *Physical Review* **95**, 249-262 (1954).

50. Stewart JR, *et al.* Disordered materials studied using neutron polarization analysis on the multi-detector spectrometer, D7. *Journal of Applied Crystallography* **42**, 69-84 (2008).

51. Moon RM, Riste T, Koehler WC. Polarization Analysis of Thermal-Neutron Scattering. *Physical Review* **181**, 920-931 (1969).

52. Ceretti M, Cousin F, Menelle A, Paulus W, Mathon MH, Ritter C. Neutron reflectivity. *EPJ Web of Conferences* **104**, 01005 (2015).

53. Kiessig H. Interferenz von Röntgenstrahlen an dünnen Schichten. *Annalen der Physik* **402**, 769-788 (1931).

54. Born MW, E. Principles of Optics: Electromagnetic Theory of Propagation, Interference and Diffraction of Light. (ed^(eds). 7th edn. Pergamon Press (1999).

55. Sakai VG, Arbe A. Quasielastic neutron scattering in soft matter. *Curr Opin Colloid In* **14**, 381-390 (2009).

56. Williams G, Watts DC. Non-Symmetrical Dielectric Relaxation Behaviour Arising from a Simple Empirical Decay Function. *Transactions of the Faraday Society* **66**, 80-& (1970).

57. Braley GS, Townsend LW, Cucinotta FA, Heilbronn LH. Modeling of secondary neutron production from space radiation interactions. *IEEE Transactions on Nuclear Science* **49**, 2800-2804 (2002).

58. Simonsen LC, Nealy JE. Radiation protection for human missions to the Moon and Mars. *Nasa Technical Paper* **3079**, (1991).

59. Lesea A, Drimer S, Fabula JJ, Carmichael C, Alfke P. The Rosetta experiment: Atmospheric soft error rate testing in differing technology FPGAs. *Ieee T Device Mat Re* **5**, 317-328 (2005).

60. Mayers J, *et al.* VESUVIO-the double difference inverse geometry spectrometer at ISIS. *Physica B-condensed Matter* **350**, E659-E662 (2004).

61. Andreani C, *et al.* Facility for fast neutron irradiation tests of electronics at the ISIS spallation neutron source. *Applied physics letters* **92**, 114101-111404 (2008).

62. Platt S, Torok Z, Frost CD, Ansell S. Charge-Collection and Single-Event Upset Measurements at the ISIS Neutron Source. *IEEE Transactions on Nuclear Science* **55**, 2126-2132 (2008).

63. Bedogni R, *et al.* Characterization of the neutron field at the ISIS-VESUVIO facility by means of a bonner sphere spectrometer. *Nuclear Instruments and Methods in Physics Research Section A: Accelerators, Spectrometers, Detectors and Associated Equipment* **612**, 143-148 (2009).

64. Paternò G, *et al.* Micro-focused X-ray diffraction characterization of high-quality [6,6]-phenyl-C61-butyric acid methyl ester single crystals without solvent impurities. *Journal of Materials Chemistry C* **1**, 5619-5623 (2013).

65. Lazzerini GM, *et al.* Traceable atomic force microscopy of high-quality solvent-free crystals of [6,6]-phenyl-C61-butyric acid methyl ester. *Applied physics letters* **108**, 053303 (2016).

66. Fraboni B, *et al.* Solution-Grown, Macroscopic Organic Single Crystals Exhibiting Three-Dimensional Anisotropic Charge-Transport Properties. *Advanced Materials* **21**, 1835-1839 (2009).

67. Fraleoni-Morgera A, Benevoli L, Fraboni B. Solution growth of single crystals of 4-hydroxycyanobenzene (4HCB) suitable for electronic applications. *Journal of Crystal Growth* **312**, 3466-3472 (2010).

68. Podzorov V. Organic single crystals: Addressing the fundamentals of organic electronics. *Mrs Bull* **38**, 15-27 (2013).

69. Briseno AL, *et al.* Patterning organic single-crystal transistor arrays. *Nature* **444**, 913-917 (2006).

70. Virkar AA, Mannsfeld S, Bao Z, Stingelin N. Organic semiconductor growth and morphology considerations for organic thin-film transistors. *Adv Mater* **22**, 3857-3875 (2010).

71. Ayzner AL, Tassone CJ, Tolbert SH, Schwartz BJ. Reappraising the Need for Bulk Heterojunctions in Polymer−Fullerene Photovoltaics: The Role of Carrier Transport in All-Solution-Processed P3HT/PCBM Bilayer Solar Cells. *The Journal of Physical Chemistry C* **113**, 20050-20060 (2009).

72. Yu G, Heeger AJ. Charge Separation and Photovoltaic Conversion in Polymer Composites with Internal Donor-Acceptor Heterojunctions. *J Appl Phys* **78**, 4510-4515 (1995).

73. Yang XN, *et al.* Crystalline organization of a methanofullerene as used for plastic solar-cell applications. *Advanced Materials* **16**, 802-806 (2004).

74. Hoppe H, Drees A, Schwinger W, Schaffler F, Sariciftci NS. Nano-crystalline fullerene phases in polymer/fullerene bulk-heterojunction solar cells: A transmission electron Microscopy study. *Synthetic metals* **152**, 117-120 (2005).

75. Yang XN, van Duren JKJ, Janssen RAJ, Michels MAJ, Loos J. Morphology and thermal stability of the active layer in poly(p-phenylenevinylene)/methanofullerene plastic photovoltaic devices. *Macromolecules* **37**, 2151-2158 (2004).

76. Hoppe H, Glatzel T, Niggemann M, Hinsch A, Lux-Steiner M, Sariciftci NS. Kelvin probe force microscopy study on conjugated polymer/fullerene bulk heterojunction organic solar cells. *Nano letters* **5**, 269-274 (2005).

77. Piersimoni F, *et al.* Influence of Fullerene Ordering on the Energy of the Charge-Transfer State and Open-Circuit Voltage in Polymer:Fullerene Solar Cells. *Journal of Physical Chemistry C* **115**, 10873-10880 (2011).

78. Swinnen A, *et al.* Tuning the Dimensions of C60-Based Needlelike Crystals in Blended Thin Films. *Advanced Functional Materials* **16**, 760-765 (2006).

79. Reyes-Reyes M, Lopez-Sandoval R, Arenas-Alatorre J, Garibay-Alonso R, Carroll DL, Lastras-Martinez A. Methanofullerene elongated nanostructure formation for enhanced organic solar cells. *Thin Solid Films* **516**, 52-57 (2007).

80. Li L, Lu G, Li S, Tang H, Yang X. Epitaxy-assisted creation of PCBM nanocrystals and its application in constructing optimized morphology for bulk-heterojunction polymer solar cells. *J Phys Chem B* **112**, 15651-15658 (2008).

81. Dante M, Peet J, Nguyen TQ. Nanoscale charge transport and internal structure of bulk heterojunction conjugated polymer/fullerene solar cells by scanning probe microscopy. *Journal of Physical Chemistry C* **112**, 7241-7249 (2008).

82. Casalegno M, *et al.* Solvent-free phenyl-C61-butyric acid methyl ester (PCBM) from clathrates: insights for organic photovoltaics from crystal structures and molecular dynamics. *Chem Commun (Camb)* **49**, 4525-4527 (2013).

83. Rispens MT, Meetsma A, Rittberger R, Brabec CJ, Sariciftci NS, Hummelen JC. Influence of the solvent on the crystal structure of PCBM and the efficiency of MDMO-PPV : PCBM 'plastic' solar cells. *Chem Commun*, 2116-2118 (2003).

84. Dabirian R, *et al.* Micron-sized [6,6]-phenyl C61 butyric acid methyl ester crystals grown by dip coating in solvent vapour atmosphere: interfaces for organic photovoltaics. *Phys Chem Chem Phys* **12**, 4473-4480 (2010).

85. Zheng L, Han Y. Solvated crystals based on [6,6]-phenyl-C61-butyric acid methyl ester (PCBM) with the hexagonal structure and their phase transformation. *J Phys Chem B* **116**, 1598-1604 (2012).

86. Gajdos F, Oberhofer H, Dupuis M, Blumberger J. On the Inapplicability of Electron-Hopping Models for the Organic Semiconductor Phenyl-C61-butyric Acid Methyl Ester (PCBM). *J Phys Chem Lett* **4**, 1012-1017 (2013).

87. Cheung DL, Troisi A. Theoretical Study of the Organic Photovoltaic Electron Acceptor PCBM: Morphology, Electronic Structure, and Charge Localization†. *The Journal of Physical Chemistry C* **114**, 20479-20488 (2010).

88. Oberhofer H, Blumberger J. Revisiting electronic couplings and incoherent hopping models for electron transport in crystalline C60 at ambient temperatures. *Phys Chem Chem Phys* **14**, 13846-13852 (2012).

89. Mackenzie RC, Frost JM, Nelson J. A numerical study of mobility in thin films of fullerene derivatives. *The Journal of chemical physics* **132**, 064904 (2010).

90. Agilent (2012). CrysAlis Pro. Agilent Technologies, Oxfordshire, England. (ed^(eds).

91. Sheldrick GM. A short history of SHELX. *Acta crystallographica Section A, Foundations of crystallography* **64**, 112-122 (2008).

92. Jorgensen WL, Maxwell DS, TiradoRives J. Development and testing of the OPLS all-atom force field on conformational energetics and properties of organic liquids. *Journal of the American Chemical Society* **118**, 11225-11236 (1996).

93. Hedberg K, *et al.* Bond lengths in free molecules of buckminsterfullerene, c60, from gas-phase electron diffraction. *Science* **254**, 410-412 (1991).

94. Heiney PA. Structure, dynamics and ordering transition of solid C60. *Journal of Physics and Chemistry of Solids* **53**, 1333-1352 (1992).

95. Phillips JC, *et al.* Scalable molecular dynamics with NAMD. *J Comput Chem* **26**, 1781-1802 (2005).

96. Frigerio F, Casalegno M, Carbonera C, Nicolini T, Meille SV, Raos G. Molecular dynamics simulations of the solvent- and thermal history-dependent structure of the PCBM fullerene derivative. *Journal of Materials Chemistry* **22**, 5434 (2012).

97. Podzorov V. Organic single crystals: Addressing the fundamentals of organic electronics. *Mrs Bull* **38**, 15-24 (2013).

98. Danzebrink HU, Koenders L, Wilkening G, Yacoot A, Kunzmann H. Advances in scanning force microscopy for dimensional metrology. *Cirp Annals-manufacturing Technology* **55**, 841-878 (2006).

99. Marco P, *et al.* Comparison of the performance of the next generation of optical interferometers. *Metrologia* **49**, 455 (2012).

100. Stone JA, *et al.* Advice from the CCL on the use of unstabilized lasers as standards of wavelength: the helium–neon laser at 633 nm. *Metrologia* **46**, 11 (2009).

101. Paterno GM, Skoda MW, Dalgliesh R, Cacialli F, Sakai VG. Tuning Fullerene Intercalation in a Poly (thiophene) derivative by Controlling the Polymer Degree of Self-Organisation. *Sci Rep* **6**, 34609 (2016).

102. Riehn R, *et al.* Local probing of photocurrent and photoluminescence in a phase-separated conjugated-polymer blend by means of near-field excitation. *Advanced Functional Materials* **16**, 469-476 (2006).

103. Stevenson R, *et al.* Ultraviolet–visible near-field microscopy of phase-separated blends of polyfluorene-based conjugated semiconductors. *Applied physics letters* **79**, 833-835 (2001).

104. Collins BA, Tumbleston JR, Ade H. Miscibility, Crystallinity, and Phase Development in P3HT/PCBM Solar Cells: Toward an Enlightened Understanding of Device Morphology and Stability. *J Phys Chem Lett* **2**, 3135-3145 (2011).

105. Miller NC, *et al.* Factors Governing Intercalation of Fullerenes and Other Small Molecules Between the Side Chains of Semiconducting Polymers Used in Solar Cells. *Advanced Energy Materials* **2**, 1208-1217 (2012).

106. Cates NC, *et al.* Tuning the properties of polymer bulk heterojunction solar cells by adjusting fullerene size to control intercalation. *Nano letters* **9**, 4153-4157 (2009).

107. Mayer AC, *et al.* Bimolecular Crystals of Fullerenes in Conjugated Polymers and the Implications of Molecular Mixing for Solar Cells. *Advanced Functional Materials* **19**, 1173-1179 (2009).

108. Nyman M, Sandberg OJ, Österbacka R. Charge transport in intercalated and non-intercalated polymer:fullerene blends. *Synthetic metals* **201**, 6-10 (2015).

109. Gao J, Thomas AK, Johnson R, Guo H, Grey JK. Spatially Resolving Ordered and Disordered Conformers and Photocurrent Generation in Intercalated Conjugated Polymer/Fullerene Blend Solar Cells. *Chem Mater* **26**, 4395-4404 (2014).

110. Lee C-K, Pao C-W. Solubility of [6,6]-Phenyl-C61-butyric Acid Methyl Ester and Optimal Blending Ratio of Bulk Heterojunction Polymer Solar Cells. *The Journal of Physical Chemistry C* **116**, 12455-12461 (2012).

111. Sun QJ, Park K, Dai LM. Liquid Crystalline Polymers for Efficient Bilayer-Bulk-Heterojunction Solar Cells. *Journal of Physical Chemistry C* **113**, 7892-7897 (2009).

112. Guangye Z, *et al.* Crystallinity Effects in Sequentially Processed and Blend-Cast Bulk-Heterojunction Polymer/Fullerene Photovoltaics. *The Journal of Physical Chemistry C* **118**, (2014).

113. Chen D, Liu F, Wang C, Nakahara A, Russell TP. Bulk heterojunction photovoltaic active layers via bilayer interdiffusion. *Nano letters* **11**, 2071-2078 (2011).

114. Kim JS, *et al.* Indium–tin oxide treatments for single- and double-layer polymeric light-emitting diodes: The relation between the anode physical, chemical, and morphological properties and the device performance. *J Appl Phys* **84**, 6859-6870 (1998).

115. Brown TM, Lazzerini GM, Parrott LJ, Bodrozic V, Burgi L, Cacialli F. Time dependence and freezing-in of the electrode oxygen plasma-induced work function enhancement in polymer semiconductor heterostructures. *Organic Electronics* **12**, 623-633 (2011).

116. Kim JS, Friend RH, Cacialli F. Surface energy and polarity of treated indium-tin-oxide anodes for polymer light-emitting diodes studied by contact-angle measurements. *J Appl Phys* **86**, 2774-2778 (1999).

117. Brown TM, Kim JS, Friend RH, Cacialli F, Daik R, Feast WJ. Built-in field electroabsorption spectroscopy of polymer light-emitting diodes incorporating a doped poly(3,4-ethylene dioxythiophene) hole injection layer. *Applied physics letters* **75**, 1679-1681 (1999).

118. Dalgliesh RM, Langridge S, Plomp J, de Haan VO, van Well AA. Offspec, the ISIS spin-echo reflectometer. *Physica B-condensed Matter* **406**, 2346-2349 (2011).

119. Nevot, Croce. Caractérisation des surfaces par réflexion rasante de rayons X. Application à l'étude du polissage de quelques verres silicates. *Revue de Physique appliquée* **15**, 761-779 (1980).

120. Li G, *et al.* High-efficiency solution processable polymer photovoltaic cells by self-organization of polymer blends. *Nature materials* **4**, 864-868 (2005).

121. Parnell AJ, *et al.* Depletion of PCBM at the cathode interface in P3HT/PCBM thin films as quantified via neutron reflectivity measurements. *Adv Mater* **22**, 2444-2447 (2010).

122. Germack DS, *et al.* Substrate-dependent interface composition and charge transport in films for organic photovoltaics. *Applied physics letters* **94**, 233303 (2009).

123. Parmer JE, *et al.* Organic bulk heterojunction solar cells using poly(2,5-bis(3-tetradecyllthiophen-2-yl)thieno[3,2,-b]thiophene). *Applied physics letters* **92**, 113309-113312 (2008).

124. Hwang IW, *et al.* Bulk heterojunction materials composed of poly(2,5-bis(3-tetradecylthiophen-2-yl)thieno[3,2-b]thiophene): Ultrafast electron transfer and carrier recombination. *Journal of Physical Chemistry C* **112**, 7853-7857 (2008).

125.釈Paternò GM, Stewart JR, Wildes A, Cacialli F, Sakai VG. Neutron polarisation analysis of Polymer:Fullerene blends for organic photovoltaics. *Polymer* **105**, 407-413 (2016).

126. Obrzut J, Page KA. Electrical conductivity and relaxation in poly(3-hexylthiophene). *Phys Rev B* **80**, (2009).

127. Guilbert AAY, *et al.* Temperature-Dependent Dynamics of Polyalkylthiophene Conjugated Polymers: A Combined Neutron Scattering and Simulation Study. *Chemistry of Materials*, (2015).

128. Etampawala T, Ratnaweera D, Morgan B, Diallo S, Mamontov E, Dadmun M. Monitoring the dynamics of miscible P3HT:PCBM blends: A quasi elastic neutron scattering study of organic photovoltaic active layers. *Polymer* **61**, 155-162 (2015).

129. Collins BA, Gann E, Guignard L, He X, McNeill CR, Ade H. Molecular Miscibility of Polymer−Fullerene Blends. *The Journal of Physical Chemistry Letters* **1**, 3160-3166 (2010).

130. Carlile CJ, Adams MA. The Design of the Iris Inelastic Neutron Spectrometer and Improvements to Its Analyzers. *Physica B* **182**, 431-440 (1992).

131. Arrighi V, Tanchawanich J, Telling MTF. Molar Mass Dependence of Polyethylene Chain Dynamics. A Quasi-Elastic Neutron Scattering Investigation. *Macromolecules* **46**, 216-225 (2013).

132. Malik S, Nandi AK. Crystallization mechanism of regioregular poly(3-alkyl thiophene)s. *Journal of Polymer Science Part B-polymer Physics* **40**, 2073-2085 (2002).

133. Kim JY, Frisbie CD. Correlation of Phase Behavior and Charge Transport in Conjugated Polymer/Fullerene Blends. *Journal of Physical Chemistry C* **112**, 17726-17736 (2008).

134. Kim Y, Choulis SA, Nelson J, Bradley DDC, Cook S, Durrant JR. Device annealing effect in organic solar cells with blends of regioregular poly(3-hexylthiophene) and soluble fullerene. *Applied physics letters* **86**, 063502 (2005).

135. Zhao J, Swinnen A, Van Assche G, Manca J, Vanderzande D, Van Mele B. Phase diagram of P3HT/PCBM blends and its implication for the stability of morphology. *J Phys Chem B* **113**, 1587-1591 (2009).

136. Dang MT, Hirsch L, Wantz G, Wuest JD. Controlling the morphology and performance of bulk heterojunctions in solar cells. Lessons learned from the benchmark poly(3-hexylthiophene):[6,6]-phenyl-C61-butyric acid methyl ester system. *Chem Rev* **113**, 3734-3765 (2013).

137. Machui F, Langner S, Zhu XD, Abbott S, Brabec CJ. Determination of the P3HT:PCBM solubility parameters via a binary solvent gradient method: Impact of solubility on the photovoltaic performance. *Solar Energy Materials and Solar Cells* **100**, 138-146 (2012).

138. Zhao Y, Yuan G, Roche P, Leclerc M. A calorimetric study of the phase transitions in poly(3-hexylthiophene). *Polymer* **36**, 2211-2214 (1995).

139. Burankova T, Hempelmann R, Wildes A, Embs JP. Collective ion diffusion and localized single particle dynamics in pyridinium-based ionic liquids. *The journal of physical chemistry B* **118**, 14452-14460 (2014).

140. Kropka J, Garcia Sakai V, Green P. Local polymer dynamics in polymer-C60 mixtures. *Nano letters* **8**, 1061-1065 (2008).

141. Richard DF, M.; Kearley, G. J.; Bradley, A. D. *The LAMP book* **Institut Laue-Langevin** http://www.ill.eu/?id=2024 (2013).

142. Azuah RT, *et al.* DAVE: A Comprehensive Software Suite for the Reduction, Visualization, and Analysis of Low Energy Neutron Spectroscopic Data. *Journal of Research of the National Institute of Standards and Technology* **114**, 341-358 (2009).

143. Destri GL, Keller TF, Catellani M, Punzo F, Jandt KD, Marletta G. Interfacial free energy driven nanophase separation in poly(3-hexylthiophene)/[6,6]-phenyl-C61-butyric acid methyl ester thin films. *Langmuir* **28**, 5257-5266 (2012).

144. Chen CY, *et al.* Mechanism and control of the structural evolution of a polymer solar cell from a bulk heterojunction to a thermally unstable hierarchical structure. *Nanoscale* **5**, 7629-7638 (2013).

145. Armstrong J, Mukhopadhyay S, Bresme F, Fernandez-Alonso F. Heads or tails: how do chemically substituted fullerenes melt? *Phys Chem Chem Phys* **18**, 17202-17209 (2016).

146. G. M. Paternò VR, K. J. Fraser, C. Frost, V. García Sakai and F. Cacialli. Neutron Radiation Tolerance of Two Benchmark Thiophene- Based Conjugated Polymers: the Importance of Crystallinity for Organic Avionics. *Sci Rep-Uk* **In press**, (2017).

147. Kaltenbrunner M, *et al.* Ultrathin and lightweight organic solar cells with high flexibility. *Nat Commun* **3**, 770 (2012).

148. Yi HT, Payne MM, Anthony JE, Podzorov V. Ultra-flexible solution-processed organic field-effect transistors. *Nat Commun* **3**, 1259 (2012).

149. Grossman E, Gouzman I. Space environment effects on polymers in low earth orbit. *Nucl Instrum Meth B* **208**, 48-57 (2003).

150. Armstrong TW, Colborn BL. Predictions of secondary neutrons and their importance to radiation effects inside the international space station. *Radiation measurements* **33**, 229-234 (2001).

151. Kumar A, Devine R, Mayberry C, Lei B, Li G, Yang Y. Origin of Radiation-Induced Degradation in Polymer Solar Cells. *Advanced Functional Materials* **20**, 2729-2736 (2010).

152. Street RA, Northrup JE, Krusor BS. Radiation induced recombination centers in organic solar cells. *Phys Rev B* **85**, 205211-205224 (2012).

153. Raval HN, Sutar DS, Nair PR, Ramgopal Rao V. Investigation of effects of ionizing radiation exposure on material properties of organic semiconducting oligomer – Pentacene. *Organic Electronics* **14**, 1467-1476 (2013).

154. Yajima K, *et al.* Measurements of Cosmic-Ray Neutron Energy Spectra from Thermal to 15 MeV with Bonner Ball Neutron Detector in Aircraft. *Journal of Nuclear Science and Technology* **47**, 31-39 (2010).

155. Koshiishi H, Matsumoto H, Chishiki A, Goka T, Omodaka T. Evaluation of the neutron radiation environment inside the International Space Station based on the Bonner Ball Neutron Detector experiment. *Radiation measurements* **42**, 1510-1520 (2007).

156. Sirringhaus H, Tessler N, Friend RH. Integrated optoelectronic devices based on conjugated polymers. *Science* **280**, 1741-1744 (1998).

157. Jenkins JL, Lee PA, Nebesny KW, Ratcliff EL. Systematic electrochemical oxidative doping of P3HT to probe interfacial charge transfer across polymer–fullerene interfaces. *J Mater Chem A* **2**, 19221-19231 (2014).

158. Ratcliff EL, Jenkins JL, Nebesny K, Armstrong NR. Electrodeposited, “Textured” Poly(3-hexyl-thiophene) (e-P3HT) Films for Photovoltaic Applications. *Chemistry of Materials* **20**, 5796-5806 (2008).

159. Naudin E, Dabo P, Guay D, Belanger D. X-ray photoelectron spectroscopy studies of the electrochemically n-doped state of a conducting polymer. *Synthetic metals* **132**, 71-79 (2002).

160. Clark J, Silva C, Friend RH, Spano FC. Role of intermolecular coupling in the photophysics of disordered organic semiconductors: aggregate emission in regioregular polythiophene. *Phys Rev Lett* **98**, 206406 - 206409 (2007).

161. Chung TC, Kaufman JH, Heeger AJ, Wudl F. Charge Storage in Doped Poly(Thiophene) - Optical and Electrochemical Studies. *Phys Rev B* **30**, 702-710 (1984).

162. Castiglioni C, Delzoppo M, Zerbi G. Vibrational Raman-Spectroscopy of Polyconjugated Organic Oligomers and Polymers. *Journal of Raman Spectroscopy* **24**, 485-494 (1993).

163. Zerbi G. Vibrational Spectroscopy of Conducting Polymers: Theory and Perspective. In: *Handbook of Vibrational Spectroscopy*. John Wiley & Sons, Ltd (2006).

164. Gao Y, Grey JK. Resonance chemical imaging of polythiophene/fullerene photovoltaic thin films: mapping morphology-dependent aggregated and unaggregated C=C Species. *J Am Chem Soc* **131**, 9654-9662 (2009).

165. Tsoi WC, *et al.* The nature of in-plane skeleton Raman modes of P3HT and their correlation to the degree of molecular order in P3HT:PCBM blend thin films. *J Am Chem Soc* **133**, 9834-9843 (2011).

166. Yun JJ, Peet J, Cho NS, Bazan GC, Lee SJ, Moskovits M. Insight into the Raman shifts and optical absorption changes upon annealing polymer/fullerene solar cells. *Applied physics letters* **92**, 251912-225915 (2008).

167. Bazzaoui EA, Levi G, Aeiyach S, Aubard J, Marsault JP, Lacaze PC. Sers Spectra of Polythiophene in Doped and Undoped States. *J Phys Chem-Us* **99**, 6628-6634 (1995).

168. Bellani S, *et al.* Reversible P3HT/Oxygen Charge Transfer Complex Identification in Thin Films Exposed to Direct Contact with Water. *The Journal of Physical Chemistry C* **118**, 6291-6299 (2014).

169. Baibarac M, Lapkowski M, Pron A, Lefrant S, Baltog I. SERS spectra of poly(3-hexylthiophene) in oxidized and unoxidized states. *Journal of Raman Spectroscopy* **29**, 825-832 (1998).

170. Sauvajol JL, Chenouni D, Lereporte JP, Chorro C, Moukala B, Petrissans J. Resonant Raman-Spectra and Photoluminescence in Polythiophene. *Synthetic metals* **38**, 1-12 (1990).

171. Ha TJ, Sparrowe D, Dodabalapur A. Device architectures for improved amorphous polymer semiconductor thin-film transistors. *Organic Electronics* **12**, 1846-1851 (2011).

172. Pingel P, Schwarzl R, Neher D. Effect of molecular p-doping on hole density and mobility in poly(3-hexylthiophene). *Applied physics letters* **100**, 143303-143306 (2012).

173. Street RA, Krakaris A, Cowan SR. Recombination Through Different Types of Localized States in Organic Solar Cells. *Advanced Functional Materials* **22**, 4608-4619 (2012).

174. Quantitative estimation of the rate of such events and calculation of deposited energy in the sample would require further computational analysis, which is beyond the scope of this manuscript.

175. Rabek JF. *Photodegradation of polymers: physical characteristics and applications*. Springer Science & Business Media (2012).

176. Arthur JC, Hinojosa O, Tripp VW. Effect of crystalline structure on the trapped radical spectra of irradiated cellulose. *Journal of Applied Polymer Science* **13**, 1497-1507 (1969).

177. Williams D, Schmidt B, Wolfrom ML, Michelakis A, McCabe LJ. Paramagnetic Resonance Spectra of Free Radicals Trapped on Irradiation of Crystalline Carbohydrates. *Proc Natl Acad Sci U S A* **45**, 1744-1751 (1959).

178. Zhao L-H, *et al.* Role of Borderline Solvents to Induce Pronounced Extended-Chain Lamellar Order in π-Stackable Polymers. *Macromolecules* **44**, 9692-9702 (2011).

179. Tregnago G, Wykes M, Paternò GM, Beljonne D, Cacialli F. Low-Temperature Photoluminescence Spectroscopy of Solvent-Free PCBM Single-Crystals. *The Journal of Physical Chemistry C* **119**, 11846-11851 (2015).

180. Zeynalov EB, Allen NS, Salmanova NI. Radical scavenging efficiency of different fullerenes C60–C70 and fullerene soot. *Polymer Degradation and Stability* **94**, 1183-1189 (2009).